Study of high-quality InGaN growth by metalorganic vapor phase epitaxy

(有機金属気相成長法による高品質のInGaN成長に関する研究)

.

LIU ZHIBIN
劉　志彬

Doctoral Dissertation

Study of high-quality InGaN growth by metalorganic vapor phase epitaxy

A DISSERTATION SUBMITTED TO DEPARTMENT OF ELECTRICAL
ENGINEERING AND COMPUTER SCIENCE
SCHOOL OF ENGINEERING
NAGOYA UNIVERSITY
FOR THE DEGREE OF
DOCTOR OF ENGINEERING

ZHIBIN LIU

2, 2019

Abstract

InGaN alloy with advantages, such as direct band gap, good thermal stability, and the whole visible spectra coverage, is usually used as the active layer of optoelectronic devices. Metalorganic vapor phase epitaxy (MOVPE) as a main growth method is widely applied in factories from viewpoints of growth rate and crystal quality. For violet-blue emission, high internal quantum efficiency (IQE) has already been achieved. However, for green, yellow, and even longer wavelength emission, an improvement of IQEs is needed in practical use. Besides polarization and the quantum-confined Stark effect, low growth temperature and high growth rate which are favorable for high InN mole fraction cause many types of defects which attribute to non-radiative recombination for a reduction in IQE. In this thesis, the single InGaN layer growth and its effect on multi-quantum well (MQW) growth are systematically studied and then the effect of gas phase temperature is investigated.

First, the morphology of single InGaN layer grown on GaN substrate by MOVPE with different growth condition is studied in detail. Three different morphologies appeared, a stepped surface, large flat two-dimensional (2D) islands, small high three-dimensional (3D) dots. Then the morphology transition is analyzed by supersaturation. The effect of miscut angle of GaN substrate on InGaN growth is systematically investigated. The critical miscut angle from 2D islands to steps is related to growth condition. At last, InGaN layers grown on GaN substrate and GaN/sapphire template are compared to illustrate the advantage of GaN substrate for InGaN layer growth.

Furthermore, InGaN/GaN multiple quantum wells (MQWs) growth is investigated. First, MQWs with low InN-mole-fraction and high InN-mole-fraction are compared to study the effect of InGaN layer on MQW growth and then, the difficulty of high InN-mole-fraction MQW growth are shown. Moreover, MQWs on GaN substrate and GaN/sapphire template are analyzed to show the effect of substrate. At last, the effect of micut angle on MQW growth is investigated. It is shown that a smooth InGaN layer itself is a key point for InGaN-based MQW growth.

The effect of gas phase temperature on InGaN grown by metalorganic vapor phase epitaxy is demonstrated at last. Four wafer trays with different gaps are used to control the temperature difference between the wafer surface and the gas phase, and five-period InGaN/GaN MQWs for different wavelength are grown on 2-inch GaN/sapphire templates with each wafer tray. The simulation result of thermal distribution in the reactor shows that the gas phase temperature increases with increasing gap to maintain a constant surface temperature, which is expected to increase the decomposition rate of NH_3. The effect of this increased gas phase temperature on MQW growth with different wavelengths is studied by photoluminescence (PL) and atomic force microscope (AFM).

Table of Contents

Chapter 1 Introduction

1.1 Introduction to III-nitrides and InGaN

1.1.1. III-nitride semiconductors

Nitrides have been widely applied for optoelectronic devices such as light-emitting diode (LED) and laser diode (LD) from 1990s. Recently, the application of nitrides for power devices have also been hot topics. Nitrides have some excellent advantage such as large band gap, high hardness, corrosion resistance, environmental friendly nature. Nitrides have the wurtzite crystallographic structure which is the most thermodynamically stable structure as shown in Fig. 1.1. The wurtzite crystallographic structure is considered as the combination of two hexagonal close-packed structures involving the anions (the nitrogen atoms) and cations (the metal atoms). Locally, each atom is surrounded by four atoms of another element which can compose a tetrahedron. III-Nitrides have much large band gap range from 0.7 eV (InN) to 6.2 eV (AlN) as shown in Fig. 1.2, which cover the spectrum from ultra violet (UV) to infrared (IR). Such a wide spectrum with a direct bandgap makes it promising for full color system. GaN-based blue LED also can be used for solid-state lighting, which has some advantages, such as small size, long lifetime, and so forth. The U.S. Department of Energy predicted that it will result in a 7% reduction in total electricity use of general lighting [3].

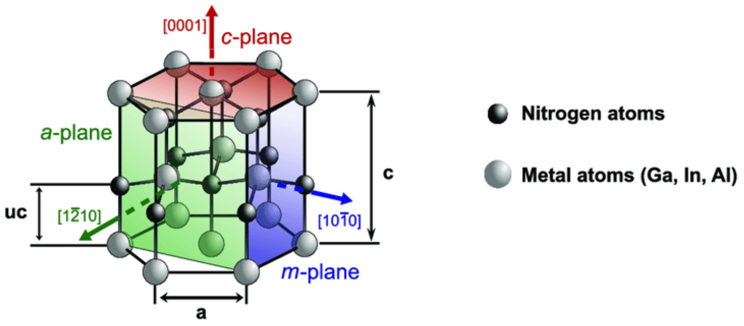

Fig. 1.1 Wurtzite crystal structure of III-nitrides [1].

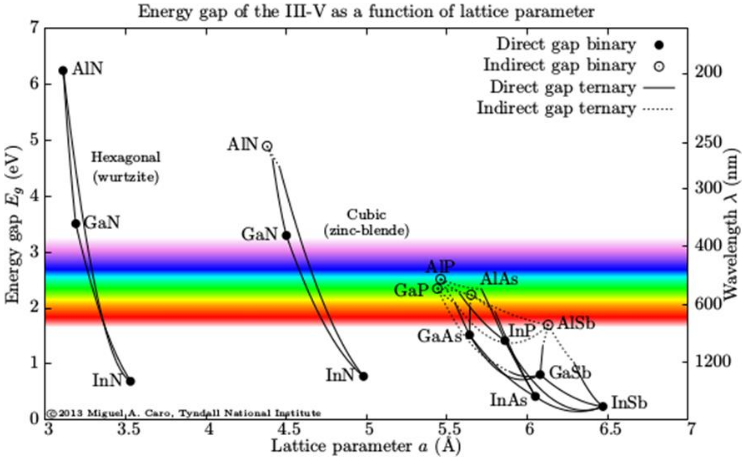

Fig. 1.2 Energy band gap of III-nitrides as a function of lattice parameter [2].

Besides, wide energy bandgap also enables nitrides to be applied for electronic devices which can operate in high power conditions because of a relatively high electric breakdown field. Furthermore, excellent carrier transport properties such as high electron mobility and large electron saturation velocity make it suitable for high frequency and high power electronic devices. Moreover, a good thermal conductivity is also a crucial factor for high-frequency devices. Nitride devices can decrease the size of the device and is promising to reduce 10% electricity consumption in the future. Fig. 1.3 summarize the applications of III-nitride.

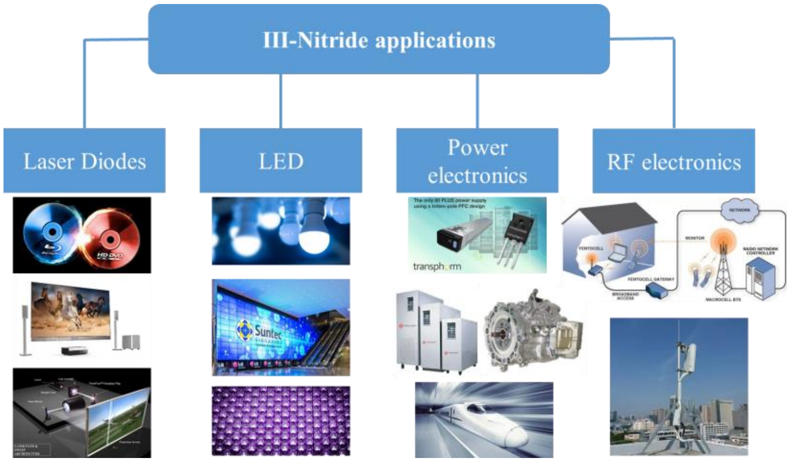

Fig. 1.3 III-nitride applications.

In 1985, H. Amano et al. first grew GaN on sapphire with successive and flat surface by metalorganic vapor phase epitaxy (MOVPE) [4]. They use the two-step growth mechanism involve low temperature AlN buffer [5] and high temperature GaN growth. After that, *p*-type conductivity in Mg-doped GaN via low-energy electron beam irradiation (LEEBI) was realized in 1989 and GaN *p*-*n* junction blue LED was achieved firstly [6]. At the same year, T. Matsuoka et al. at Nippon Telegraph and Telephone Public Corporation (NTT) achieved InGaN under an extremely high ammonia supply with nitrogen carrier gas [7]. In 1993, S. Nakamura et al Nichia Corporation succeeded in commercializing double heterostructure-type InGaN blue LEDs firstly in the world by combining low-temperature-deposited GaN buffer layer with p-type annealing technology and InGaN growth technologies [8, 9]. Since then, nitride-related technologies started to be developed at a fast speed. Nitrides will make a great contribution to human and revolute the human's life in near future.

1.1.2. InGaN alloy

Table 1.2 Band gap and lattice of InN, GaN, and AlN.

	Band gap (eV)	a (nm)	c (nm)
InN	0.77	0.355	0.570
GaN	3.43	0.319	0.519
AlN	6.28	0.311	0.498

InGaN as a nitride family member has wide application for optical devices. InGaN is the ternary compound with InN and GaN. The lattice constant along a-axis is from 0.319 (GaN) to 0.355 (InN) nm. The lattice constant depends on the InN mole fraction x,

$$a\left(In_xGa_{(1-x)}N\right) = xa(InN) + (1-x)a(GaN) \tag{1.1}$$

Similarly, the bandgap E is a function of the InN mole fraction x with the bowing parameter b as follows [10] and the experiment result is shown in Fig. 1.4,

$$E_g\left(In_xGa_{(1-x)}N\right) = xE(InN) + (1-x)E(GaN) - b(1-x)x \tag{1.2}$$

In Fig. 1.4, the band gap of InGaN is from 0.64 eV to 3.4 eV, which covers the full visible spectrum.

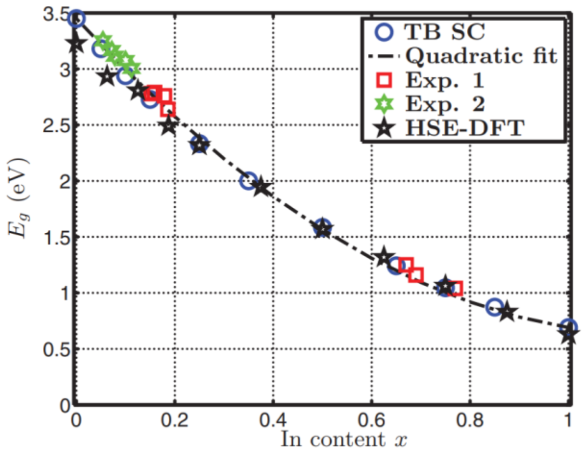

Fig. 1.4 Band gap E_g of $In_xGa_{1-x}N$ as a function of the In content x [10].

1.2 Mechanism of InGaN growth

InGaN is grown by Molecular-beam epitaxy (MBE), Hydride vapor phase epitaxy (HVPE), Metalorganic vapor phase epitaxy (MOVPE).

1.2.1 MBE

MBE, as one physical vapor deposition (PVD) technique, is a most frequently used epitaxial growth technique for growing thin epitaxial structures. In this technology, thin epitaxial layers are grown by reactions between molecular or atomic beams of the components with thermal energy on a substrate surface at a certain temperature in ultrahigh vacuum. At first, solid source material is evaporated in a Knudsen mode or heated by electron beam and laser radiation. And then molecules or atoms can be emitted to the heated substrate as a beam because of the pressure difference between the source and the reactor. During the emitting process, there is almost no interaction between the atoms of reactant elements because of ultrahigh vacuum in the growth reactor (less than 10^{-7} Pa). Therefore, the angle or velocity of the beam molecules will not be changed. On the other hand, the effusion cell is designed accurately to make the beam molecules distribution uniform in space which leads to a uniform layer. Due to vacuum deposition, MBE is carried out under conditions far from thermodynamic equilibrium and is governed mainly by the surface kinetics processes occurring when the impinging beams react with the outermost atomic layers of the substrate crystal.

R. Singh and T. D. Moustakas first reported InGaN growth by electron cyclotron resonance microwave plasma-assisted MBE (ECR-MBE) in 1996 [11]. Gallium and Indium was evaporated by a conventional Knudsen effusion cell and atomic and ionic nitrogen were formed by passing molecular nitrogen through the ECR source with ~10% conversation rate. They successfully grew 0.5-1 μm thick InGaN (InN mole fraction= 0.1-0.37) layer without any indium droplet and a thin GaN/InGaN/GaN with 81% InN mole fraction at 725 °C. After several years, radio frequency plasma-assisted molecular beam epitaxy (RF-MBE) has been significantly improved to grow InN or InGaN alloy [12, 13]. In this growth method, excited nitrogen radicals can be generated separately by an EPI unibulk RF plasma source [12].

In 2000, C. Adelmann et al. reports that InGaN QD was grown by RF-MBE [14]. RHEED curve first oscillated corresponding to layer-by-layer growth and then accidently rise rapidly which means QD formed. Because high In content and abundant N source can easily be achieved in MBE system, high-quality wetting layers can be grown and then QD form on these wetting layers by standard Stranki-Krastanov (S-K) mode. Recently, some researcher also reported the InGaN nano-structure grown by MBE [15].

For InGaN growth, compared with MOVPE, a great advantage of MBE is that atomic nitrogen has been formed before inducing into reactor. In this case, NH_3 decomposition rate can be neglected and high V/III ratio can be achieved in reactor theoretically. One disadvantage of MBE for InGaN growth is the much low pressure. Therefore, according to the phase diagram (Fig. 1.11), lower growth temperature is needed to achieve high InN mole fraction. Another disadvantage is the slow growth rate (about 1 μm/h or 1 monolayer/s) [16]. The time cost is very high for industry, which limits the application of MBE technology.

1.2.2 HVPE

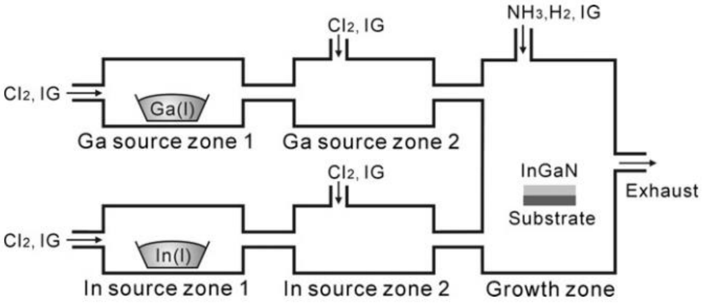

Fig. 1.5 Schematic view of the InGaN HVPE system (IG=Inert Gas) [18].

Hydride vapor phase epitaxy (HVPE) is another attractive growth methods, especially for bulk crystal growth because of high growth rate and low dislocation density. In 1977, L. A. Marasina et al. first reported InN growth by HVPE with $InCl_3$ powder and NH_3 [17]. However, the big problem of powder materials is impurity due to their hygroscopic nature. Y. Kumagai et al. calculated that InN can be grown not by InCl and NH_3 but by $InCl_3$ and NH_3 [18]. Therefore, the InGaN growth by HVPE can be performed by using two types of halides (GaCl and InCl) and two types of trihalides ($GaCl_3$ and $InCl_3$) in Fig 1.5 [19].

The chemical reactions in growth zone are as follows.

$$InCl_3(g) + NH_3(g) = InN(alloy) + 3HCl(g) \tag{1.3}$$

$$GaCl_3(g) + NH_3(g) = GaN(alloy) + 3HCl(g) \tag{1.4}$$

$$InCl(g) + Cl_2(g) = InCl_3(g) \tag{1.5}$$

$$InCl(g) + Cl_2(g) = InCl_3(g) \tag{1.6}$$

$$H_2(g) + Cl_2(g) = 2HCl(g) \tag{1.7}$$

A. Syrkin et al. first reported the InGaN based MQW structures grown by HVPE [20, 21]. The TEM image in Fig. 1.6(a) shows that the interface between well and barrier layer is rough. In Fig. 1.6(b), the satellite peak of XRD curve is also not clear. Because of high vertical growth rate, HVPE can be used for nanorods growth. H.-M. Kim et al. reported InGaN nanorods growth on (1 1 1) silicon [22]. The average diameter and length of nanorods were 50 nm and 10 μm, respectively.

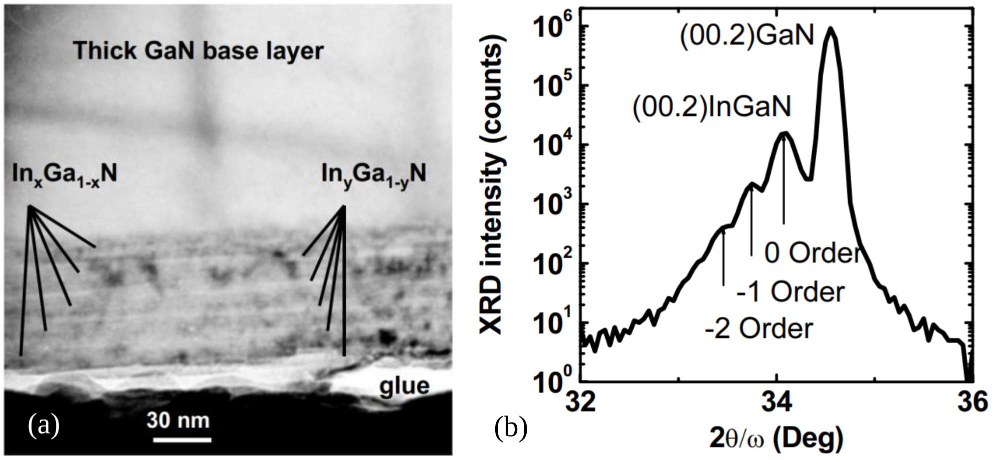

Fig. 1.6 (a) Cross sectional TEM image of HVPE grown $In_xGa_{1-x}N$ (x ~ 0.2)/$In_yGa_{1-y}N$ (y ~ 0.14) multi-layer structure. The image was taken along the [10-10] zone axis [20]; (b) HRXRD 2θ/ω scan for HVPE grown $In_xGa_{1-x}N$/$In_yGa_{1-y}N$ multi-layer structure [21].

The advantage of InGaN growth by HVPE is that it is not needed to input much NH_3 because of the strong reaction between trihalides and NH_3 [18]. On the other hand, InGaN growth by HVPE has a disadvantage that it is difficult to control the growth with step-flow growth mode due to the high growth rate at appropriate growth temperature, which will cause the rough interface.

1.2.3 MOVPE

In 1985, H. Amano et al. used low temperature AlN as a buffer layer to grow GaN successfully at first time in the world [4]. In 1989, based on this GaN growth technology T. Matsuoka et al. grew successfully InGaN by using an extremely high ammonia supply and nitrogen carrier gas [7]. In 1991, Matsuoka's group also grew InGaN at 800 ºC and high In/Ga flow rate ratio in gas phase to achieve high-quality InGaN film on sapphire [23]. In 1992, S. Nakamura et al. found that

InGaN grown on GaN films has better crystal quality than that on sapphire [24]. In 1993, S. Nakamura et al. firstly achieved Double-Heterostructure Blue-LEDs with p-GaN-n-InGaN (20 nm)-n-GaN based on this technology with GaN buffer and p-type technology [8, 9]. The output power and the external quantum efficiency is 125 μW and 0.22% at 20 mA, respectively [9]. Then, they grew InGaN multi-quantum-well structure (MQW) with 3 nm well and 3 nm barrier to decrease the misfit dislocation in the thick InGaN layer caused by the stress because of lattice mismatch and improve the crystal quality of InGaN layer [25]. As a result, the PL intensity is about twice as strong as that of InGaN thick film.

In 1994, Y. Kato et al. first reported that selective area growth (SAG) of GaN and AlGaN on GaN/sapphire template by MOVPE [26]. GaN layer was first grown on sapphire substrate using an AlN buffer layer and then SiO_2 mask was deposited by RF sputtering. A mask pattern was made by photolithography to form linear windows. Because GaN can not grow on SiO_2, GaN just grow in the window where GaN was exposed and form island. The lateral vapor phase diffusion of gas which flows from the mask region to the window region because of the source gas concentration gradient will lead to the ridge growth [26]. The GaN shape was controlled by growth parameters or window size which causes the different lateral growth rate and the different coalescence time of GaN islands [27]. O.-H. Nam et al. showed that there is no threading dislocation in the wing range [28].

In 1997, A. Sakai et al. first reported that GaN growth was achieved by epitaxially laterally overgrown (ELOG) technology in HVPE to decrease threading dislocation density (TDD) [29]. GaN layer was regrown on SiO_2-stripe-patterned GaN layers. TDD was decreased from 10^{10} to 10^7 cm^{-2} because of a change of a propagation direction of the dislocations during GaN growth [30]. Then G. Fasol and S. Nakamura reported the blue emission laser diode (LD) grown on GaN layer by ELOG in 1997 respectively [31, 32]. The lifetime of LD improved from only 27 h to above 3000 h [32].

ELOG technology can effectively reduce the treading dislocation, however, samples have to be put into MOVPE twice. Such regrowth is complex and could often bring into some problem and result in a lower production yield [33]. In 2001, K. Tadatomo et al. reported that InGaN LED was fabricated on patterned sapphire substrates [34]. The GaN layer was grown by lateral epitaxy on patterned sapphire substrates to decrease dislocation density to 1.5×10^{8} cm^{-2}. Besides the low threading dislocation density, patterned sapphire substrate also improve the light extraction efficiency in Table 1.3 [34]. Then some researchers redesigned the pattern of sapphire substrate to increase the light extraction efficiency [35-37]. Now PSS has been widely applied in factories.

Table 1.3 Comparison of the LEPS-UV-LED (sample A) and the CSS-UV-LED (sample B) [34]

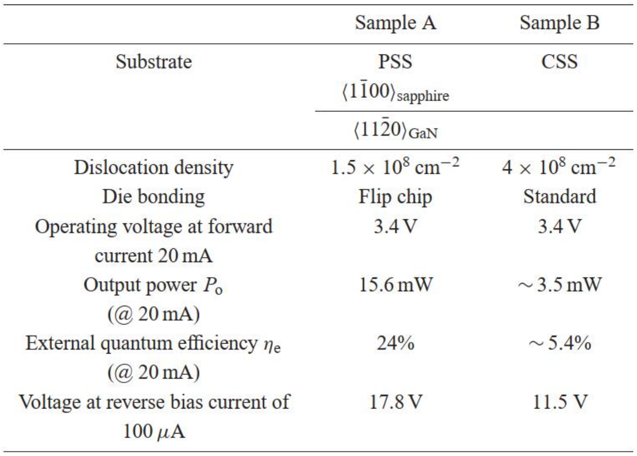

	Sample A	Sample B
Substrate	PSS $\langle 1\bar{1}00\rangle_{\text{sapphire}}$	CSS
	$\langle 11\bar{2}0\rangle_{\text{GaN}}$	
Dislocation density	$1.5 \times 10^{8}\ \text{cm}^{-2}$	$4 \times 10^{8}\ \text{cm}^{-2}$
Die bonding	Flip chip	Standard
Operating voltage at forward current 20 mA	3.4 V	3.4 V
Output power P_{o} (@ 20 mA)	15.6 mW	~ 3.5 mW
External quantum efficiency η_{e} (@ 20 mA)	24%	~ 5.4%
Voltage at reverse bias current of 100 μA	17.8 V	11.5 V

1.3 High InN-mole-fraction InGaN growth

Solid state lighting has some advantage such as high efficiency, long life-time and environmental friendly nature. LEDs have already replaced traditional lamps in some lighting systems, including street light, traffic lights, and displays. Nowadays, the most common white light based on LEDs is achieved by the combination between blue light from LED and yellow light from phosphor by LED pumping. This two-color system has a color rendering index (CRI) of 70-80 and a correlated color temperature (CCT) of 4000-8000K. Although this light system is suitable for some applications, such as outdoor lighting, it is not adequate for indoor illumination applications which require with higher CRI (> 80) and lower (warmer) CCT (~3200K) compared with fluorescent lamps [38]. Therefore, three-color system is created by using red and green (or yellow) phosphor with blue LED in Fig. 1.7(a). The CRI of this system is increased to ~90, and CCT is 3000-3600K [38]. Using phosphor will lose the energy around 10%, however, the total output power of blue LED and phosphor is still high due to high quantum efficiency of blue LED. In Fig. 1.7(b), when red phosphor is replaced by red LED, a strong red emission is achieved and CCT will become further low. However, the package is complex because red and blue LED are made from different materials. In contrast to phosphor approaches, four color (RYGB) system with "multichip" in Fig. 1.7(c) will achieve CRI > 95 [39]. However, until now, the quantum efficiency of green and yellow LED is still low which are called "green gap" (Fig. 1.9).

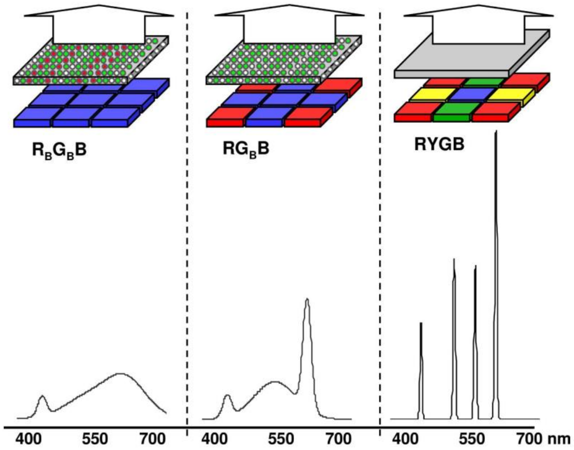

Fig. 1.7 Approaches for generating white light from LEDs and representative power spectra (the upper part is phosphor and the bottom part is LED). (a) R_BG_BB system that employs a blue LED to pump red and green phosphors. (b) Blue LED pumping a green phosphor combined with a red LED (RG_BB). (c) Four-color RYGB all-LED system (R, G, B is expressed as red, green, blue light from LED and R_B, G_B means red, green light from phosphor pumped by blue LED) [40].

The external quantum efficiency of AlInGaP drops sharply when the emission wavelength is closed to green region because the bandgap transforms to an indirect bandgap [41]. InGaN should have high quantum efficiency because of direct band gap at long wavelength. Moreover, the thermal stability of AlInGaP LEDs is not good as InGaN LEDs (Fig. 1.9(b)) because of the small band offset. Therefore, InGaN is expected to be used for long wavelength device. Until now, for violet-blue emission, high internal quantum efficiency (IQE) has been achieved [42]. For long wavelength device, such as green, amber, red emission, however, the quantum efficiency become low as shown in Fig. 1.8 [43].

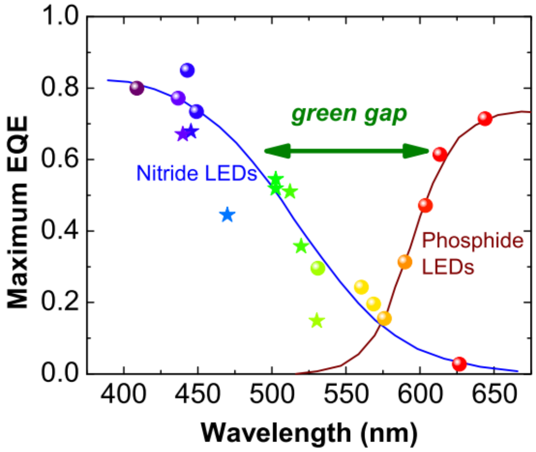

Fig. 1.8 The green gap. Maximum external quantum efficiency (EQE) of different commercial nitride and phosphide LEDs (spheres), illustrating the green gap problem [43] (Data points are taken from Ref. [46, 47]).

In 1995, S. Nakamura et al. first reported the amber InGaN-based LED with 2 nm InGaN well layer [44]. The peak wavelength and the FWHM is 590nm and 90 nm, respectively. The EQE is only 1.19%. In 1998, T. Mukai et al. reported amber InGaN LEDs with 2.5 nm InGaN well layer [45]. The EQE increased to 3.35%. The full-width at half maximum (FWHM) of the emission spectrum is 50 nm which is wider than that of AlInGaP LEDs (17 nm) in Fig. 1.9(a). They considered that the wider spectrum of amber InGaN LEDs is due to In composition fluctuation in the InGaN well layer. In 1999, they also reported a 6 nm InGaN well layer for amber emission. The EQE increased to 4.5% because of higher growth temperature [48, 49]. They also reported the red LED at the same time. However, at small current such as 1mA, the red emission disappeared and was replaced by blue emission at 470 nm possibly because of In fluctuation in the InGaN well layer.

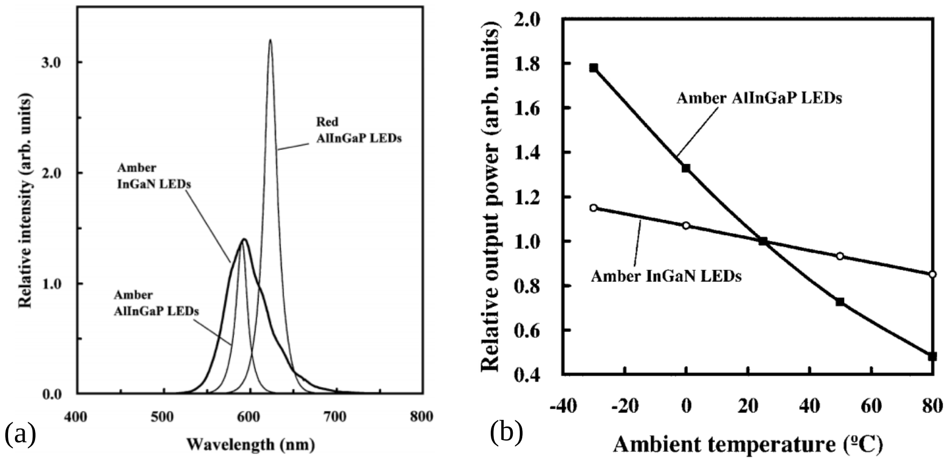

Fig. 1.9 (a) Emission spectra of amber InGaN, amber AlInGaP and red AlInGaP LEDs at a forward current of 20 mA [49]; (b) The output power of amber InGaN and AlInGaP LEDs as a function of the ambient temperature from 30 to 80 ℃. The output power of each LED was normalized to 1.0 ℃ at 25 ℃ [45].

In 2013, Toshiba research group reported the green and yellow LED [50, 51]. They used high growth rate and high growth temperature to suppress the crystal defects and used the AlGaN interlayer between InGaN well layer and GaN barrier layer to increase the EQE to 25.5% [50]. This AlGaN interlayer increases the polarity of the well layer so that it does not need so high In content for the same wavelength. On the other hand, this interlayer flatten the MQW surface. In 2014, they use this technology into the red LED and increase the EQE to 2.9% at the peak wavelength of 629 nm [52]. In 2017, K. Lee et al. reported the Ga-flow interruption technique to improve the interface between well and barrier layers for yellow InGaN LED [53].

1.3.1 Difficult of InGaN growth by MOVPE

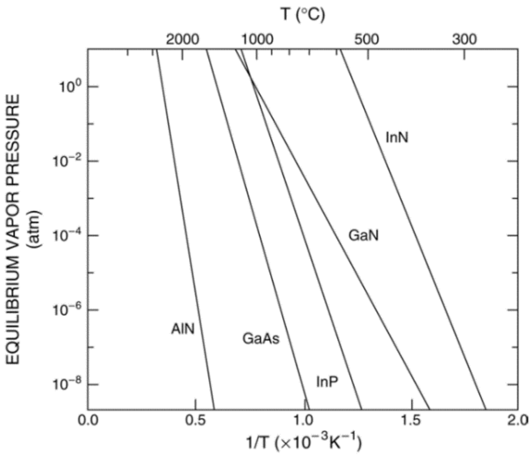

Fig. 1.10 Equilibrium vapor pressures of N_2 over AlN, GaN and InN [54]

Figure 1.10 shows the temperature dependency of the equilibrium vapor pressures of AlN, GaN, InN [54]. In Fig. 1.10, GaN and InN are grown at very different growth temperature zone. InN decompose at above 600 ℃. Therefore, low growth temperature is necessary for high InN-mole-fraction InGaN growth.

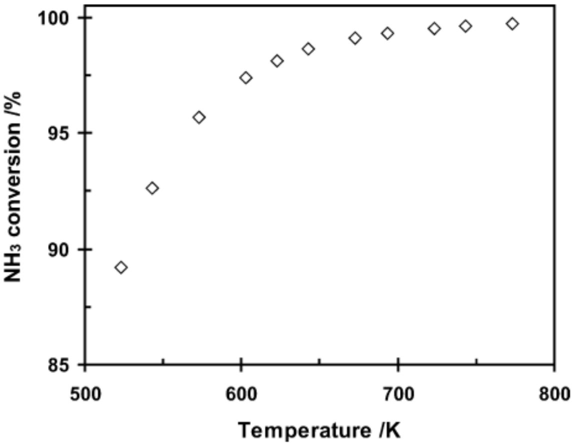

Fig. 1.11 Equilibrium conversion of NH_3 at different temperatures and 1 atm [55].

Figure 1.11 shows that more than 90% of NH_3 decompose at above 600 K in the equilibrium state [55]. However, in reality only a little NH_3 is reactive because NH_3 thermal decomposition is a sluggish reaction [56]. NH_3 is not at equilibrium state in MOVPE reactor due to high flow speed. In addition, the NH_3 decomposition rate depends on temperature, and decrease with low temperature [57, 58]. The low growth temperature will lead to low V/III ratio on the surface and cause many kinds of defects. Therefore, for InGaN growth, especially for high InN mole fraction, MOVPE has an inherent disadvantage because it must satisfy the conditions for NH_3 decomposition to form N source and for prevention of InN dissociation, which imposes conflicting temperature requirements [59].

1.3.2 Factors for low quantum efficiency and technology

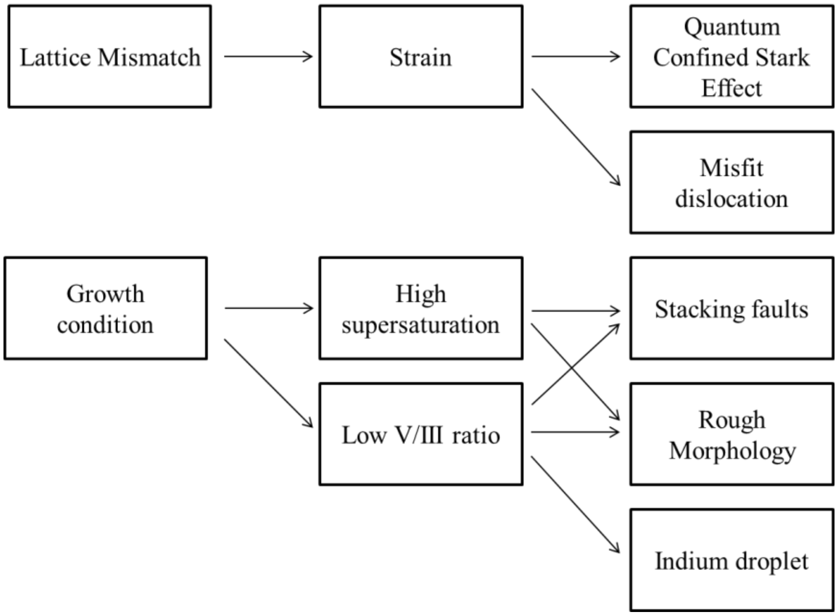

Fig. 1.12 The origin of low quantum efficiency for high In-mole-fraction InGaN growth.

The origin of low quantum efficiency for high In-mole-fraction InGaN growth is shown in Fig. 1.12. The large lattice mismatch between GaN and InN will induce large strain which leads to QCSE and misfit dislocation. On the other hand, the growth condition for high InN mole fraction is another problem which causes to many kinds of defects.

1.3.2.1 Quantum Confined Stark Effect (QCSE)

The first problem is the lattice mismatch between InGaN and GaN. With increasing InN-mole-fraction, the lattice mismatch become larger. This large mismatch will bring the biaxial stress in the well layer [60]. Therefore, the large piezoelectric field along [0001] orientation is induced because of large piezoelectric constants [61-63]. T. Takeuchi et al. observed the peak wavelength of MQW shift blue with increasing excitation power at 15 K which is caused by QCSE [64]. S. F. Chichibu et al. studied the QCSE of InGaN QW as shown in Fig. 1.13 [65, 66]. M. A. Maur et al. showed that the effect of QCSE on IQE become strong with increasing wavelength [43].

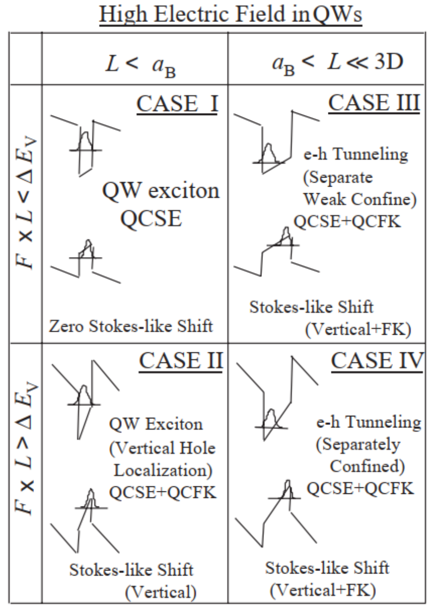

Fig 1.13 Schematic band diagrams of GaN/AlGaN or InGaN/AlGaN QWs under the electric field *F*. Each case represents the restrictions determined among the internal electric field *F*, the well width *L*, the valence band discontinuity ΔE_V and the bulk free exciton Bohr radius a_B. Note that in-plane (lateral) bandgap inhomogeneity is omitted [65].

Many researchers want to use non-polar or semi-polar (orientation) InGaN based LED to reduce the effect of QCSE on the quantum efficiency. A. E. Romanov et al. calculated the polarization effects with increasing plane orientation from c-plane (0001) as shown in Fig. 1.14

[67]. The problem of InGaN growth on semi-polar or non-polar plane is the crystal quality of GaN template. B. Leung et al. reported that undesirable facets form with H_2 carrier gas but N_2 carrier gas can achieve flat surface [68]. However, GaN growth with N_2 carrier gas has other problems such as higher impurity density. Ingrid L. Koslow et al. reported that the EQE of LED on (11-22) plane arrived to 12.5% at a peak wavelength of 556 nm [69].

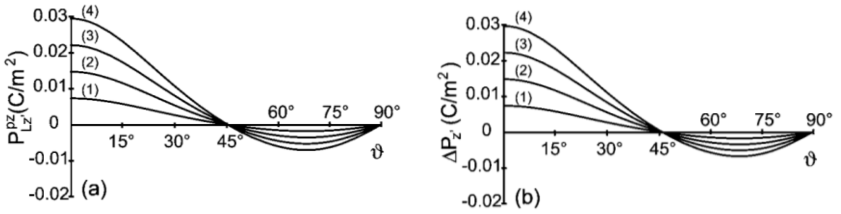

Fig. 1.14 Polarization effects in semipolar layers under biaxial compression. (a) Dependence of the piezoelectric polarization P_{Lz}^{pz} and (b) difference Pz of the total polarization on the semipolar plane orientation for InxGa1-x layers on GaN. Composition x=0.05 (1), 0.10 (2), 0.15 (3), and 0.20 (4) [67].

1.3.2.2 Misfit dislocation

When strain is accumulated to a certain account, it should be relaxed by some methods, such as pyramidal pits, misfit dislocation, 3D dots and so forth. One way is to form misfit dislocation. R. Liu et al. observed misfit dislocation in 100 nm-thick InGaN (In >11%) layer on GaN substrate by TEM as shown in Fig. 1.15(a) [70]. A network of misfit dislocations is aligned along symmetric 〈1-100〉 directions and few among them end by threading to surface. They also compared the InGaN layer on typical GaN/sapphire template with ELOG GaN/template by CL and found that InGaN on typical GaN template did not have misfit dislocations but involved pits, while InGaN on ELOG GaN template had misfit dislocations with few pits [71]. All of these proves that misfit dislocation is not due to threading dislocation from GaN underlayer. They also proposed a punch-out mechanism of misfit dislocation formation as illustrated in Fig. 1.15(b) [70]. Two simultaneous slop in **a** + **c** directions on oppositely inclined planes achieve the misfit dislocations with Burges vector **b** = 2**a**, which is also observed by TEM image in Fig. 1.15(c). Moreover, the punch-out segments must stop by new dislocations which thread through the InGaN layer. P. M. F. J. Costa et al. reported that misfit dislocation form in green MQW but not appear in blue MQW [72].

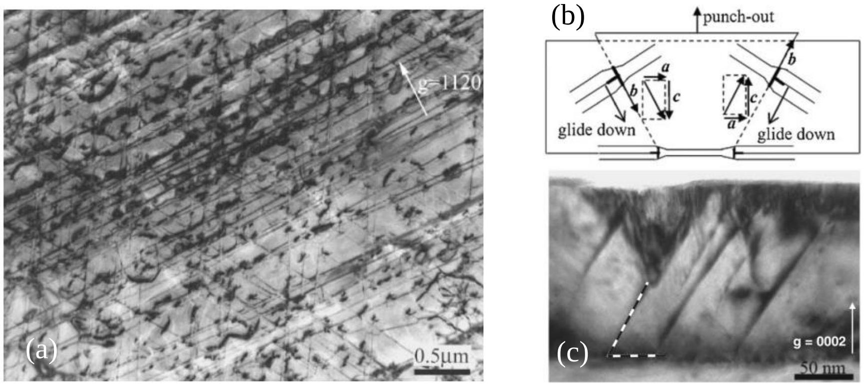

Fig. 1.15 (a) Misfit dislocation network observed in a plan-view, dark field, 400 kV TEM image of the InGaN/GaN heterojunction. Dislocations are aligned along symmetric 〈10-10〉 directions. (b) Schematic diagram illustrating plastic relaxation via a punchout relaxation process involving introduction of misfit dislocations along two oppositely inclined slip planes. (c) Cross section TEM image along a 〈1-100〉 projection [70].

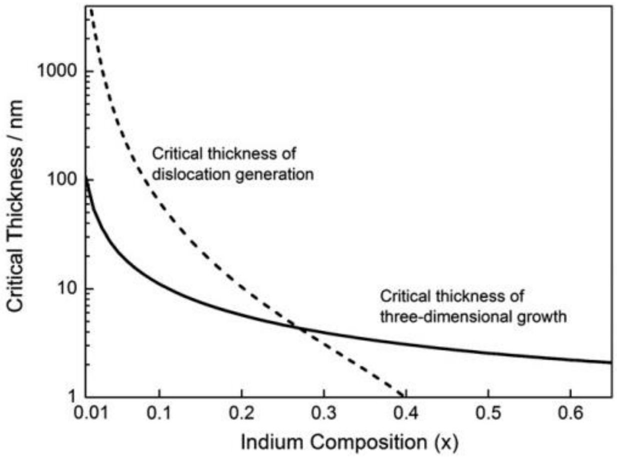

Fig. 1.16 Critical thicknesses of dislocation generation and three-dimensional growth versus indium composition x ($In_xGa_{1-x}N$) while InGaN is grown on (0 0 0 1) GaN [73].

W. Zhao et al. calculated the critical thickness of InGaN on GaN for misfit dislocation according to People and Bean's method [73]. Figure 1.16 shows that for low InN mole fraction (~0.1), the critical thickness is above 50 nm which corresponds to the data reported by R. Liu et al. Therefore, misfit dislocation does not appear in blue MQW. While, for high InN mole fraction (> 0.3), misfit dislocation should form when InGaN well layer is thicker than 3 nm. However, the critical thickness of 3D growth is related with growth condition which should not be calculated [74].

1.3.2.3 V-pits

Besides the large strain, the growth condition for high InN-mole-fraction is another main origin for low quantum efficiency. Low growth temperature or high growth rate are usually used to increase InN-mole-fraction. However, these growth condition will increase supersaturation and decrease V/III ratio, which will lead to many kinds of defects.

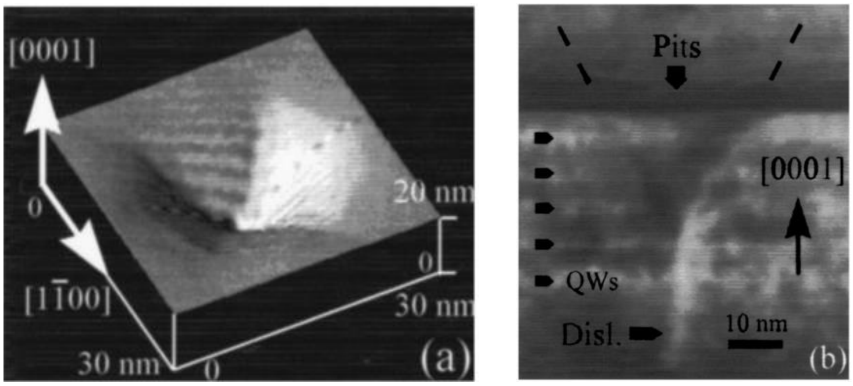

Fig. 1.17 (a) An AFM image and (b) a cross-section TEM image of a pit in five $Ga_{0.68}In_{0.32}N$ QWs [75].

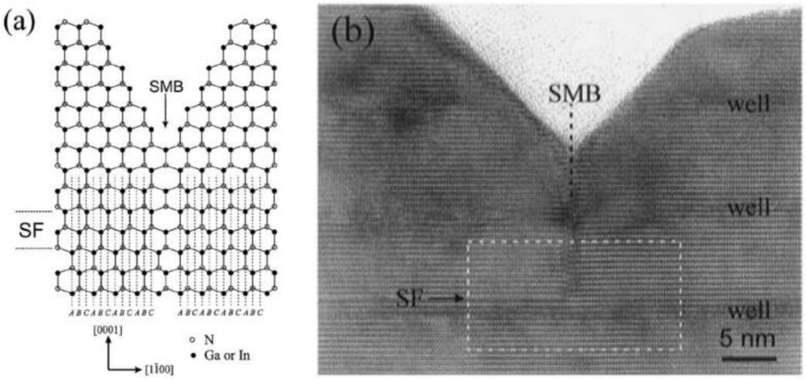

Fig. 1.18 (a) A geometrical atomic model that shows how the SMB and V-defect are generated when the faulted area of the left side meets the corrected stacked area of the right side. (b) HRTEM image showing V-defects originating from the stacking mismatch boundary induced by stacking faults in the six periods $In_{0.3}Ga_{0.7}N$/GaN MQWs [78].

V-pits is a common defect for InGaN based MQW growth. Some researchers reported the formation of V-pits [75, 76]. They found that the pits have a hexahedron cone shape with six sidewalls on <1-101> planes and are connected to threading dislocations at their bottom as shown in Fig. 1.17. K. Watanabe et al. found that V-pits preferentially starts at threading dislocations or In-rich dots under adverse growth conditions [77]. However, for high InN-mole-fraction, H. K. Cho et al. showed that some V-pits generate from the stacking mismatch boundaries induced by stacking faults rather than connected with the threading dislocations as shown in Fig. 1.18 [78, 79]. A. Kaneta et al. observed that there are some pits on the wing of ELOG for green MQW by AFM and SNOM, which proved that new TDs were generated during MQW growth and PL intensity decrease with wavelength longer than 470 nm [80].

1.3.2.4 Trench defect

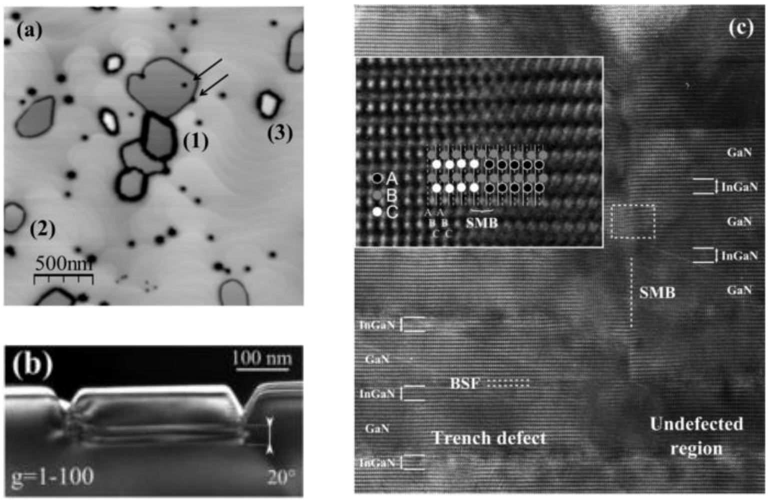

Fig. 1.19 (a) Three kinds of trench defect observed by AFM; (b) Cross section of a trench defect (zone axis 11 20) in a dark-field TEM imaging mode with g = 1-100 observed 20° away from the zone axis. (c) HRTEM image (zone axis 11-20) of the sub-surface structure of a trench defect depicting a BSF and a SMB. The atomic structure of the SMB identified by the dotted rectangle is shown on the inset [81].

F. C.-P. Massabuau et al. observed different types of trench defect which consist of a trench partially or fully enclosing a region of MQW by AFM [81]. Figure 1.19 shows that the bottom of the trench defect connects a basal plane stacking faults bounded by a stacking mismatch boundary. They suggested that either stacking mismatch boundary (SMB) as a non-radiative recombination center, or basal-plane stacking fault (BSF) which capture carriers will reduce MQW PL intensity [82]. They also found that some parts of the enclosed region of the trench defect at the top of MQW disappear and indium platelets and voids form preferentially at the bottom of MQW during the p-type layer growth, which strongly affects PL intensity [83]. F. C.-P. Massabuau et al. and J. Smalc-Koziorowska et al. reported that high barrier growth temperature reduces trench defect effectively [84, 85]. S. M. Ting et al. induced H_2 during barrier growth to decrease trench defect [86, 87].

1.3.2.5 Indium cluster

Indium cluster is another problem for high-InN-mole-fraction InGaN growth. Y.-H. Cho et al. observed the effect of indium cluster on luminescence efficiency by PL measurement [88]. S. Suihkonen et al. also reported the indium clusters by AFM [89]. A. Q. Tian et al. thought that the In cluster is from In metal on the InGaN surface and can be removed by thermal annealing [90].

In conclusion, for InGaN growth on GaN (0001) plane, the large strain due to the lattice mismatch can not be reduced in theory. Growth related defects should be focused on for improvement of high InN-mole-fraction InGaN growth in the future. For low InN-mole-fraction InGaN based MQW, there are less defects, while for high InN-mole-fraction many new defects appear even if using the same barrier growth condition. However, many published researches focused on the optimization of barrier growth condition. MOVPE as one common growth theory in factory has the inherent disadvantage for high InN-mole-fraction InGaN growth because of low NH_3 decomposition rate at lower growth temperature. Therefore, there are several issues that should be considered for high InN-mole-fraction InGaN growth by MOVPE.

(1) How to increase InN-mole-fraction without low growth temperature or high growth rate which will reduce the actual V/III ratio.

(2) How to improve InGaN growth without using high growth temperature or low growth rate which decreases InN-mole-fraction.

(3) How to improve NH_3 decomposition in reactor to increase the actual V/III ratio.

1.4. Objective of this research

High InN-mole-fraction InGaN has a great potential for future long-wavelength optoelectronic device. Despite many efforts have been devoted to an improvement of high InN-mole-fraction InGaN based MQW growth by MOVPE, the investigation of a single InGaN layer is still not enough. The crystallinity of high InN-mole-fraction InGaN based MQW is still not good as the low InN-mole-fraction MQW. Especially, it is difficult to keep InGaN layers with stepped morphology and achieve a smooth surface of MQW for high InN-mole-fraction cases. Moreover, the NH_3 effect is another important issue for the high InN-mole-fraction InGaN growth which should be paid much attention to. For a MOVPE system, there is an upper limit of the NH_3 flow rate (the maximum in this work (30 standard liter per minute (SLM)). Therefore, NH_3 decomposition rate should be considered. The objective of this research is summarized as below:

1) To investigate the morphology of single InGaN layer growth by MOVPE and analyze the morphology transformation by supersaturation.
2) To investigate the growth condition of InGaN based MQW and analyze the effect of InGaN well layer on MQW growth.
3) To study the effect of gas phase temperature for InGaN based MQW growth.

1.5. Thesis organization

In this sub-chapter, the outline of this thesis will be given. The title of this thesis is: Study of high-quality and high-indium-content InGaN growth by MOVPE.

In Chapter 1, the development history of III-nitrides and InGaN growth is introduced, respectively. And then it shows the difficult and improvement for high InN-mole-fraction InGaN growth by MOVPE. In the last part of this chapter, the objectives of this study and thesis outline are introduced.

In Chapter 2, the MOVPE system and the characterization methods during this study is introduced. And then the calculation of supersaturation is described.

In Chapter 3, single InGaN layer growth by MOVPE is studied. Three different InGaN morphology are introduced. The impact of growth conditions such as growth temperature, growth rate on InGaN growth is systematically investigated by supersaturation. And the effect of miscut angle of GaN substrate is presented in detail.

In Chapter 4, InGaN-based MQW growth is described. MQW with low InN-mole-fraction and high InN-mole-fraction are compared on GaN substrate and GaN/sapphire template. The effect of InGaN well layer on MQW growth is shown.

In Chapter 5, the effect of gas phase temperature on InGaN-based MQW growth is discussed. The temperature distribution in reactor is simulated and show the effect of different wafer tray on the gas temperature. MQWs with three different wavelengths are investigated in detail.

In Chapter 6, all the work is summarized and some suggestions for further research on high InN-mole-fraction InGaN growth are provided.

References

1. G. Cosendey, “(In,Al)N-based blue microcavity lasers” PhD Thesis, Ecole polytechnique fédérale de Lausanne (EPFL), 2013
2. M. A. Caro, “Theory of elasticity and electric polarization effects in the group-III nitrides” PhD Thesis, University College Cork, 2013
3. H. Amano, “Nobel Lecture: Growth of GaN on sapphire via low-temperature deposited buffer layer and realization of p-type GaN by Mg doping followed by low-energy electron beam irradiation” Rev. Mod. Phys., 87 (2015) 1133-1138
4. H. Amano, N. Sawaki, I. Akasaki, and Y. Toyoda, “Metalorganic vapor phase epitaxial growth of a high quality GaN film using an AlN buffer layer”, Appl. Phys. Lett. 48 (1986) 353-355.
5. S. Yoshida, S. Misawa, and S. Gonda, “Improvements on the electrical and luminescent properties of reactive molecular beam epitaxially grown GaN films by using AlN-coated sapphire substrates”, Appl. Phys. Lett. 42 (1983) 427-429
6. H. Amano, M. Kito, K. Hiramatsu, and I. Akasaki, “P-Type Conduction in Mg-Doped GaN Treated with Low-Energy Electron Beam Irradiation (LEEBI)”, Jpn. J. Appl. Phys. 28 (1989) L2112-L2114
7. T. Matsuoka, H. Tanaka, T. Sasaki and A. Katsui, “Wide-gap semiconductor (In, Ga)N”, Proc. 16th Int. Symp. on GaAs and Related Compounds, Karuizawa, 1989, Inst. Phys. Conf. Ser. 106, T. Ikoma, and H. Watanabe (Eds.) (Institute of Physics, Bristol, 1990) 141-146
8. S. Nakamura, “GaN Growth Using GaN Buffer Layer”, Jpn. J. Appl. Phys. 30 (1991) L1705.
9. S. Nakamura, M. senoh, T. Mukai, “P-GaN/N-InGaN/N-GaN Double-Heterostructure Blue-Light-Emitting Diodes”, Jpn. J. Appl. Phys. 32 (1993) L8-L11.

10. M. A. Caro, S. Schulz, and E. P. O'Reilly, "Theory of local electric polarization and its relation to internal strain: Impact on polarization potential and electronic properties of group-III nitrides", Phys. Rev. B 88 (2013) 214103
11. R. Singh and T. D. Moustakas, "Growth of InGaN Films by MBE at the Growth Temperature of GaN", Mat. Res. Soc. Symp. Proc. 395 (1996) 163-168
12. H. Lu, W. J. Schaff, J. Hwang, H. Wu, W. Yeo, A. Pharkya, and L. F. Eastman, "Improvement on epitaxial grown of InN by migration enhanced epitaxy", Appl. Phys. Lett. 77 (2000) 2548-2550
13. H. Lu, W. J. Schaff, L. F. Eastman, J. Wu, W. Walukiewicz, D. C. Look, and R. J. Molnar, "Growth of thick InN by molecular beam epitaxy", Material Research Society Symposium Proceedings, 743 (2003) L4.10.1-L4.10.6
14. C. Adelmann, J. Simon, G. Feuillet, N. T. Pelekanos, B. Daudin, and G. Fishman, "Self-assembled InGaN quantum dots grown by molecular-beam epitaxy", Appl. Phys. Lett., 76 (2000) 1570-1572
15. H. Sekiguchi, K. Kishino, and A. Kikuchi, "Emission color control from blue to red with nanocolumn diameter of InGaN/GaN nanocolumn arrays grown on same substrate", Appl. Phys. Lett. 96 (2010) 231104
16. M. A. Herman, W. Richter and H. Sitter: Epitaxy Physical Principles and Technical Implementation (Springer-Verlag Berlin Heidelberg NewYork, 2004)
17. L. A. Marasina, I. G. Pichugin, and M. Tlaczala, "Preparation of InN Epitaxial Layers in $InCl_3$-NH_3 System", Kristall Tech. 12 (1977) 541-545
18. Y. Kumagai, K. Takemoto, A. Koukitu, and H. Seki, "Thermodynamics on halide vapor-phase epitaxy of InN using InCl and $InCl_3$", J. Cryst. Growth 222 (2001) 118-124
19. K. Hanaoka, H. Murakami, Y. Kumagai, and A. Koukitu, "Thermodynamic analysis on HVPE growth of InGaN ternary alloy", J. Cryst. Growth 318 (2011) 441-445

20. A. Syrkin, V. Ivantsov, O. Kovalenkov, A. Usikov, V. Dmitriev, Z. Liliental-Weber, M. L. Reed, E. D. Readinger, H. Shen, and M. Wraback, “First all-HVPE grown InGaN/InGaN MQW LED structures for 460-510 nm”, phys. stat. sol. (c) 5 (2008) 2244-2246
21. A. Usikov, V. Soukhoveev, L. Shapovalova, A. Syrkin, O. Kovalenkov, A. Volkova, V. Sizov, V. Ivantsov, and V. Dmitriev, “New results on HVPE growth of AlN, GaN, InN and their alloys”, phys. stat. sol. (c) 5 (2008) 1825-1828
22. H. M. Kim, W. C. Lee, T. W. Kang, K. S. Chung, C. S. Yoon, C. K. Kim, “InGaN nanorods grown on (1 1 1) silicon substrate by hydride vapor phase epitaxy”, Chemical Physics Letters 380 (2003) 181-184
23. N. Yoshimoto, T. Matsuoka, T. Sasaki, and A. Katsui, “Photoluminescence of InGaN films grown at high temperature by metalorganic vapor phase epitaxy”, Appl. Phys. Lett. 59 (1991) 2251-2253
24. S. Nakamura, T. Mukai, “High-Quality InGaN Films Grown on GaN Films”, Jpn. J. Appl. Phys. 31(1992) L1457-L1459
25. S. Nakamura, T. Mukai, M. Senoh, S. Nagahama, and N. Iwasa, “$In_xGa_{(1-x)}N/In_yGa_{(1-y)}N$ superlattices grown on GaN films”, J. Appl. Phys. 74 (1993) 3911-3915
26. Y. Kato, S. Kitamura, K. Hiramatsu, and N. Sawaki, “Selective growth of wurtzite GaN and $Al_xGa_{1-x}N$ on GaN/sapphire substrates by metalorganic vapor phase epitaxy”, J. Cryst. Growth 144 (1994) 133-140
27. P. Fini, H. Marchand, J.P. Ibbetson, S.P. DenBaars, U.K. Mishra, and J.S. Speck, “Determination of tilt in the lateral epitaxial overgrowth of GaN using X-ray diffraction”, J. Cryst. Growth 209 (2000) 581-590
28. O. H. Nam, M. D. Bremser, T. S. Zheleva, and R. F. Davis, “Lateral epitaxy of low defect density GaN layers via organometallic vapor phase epitaxy”, Appl. Phys. Lett. 71 (1997) 2638-2640

29. A. Sakai, H. Sunakawa and A. Usui, “Defect structure in selectively grown GaN films with low threading dislocation density”, Appl. Phys. Lett. 71 (1997) 2259-2261
30. A. Usui, H. Sunakawa, A. Sakai, and A. A. Yamaguchi, “Thick GaN epitaxial growth with low dislocation density by hydride vapor phase epitaxy”, Jpn. J. Appl. Phys., 36 (1997) L899-L902
31. G. Fasol, “Longer Life for the Blue Laser”, Science 278 (1997) 1902-1903
32. S. Nakamura, M. Senoh, S. Nagahama, N. Iwasa, T. Yamada, T. Matsushita, H. Kiyoku, Y. Sugimoto, T. Kozaki, H. Umemoto, M. Sano, and K. Chocho, “InGaN/GaN/AlGaN-based laser diodes with modulation-doped strained-layer superlattices grown on an epitaxially laterally overgrown GaN substrate”, Appl. Phys. Lett. 72 (1998) 211-213
33. Y.P. Hsu, S.J. Chang, Y.K. Su, J.K. Sheu, C.T. Lee, T.C. Wen, L.W. Wu, C.H. Kuo, C.S. Chang, S.C. Shei, “Lateral epitaxial patterned sapphire InGaN/GaN MQW LEDs”, J. Cryst. Growth 261 (2004) 466-470
34. K. Tadatomo, H. Okagawa, Y. Ohuchi, T. Tsunekawa, Y. Imada, M. Kato and T. Taguchi, “High Output Power InGaN Ultraviolet Light-Emitting Diodes Fabricated on Patterned Substrates Using Metalorganic Vapor Phase Epitaxy”, Jpn. J. Appl. Phys. 40 (2001) L583-L585
35. D. S. Wuu, W. K. Wang, W. C. Shih, R. H. Horng, C. E. Lee, W. Y. Lin, and J. S. Fang, “Enhanced Output Power of Near-Ultraviolet InGaN-GaN LEDs Grown on Patterned Sapphire Substrates”, IEEE PHOTONICS TECHNOLOGY LETTERS, 17 (2005) 288-290
36. Y. J. Lee, J. M. Hwang, T. C. Hsu, M. H. Hsieh, M. J. Jou, B. J. Lee, T. C. Lu, H. C. Kuo, and S. C. Wang, “Enhancing the Output Power of GaN-Based LEDs Grown on Wet-Etched Patterned Sapphire Substrates”, IEEE PHOTONICS TECHNOLOGY LETTERS 18 (2006) 1152-1154

37. R. H. Horng, W. K. Wang, S. C. Huang, S. Y. Huang, S. H. Lin, C. F. Lin, and D. S. Wuu, "Growth and characterization of 380-nm InGaN/AlGaN LEDs grown on patterned sapphire substrates", J. Cryst. Growth 298 (2007) 219-222
38. M. R. Krames, O. B. Shchekin, R. Mueller-Mach, G. O. Mueller, L. Zhou, G. Harbers, and M. G. Craford, "Status and future of high-power light emitting diodes for solid-state lighting," J. Disp. Technol. 3 (2007) 160-175
39. J. M. Phillips, M. E. Coltrin, M. H. Crawford, A. J. Fischer, M. R. Krames, R. Mueller-Mach, G. O. Mueller, Y. Ohno, L. E. S. Rohwer, J. A. Simmons, and J. Y. Tsao, "Research challenges to ultra-efficient inorganic solid-state lighting," Laser Photon. Rev. 1 (2007) 307-333
40. M. H. Crawford, "LEDs for Solid-State Lighting: Performance Challenges and Recent Advances", IEEE J. Sel. Top. Quantum Electron. 15 (2009) 1028-1040
41. M. G. Craford, "LEDs challenge the incandescents", Circuits and Devices (1992) 24-29
42. Y. Narukawa, M. Ichikawa, D. Sanga, M. Sano and T. Mukai, "White light emitting diodes with super-high luminous efficacy", J. Phys. D: Appl. Phys. 43 (2010) 354002
43. M. A. Maur, A. Pecchia, G. Penazzi, W. Rodrigues, and A. D. Carlo, "Efficiency Drop in Green InGaN/GaN Light Emitting Diodes: The Role of Random Alloy Fluctuations", Phys. Rev. Lett., 116 (2016) 027401
44. S. Nakamura, M. Senoh, N. Iwasa and S. Nagahama, "High-brightness InGaN blue, green and yellow lightemitting diodes with quantum well structures", Jpn. J. Appl. Phys. 34 (1995) L797-L799
45. T. Mukai, H. Narimatsu and S. Nakamura, "Amber InGaN-Based Light-Emitting Diodes Operable at High Ambient Temperatures", Jpn. J. Appl. Phys. 37 (1998) L479-L481
46. K. A. Bulashevich, A. V. Kulik, and S. Y. Karpov, "Optimal ways of colour mixing for high-quality white-light LED sources", Phys. Status Solidi (a) 212 (2015) 914-919

47. D. Schiavon, M. Binder, M. Peter, B. Galler, P. Drechsel, and F. Scholz, "Wavelength-dependent determination of the recombination rate coefficients in single-quantum-well GaInN/GaN light emitting diodes", Phys. Status Solidi (b) 250 (2013) 283-290
48. T. Mukai, M. Yamada and S. Nakamura, "Characteristics of InGaN-Based UV/Blue/Green/Amber/Red Light-Emitting Diodes", Jpn. J. Appl. Phys. 38 (1999) 3976-3981
49. T. Mukai, "Recent Progress in Group-III Nitride Light-Emitting Diodes", IEEE J. Sel. Top. Quantum Electron. 8 (2002) 264-270
50. R. Hashimoto, J. Hwang, S. Saito and S. Nunoue, "High-efficiency green-yellow light-emitting diodes grown on sapphire (0001) substrates", Phys. Status Solidi C 10 (2013) 1529-1532
51. S. Saito, R. Hashimoto, J. Hwang and S. Nunoue, "InGaN light-emitting diodes on c-face sapphire substrates in green gap spectral range", Appl. Phys. Express 6 (2013) 111004
52. J. Hwang, R. Hashimoto, S. Saito and S. Nunoue, "Development of InGaN-based red LED grown on (0001) polar surface", Appl. Phys. Express 7 (2014) 071003
53. K. Lee, H. Lee, C.-R. Lee, T.-H. Chung, Y. S. Kim, J.-Y. Leem, K.-U. Jeong, and J. S. Kim, "Yellow-red light-emitting diodes using periodic Ga-flow interruption during deposition of InGaN well", Opt. Express 25 (2017) 15152-15160
54. T. Matsuoka, "Progress in nitride semiconductors from GaN to InN-MOVPE growth and characteristics", Superlattices and Microstructures 37 (2005) 19-32
55. S. F. Yin, B. Q. Xu, X. P. Zhou, and C. T. Au, "A mini-review on ammonia decomposition catalysts for on-site generation of hydrogen for fuel cell applications", Appl. Catalysis A: General 277 (2004) 1-9
56. V. S. Ban, "Mass Spectrometric Studies of Vapor-Phase Crystal Growth II. GaN", J. Electrochem. Soc. 119 (1972) 761-765

57. S. Kim, K. Lee, H. Lee, K. Park, C-S. Kim, S-J. Son, K-W. Yi, “The influence of ammonia pre-heating to InGaN films grown by TPIS-MOCVD”, J. Cryst. Growth 247 (2003) 55-61
58. S. F. Yin, Q. H. Zhang, B. Q. Xu, W. X. Zhu, C. F. Ng, and C. T. Au, “Investigation on the catalysis of COx-free hydrogen generation from ammonia”, J. Catal. 224 (2004) 384-396
59. T. D. Veal, C. F. McConville, and W. J Schaff: Indium Nitride and Related Alloys, Taylor and Francis Group, LLC (2010)
60. T. Takeuchi, H. Takeuchi, S. Sota, H. Sakai, H. Amano and I. Akasaki, “Optical Properties of Strained AlGaN and GaInN on GaN”, Jpn. J. Appl. Phys. 36 (1997) L177-L179
61. A. Bykhovski, B. Gelmont, M. Shur and A. Khan, “Current-voltage characteristics of strained piezoelectric structures”, J. Appl. Phys. 77 (1995) 1616-1620
62. A. D. Bykhovski, V. V. Kaminski, M. S. Sur, Q. C. Chen and M. A. Khan, “Piezoresistive effect in wurtzite n-type GaN”, Appl. Phys. Lett. 68 (1996) 818-819
63. G. Martin, A. Botchkarev, A. Rockett and H. Morkoc, “Valence-band discontinuities of wurtzite GaN, AlN, and InN heterojunctions measured by x-ray photoemission spectroscopy”, Appl. Phys. Lett. 68 (1996) 2541-2543
64. T. Takeuchi, S. Sota, M. Katsuragawa, M. Komori, H. Takeuchi, H. Amano and I. Akasaki, “Quantu-Confined Stark Effect due to Piezoelectric Fields in GaInN Strained Quantum Wells”, Jpn. J. Appl. Phys. 36 (1997) L382-L385
65. S. F. Chichibu, T. Sota, K. Wada, S. P. DenBaars, S. Nakamura, “Spectroscopic Studies in InGaN Quantum Wells”, MRS Internet J. Nitride Semicond. Res. 4S1, G2.7 (1999)
66. S. F. Chichibu, A. Shikanai, T. Deguchi, A. Setoguchi, R. Nakai, H. Nakanishi, K. Wada, S. P. Denbaars, T. Sota and S. Nakamura, “Comparison of Optical Properties of GaN/AlGaN and InGaN/AlGaN Single Quantum Wells”, Jpn. J. Appl. Phys. 39 (2000) 2417-2424
67. A. E. Romanov, T. J. Baker, S. Nakamura, and J. S. Speck, “Strain induced polarization in wurtzite III-nitride semipolar layers,” J. Appl. Phys. 100 (2006) 023522

68. B. Leung, D. L. Wang, Y.-S. Kuo, K. L. Xiong, J. Song, D. Chen, S. H. Park, S. Y. Hong, J. W. Choi, and J. Han, "Semipolar (20-21) GaN and InGaN quantum wells on sapphire substrates", Appl. Phys. Lett. 104 (2014) 262105
69. I. L. Koslow, M. T. Hardy, P. S. Hsu, P. Y. Dang, F. Wu, A. Romanov, Y. R. Wu, E. C. Young, S. Nakamura, J. S. Speck and S. P. DenBaars, "Performance and polarization effects in (11-22) long wavelength light emitting diodes grown on stress relaxed InGaN buffer layers", Appl. Phys. Lett. 101 (2012) 121106
70. R. Liu, J. Mei, S. Srinivasan, H. Omiya, F. A. Ponce, D. Cherns, Y. Narukawa and T. Mukai, "Misfit Dislocation Generation in InGaN Epilayers on Free-Standing GaN", Jpn. J. Appl. Phys. 45 (2006) L549-L551
71. S. Srinivasan, L. Geng, R. Liu, F. A. Ponce, Y. Narukawa, and S. Tanaka, "Slip systems and misfit dislocations in InGaN epilayers", Appl. Phys. Lett. 83 (2003) 5187-5189
72. P. M. F. J. Costa, R. Datta, M. J. Kappers, M. E. Vickers, C. J. Humphreys, D. M. Graham, P. Dawson, M. J. Godfrey, E. J. Thrush, and J. T. Mullins, "Misfit dislocations in In-rich InGaN/GaN quantum well structures", phys. stat. sol. (a) 203 (2006) 1729-1732
73. W. Zhao, L. Wang, J. X. Wang, Z. B. Hao, and Y. Luo, "Theoretical study on critical thicknesses of InGaN grown on (0 0 0 1) GaN", J. Cryst. Growth 327 (2011) 202-204
74. N. Grandjean and J. Massies, "Epitaxial growth of highly strained $In_xGa_{1-x}As$ on GaAs(001): the role of surface diffusion length", J. Cryst. Growth 134 (1993) 51-62
75. Y. Chen, T. Takeuchi, H. Amano, I. Akasaki, N. Yamada, Y. Kaneko, and S. Y. Wang, "Pit formation in GaInN quantum wells", Appl. Phys. Lett., 72 (1998) 710-712
76. X. H. Wu, C. R. Elsass, A. Abare, M. Mack, S. Keller, P. M. Petroff, S. P. DenBaars, J. S. Speck, and S. J. Rosner, "Structural origin of V-defects and correlation with localized excitonic centers in InGaN/GaN multiple quantum wells", Appl. Phys. Lett. 72 (1998) 692-694

77. K. Watanabe, J. R. Yang, S. Y. Huang, K. Inoke, J. T. Hsu, R. C. Tu, T. Yamazaki, N. Nakanishi, and M. Shiojiri, “Formation and structure of inverted hexagonal pyramid defects in multiple quantum wells InGaN/GaN”, Appl. Phys. Lett. 82 (2003) 718-720
78. H. K. Cho, J. Y. Lee, C. S. Kim, G. M. Yang, N. Sharma, and C. Humphreys, “Microstructural characterization of InGaN/GaN multiple quantum wells with high indium composition”, J. Cryst. Growth 231 (2001) 466-473
79. H. K. Cho, J. Y. Lee, G. M. Yang and C. S. Kim, “Formation mechanism of V defects in the InGaN/GaN multiple quantum wells grown on GaN layers with low threading dislocation density”, Appl. Phys. Lett. 79 (2001) 215-217
80. A. Kaneta, M. Funato, and Y. Kawaka, “Nanoscopic recombination processes in InGaN/GaN quantum wells emitting violet, blue, and green spectra”, Phys. Rev. B 78 (2008) 125317
81. F. C. P. Massabuau, S. L. Sahonta, L. Trinh-Xuan, S. Rhode, T. J. Puchtler, M. J. Kappers, C. J. Humphreys, and R. A. Oliver, “Morphological, structural, and emission characterization of trench defects in InGaN/GaN quantum well structures”, Appl. Phys. Lett. 101 (2012) 212107
82. F. C. P. Massabuau, L. Trinh-Xuan, D. Lodié, E. J. Thrush, D. Zhu, F. Oehler, T. Zhu, M. J. Kappers, C. J. Humphreys, and R. A. Oliver, “Correlations between the morphology and emission properties of trench defects in InGaN/GaN quantum wells”, J. Appl. Phys. 113 (2013) 073505
83. F. C. P. Massabuau, M. J. Davies, F. Oehler, S. K. Pamenter, E. J. Thrush, M. J. Kappers, A. Kovács, T. Williams, M. A. Hopkins, C. J. Humphreys, P. Dawson, R. E. Dunin-Borkowski, J. Etheridge, D. W. E. Allsopp, and R. A. Oliver, “The impact of trench defects in InGaN/GaN light emitting diodes and implications for the “green gap” problem”, Appl. Phys. Lett. 105 (2014) 112110
84. F. C. P. Massabuau, A. L. Fol, S. K. Pamenter, F. Oehler, M. J. Kappers, C. J. Humphreys, and R. A. Oliver, “The impact of growth parameters on trench defects in InGaN/GaN quantum wells”, Phys. Status Solidi A 211 (2014) 740-743

85. J. Smalc-Koziorowska, E. Grzanka, R. Czernecki, D. Schiavon, and M. Leszczynski, “Elimination of trench defects and V-pits from InGaN/GaN structures”, Appl. Phys. Lett. 106 (2015) 101905

86. S. M. Ting, J. C. Ramer, D. I. Florescu, V. N. Merai, B. E. Albert, A. Parekh, D. S. Lee, D. Lu, D. V. Christini, L. Liu, and E. A. Armour, “Morphological evolution of InGaN/GaN quantum-well heterostructures grown by metalorganic chemical vapor deposition”, J. Appl. Phys. 94 (2003) 1461-1467

87. D. I. Florescu, S. M. Ting, J. C. Ramer, D. S. Lee, V. N Merai, A. Parkeh, D. Lu, and E. A. Armour, “Investigation of V-Defects and embedded inclusions in InGaN/GaN multiple quantum wells grown by metalorganic chemical vapor deposition on (0001) sapphire”, Appl. Phys. Lett. 83 (2003) 33-35

88. Y.-H. Cho, S. K. Lee, H. S. Kwack, J. Y. Kim, K. S. Lim, H. M. Kim, T. W. Kang, S. N. Lee, M. S. Seon, O. H. Nam, and Y. J. Park, “Carrier loss and luminescence degradation in green-light-emitting InGaN quantum wells with micron-scale indium clusters”, Appl. Phys. Lett. 83 (2003) 2578-2580

89. S. Suihkonen, T. Lang, O. Svensk, J. Sormunen, P.T. Törmä, M. Sopanen, H. Lipsanen, M.A. Odnoblyudov, and V.E. Bougrov, “Control of the morphology of InGaN/GaN quantum wells grown by metalorganic chemical vapor deposition”, J. Cryst. Growth 300 (2007) 324-329

90. A. Q. Tian, J. P. Liu, L. Q. Zhang, Z. C. Li, M. Ikeda, S. M. Zhang, D. Y. Li, P. Y. Wen, F. Zhang, Y. Cheng, X. W. Fan, and H. Yang, “Green laser diodes with low threshold current density via interface engineering of InGaN/GaN quantum well active region”, Opti. Express 25 (2017) 415-421

Chapter 2 Growth, Characterization Techniques and theoretical calculation

2.1 Introduction

In this chapter, the MOVPE system used for InGaN growth in this study was first introduced. Some characterization techniques for InGaN layer and MQW in this research were also shortly summarized. The InN mole fraction and thickness of InGaN layer were characterized by X-ray Diffraction (XRD). The surface morphology was investigated by atomic force microscopy (AFM). The optical properties of InGaN was measured by photoluminescence (PL). At last, the calculation of supersaturation was shown by thermal dynamic and surface kinetics.

2.2 MOVPE system

MOVPE system is a common technique for nitride growth which has already been applied in factories. In this work, MOVPE system is made by TAIYO NIPPON SANSO CORPORATION. Figure 2.1 is a photograph of the MOVPE system used in this work. It is composed of three main parts: the growth chamber, the gas panel, and the sources panel. A pump and a butterfly valve are connected to the exit of the growth chamber to control the reactor pressures from 400 to 1500 hPa. There is a horizontal reactor in the chamber as illustrated in Fig. 2.2. Quartz flow channel was put at the top and bottom which limits the growth temperature below 1300 °C. The inset line was divided into three parts. The upper line is carrier gas line involving H_2/N_2. The middle line is MO source line and the bottom line is NH_3 line.

Fig. 2.1 Photograph of TAIYO NIPPON SANSO MOVPE SR-2000 system.

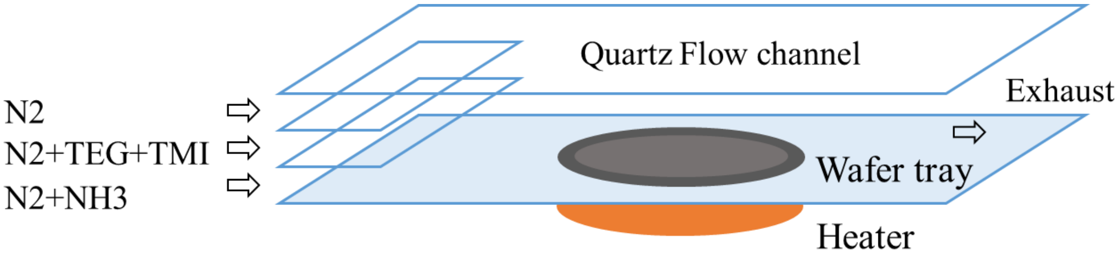

Fig. 2.2 Schematic of the configuration of the reactor.

2.3 Characterization techniques

2.3.2 Photoluminescence (PL)

PL is applied widely to examine optical properties of InGaN based QW structures with no destruction. The instrument basically includes five parts: laser, sample stage, monochromator, detector and some lens. Figure 2.3 shows a simple working principle of photoluminescence. Light beam from a laser emit to the sample and electrons in the valence band (low energy level) are excited to conduction band (high energy level) by absorbing energy from photons and holes form in the valence band at the same time. Then exited electrons transmit from the conduction band to the valence band and recombine with hole. At the same time energy loss emits photons.

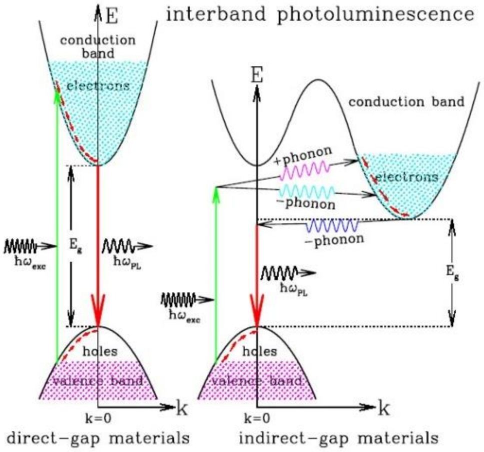

Fig. 2.3 Schematic of photoluminescence for direct-gap materials (left) and indirect-gap materials (right) [1]

In this work, micro-PL set-up was used to measure optical properties accurately. The light spot size was reduced to 1-2 μm through lens and focus on the sample by optimizing the distance between lens and samples. If the sample can be moved by stepping system, micro-PL enable us to measure the wavelength or intensity distribution on the surface which is also an important performance. If the sample stage is connected with liquid N_2 or liquid helium which can reduce the sample temperature to 77 K and 4.2 K, respectively, the PL system can be used to measure internal quantum efficiency (IQE) of the sample.

2.3.3 Atomic force microscopy (AFM)

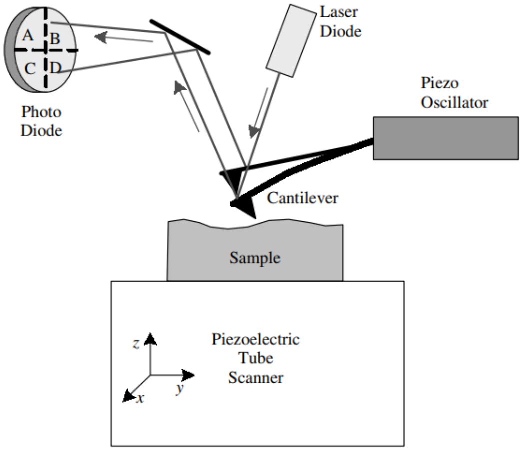

Fig. 2.4 Schematic illustration of an atomic force microscope with an optical deflection method [3].

Atomic Force Microscopy (AFM) is one of the most common scanning probe technique to analyze the surface morphology in nanoscale. AFM actually measures force between the probe and the sample. The optical deflection method is commonly adopted [2]. The principle is illustrated in Fig. 2.4 [3]. The instruments mainly involve four parts: piezo oscillator, cantilever, laser diode and photo diode. There is a sharp tip mounted on the bottom of a cantilever to touch the sample surface. A piezo oscillator provides the force to let the cantilever vibrate at a certain frequency. A laser diode emits narrow a light beam to the front of the cantilever. A photo diode is used to receive optical signals from the deflection of the cantilever and transforms them into electronic signals. If the sample surface is rough, the cantilever will bend up and down. The deflection light from the front side of the cantilever will arrive to the different position of the photo diode. Thus, the surface morphology is measured.

AFM can operate typically in three modes: contact mode, non-contact mode and tapping mode. In the contact mode, the probe tip touches the surface and is dragged across the surface during the measurement. It is easy to take a damage to both the surface of the sample and the tip because of long-time touching. In the non-contact mode, the probe tip holds above the sample surface. Therefore, the degree of bend of the tip is changed by van der Waal attractive/repulsive forces. Because these forces is generally weaker than the contact mode force, the provided resolution is lower than the contact mode. Tapping mode place the tip in contact with the sample surface to provide high resolution and then lift the tip off the surface to avoid breaking the surface. Therefore, the tapping mode is applied widely nowadays. First, the cantilever is oscillated by piezoelectric crystal near the cantilever's resonant frequency to achieve the maximum amplitude. Then, the oscillating tip is moved to the surface until it begins to lightly touch and lift off the surface. During the scanning, the tip touch and lift off the surface at a certain frequency. When the tip touch the surface, the oscillating energy loss and the oscillation amplitude decreases. The oscillation amplitude of the tip is measured and feedback to the system. The system adjusts to keep amplitude constant. The adjusted value is used to express the surface morphology.

2.3.4 X-ray diffraction (XRD)

X-ray diffraction (XRD) is one common way for characterizing crystal quality. XRD is ideal analysis tool for III-nitrides because of non-destruction, high strain sensitivity. A typical XRD equipment mainly involves three parts: X-ray generator, sample stage with three axes, detector. In front of the detector and generator there are some crystals to make X-ray beam monochromatic. X-ray are usually generated by bombarding metal target (made of typically Cu) with electrons in the tube. X-ray beams with a certain wavelength (λ) emit to the sample and are scattered by the electron cloud surrounding each atom in the crystal. The diffracted beams from different positions of the crystal will make interference in space and form the intensity distribution. According to Bragg's law, interference is related with the distance d between the two planes from which diffraction occurs and the angle θ at which the incident monochromatic beams go into the plane. This method is illustrated in the equation (2.1) and Fig. 2.5(a). In this work, the author uses PANalytical X'Pert MRD system by Philips (Fig. 2.5(b)).

$$n\lambda = 2d\sin\theta \tag{2.1}$$

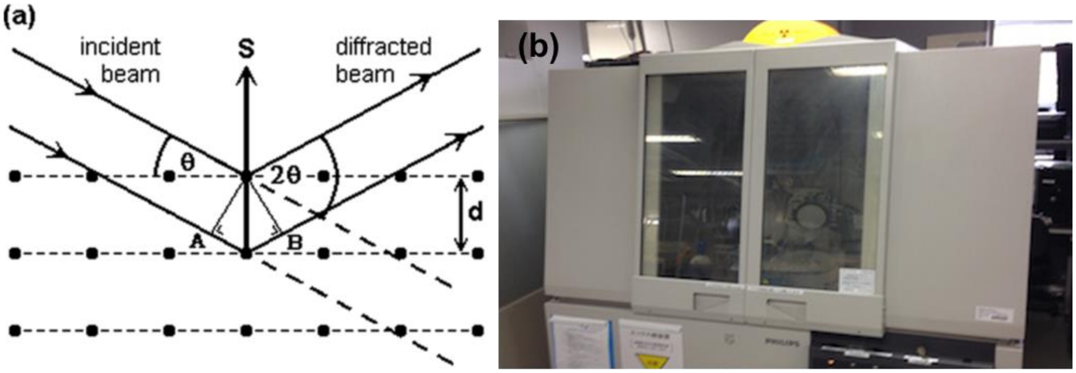

Fig. 2.5 (a) Schematic of X-ray diffraction with Bragg's law. Atom planes are indicated by dotted lines [4]. (b) Photograph of PANalytical X'Pert MRD system used in this work.

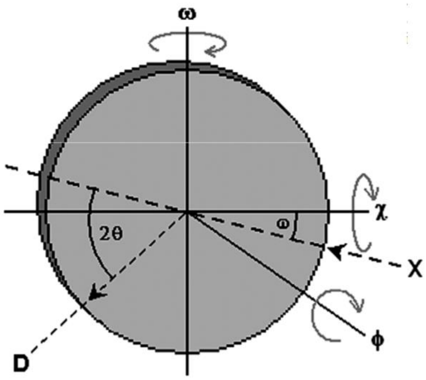

Fig 2.6 the axes of rotation [4]

There are four axes of sample rotation in Fig. 2.6 and seven scan types which are summarized in table 2.1 [4]. In this work, the author mainly uses $2\theta - \omega$ san to measure the InN mole fraction and thickness of InGaN layer and MQWs.

Table 2.1 Seven available scan types on diffractometers [4]

Scan type	Description
ω	The detector and the beam source keep stationary and the sample rotate around the ω axis. In reciprocal space, ***S*** traces an arc around the origin. The length of ***S*** keeps the same, but its direction changes.
2θ	The sample and source keep still and the detector move around the ω axis. ***S*** move along the circumference of the Ewald sphere. Both the length and the direction of ***S*** change.
ω-2θ	The sample rotate around ω axis and the detector rotate around 2θ axis with an angular ratio of 1 : 2 at the same time. In reciprocal space, ***S*** moves outwards from the origin. The *length* of ***S*** changes, but its *direction* remains the same. The x-axis is in units of 2θ.
2θ-ω	The same scan with ω-2θ scan, but the x-axis is in units of ω.
ϕ	Rotation of the sample about the ϕ axis (usually used for scanning in the asymmetric plane).
χ	The sample rotate around the χ axis. The detector and the beam source keep stationary.
Q	Keep a certain ω and scan 2θ in the set range. Then ω move a step and scan 2θ in the whole range again until ω can finish in the range. ***S*** scan in an area of the reciprocal space and reciprocal space mapping is achieved.

2.3.5 Transmission electron microscopy (TEM)

To characterize MQW structure, transmission electron microscopy (TEM) with a high resolution is often used because of the nanoscale layers. In principle, TEM is similar to optical microscopes with a series of lenses for magnifying the sample. The resolution of TEM (<0.1nm) is so high because the numerical aperture $NA \approx 0.01$ and the wavelength of electron (0.004 nm) is short. The magnification of TEM is several hundred thousand which is better than optical microscopy. Figure 2.7 shows the schematic of a typical TEM instrument [5]. Electrons from an electron gun are accelerated by high voltages and then focused on the sample through the condenser lenses. Basically, a source emits a primary beam of electrons that acquires a high energy with acceleration up to 200 kV or more of voltage to be focused on a specimen with a few micron size by the use of the condense lens. The sample must be thin enough to be transparent to the electron beam which cut by focused ion beam (FIB). The transmitted and forward scattered electrons form a diffraction pattern with the structural information of samples in the back focal plane. The pattern image is magnified and projected on a fluorescent screen by lens for electronic or photographic recording.

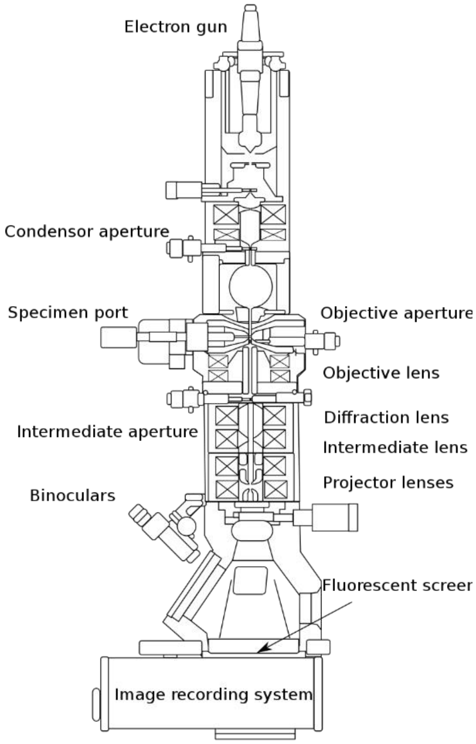

Fig. 2.7 Layout of optical components in a basic TEM [5].

Besides, scanning transmission electron microscopy (STEM) is also usually to characterize the structure of samples. In STEM, a beam with small size (~0.1 nm) transmits across the sample. Then the transmitted electrons are focused to a fixed region in the back focal plane by objective lens. The output of electron detector modulates the brightness of cathode ray tube (CRT). The primary electrons in STEM also produce secondary electrons, backscattered electrons, X-rays and cathodoluminescence which are used for other material analysis such electron energy loss spectroscopy (EELS), cathodoluminescence (CL), energy dispersive X-ray (EDX) spectroscopy.

2.4 Supersaturation

The equilibrium state of two phase is determined by the equality of their chemical potentials at a constant pressure and temperature. If the pressure or temperature is changed, the chemical potential will deviate from the equilibrium and become smaller. The phase arrives to another stable state. Therefore, any temperature or pressure change will change the stable region and lead to the transition from one phase to another. For crystal growth by MOVPE, the phase transition is from a vapor phase to a sold phase. Figure 2.8 shows the variation of the chemical potentials of the crystal and vapor phases with the pressure at a certain temperature. The chemical potential of the vapor increases with pressure along the logarithmic law, while the chemical potential of the crystal is linear with pressure. When pressure P > equilibrium pressure P_0, the chemical potential of vapor is larger than that of solid crystal, therefore, the crystal is grown. The difference of the chemical potential as a function of the pressure, which is expressed as Eq. 2.2 is called supersaturation which represents the thermodynamic driving force for crystallization [6].

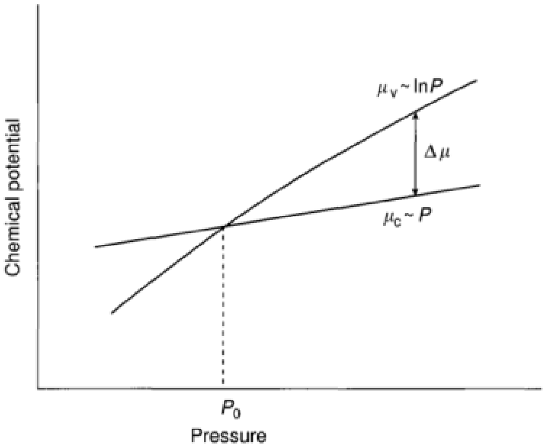

Fig. 2.8 Dependence of the chemical potentials of the vapor μ_v, and the crystal μ_c on the pressure.

2.4.1 Vapor supersaturation

In this work, the vapor supersaturation is defined as the ratio of the difference pressure to the input pressure in the following equation.

$$\sigma = \frac{P^0 - P}{P} \qquad (2.2)$$

Here, P^0 is the input partial pressure and P is the equilibrium partial pressure.

For InGaN growth, some researchers reported how to calculate the equilibrium partial [7-15]. However, in their study, undecomposed NH_3 provides N source but decomposed NH_3 prevent the nitride growth. In reality, only NH_3 decomposes to N source and joins the reaction. In this work, the author assumes that the TEG or TMG, TMI, NH_3 decomposes 100% into the Ga, In, N atom. Therefore, the reaction equations can be simply written as follows,

$$Ga(g) + NH_3(g) = GaN(s) + \frac{3}{2}H_2(g) \qquad (2.3)$$

$$In(g) + NH_3(g) = InN(s) + \frac{3}{2}H_2(g) \qquad (2.4)$$

The equilibrium equations corresponding to these reactions are as follows,

$$K_{Ga} = \frac{a_{GaN}P_{H_2}^{3/2}}{P_{Ga}P_{NH_3}} \qquad (2.5)$$

$$K_{In} = \frac{a_{InN}P_{H_2}^{3/2}}{P_{In}P_{NH_3}} \qquad (2.6)$$

where a_{GaN} and a_{InN} are the acitvities of the binary conmpounds in InGaN alloy as follows [15].

$$a_{GaN} = (1-x)\ exp[\Omega x^2/(k_BT)] \qquad (2.7)$$

$$a_{InN} = x\ exp[\Omega(1-x)^2/(k_BT)] \qquad (2.8)$$

Here, the interaction parameter $\Omega = 7000\,cal/mol$ [15].

K_{Ga} and K_{In} are the equilibrium constants of these two reactions, respectively. In this work, their value are as follows [10].

$$log_{10} K_{Ga}(T) = -12.2 + 1.78 \times 10^4/T + 1.79\, log_{10} T \qquad (2.9)$$

$$log_{10} K_{In}(T) = -13.1 + 1.13 \times 10^4/T + 2.29\, log_{10} T \qquad (2.10)$$

Because the total pressure in the reactor is kept constant during reaction, the input total pressure should be equal to the total pressure after reaction.

$$P_{Ga}^0 + P_{In}^0 + P_{NH_3}^0 + P_{N_2}^0 = P_{Ga} + P_{In} + P_{NH_3} + P_{H_2} + P_{N_2} \qquad (2.11)$$

Especially, N_2 does not join the reaction. Therefore, $P_{N_2}^0$ should be equal to P_{N_2}.

The ratio of deposited group III and group V element should be equal to 1 [16], therefore,

$$P_{Ga}^0 + P_{In}^0 - P_{Ga} - P_{In} = P_{NH_3}^0 - P_{NH_3} \qquad (2.12)$$

If a_{GaN}, a_{InN}, K_{Ga}, and K_{In} are considered as constants, Eqs (2.5), (2.6), (2.11) and (2.12) can be put together to form four equations with four unknown number, P_{Ga}, P_{In}, P_{H_2} and P_{NH_3}. The problem is how to confirm the InN mole fraction x in a_{GaN} and a_{InN}. Here, the InN mole fraction x in InGaN is approximatively defined as follows [10], because the InN mole fraction in InGaN alloy is also affected by InN decomposition from the solid state.

$$x = \frac{P_{In}^0 - P_{In}}{(P_{In}^0 - P_{In}) + (P_{Ga}^0 - P_{Ga})} \qquad (2.13)$$

Firstly, x is initialized and the equilibrium partial pressure P_{Ga} and P_{In} is calculated, and then x' is calculated according to Eq. (2.13). If $|x' - x| < 10^{-3}$, the calculation is stopped and the partial pressure P_{Ga} and P_{In} are achieved. The calculation process is expressed in Table 2.2.

Table 2.2 Flow chart of calculation process

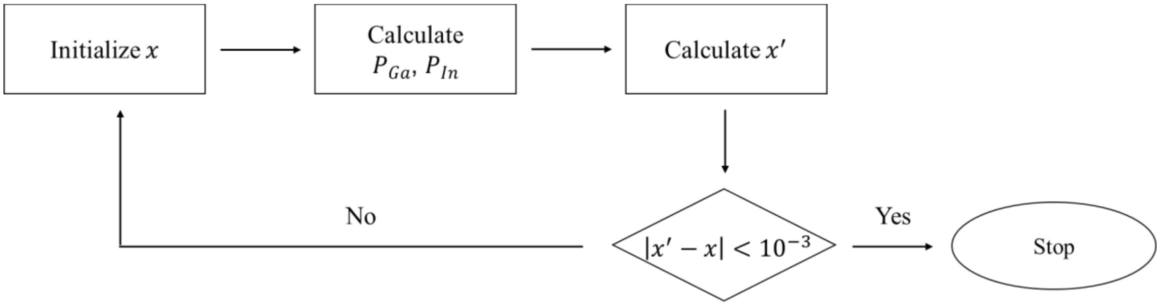

2.4.2 Surface supersaturation

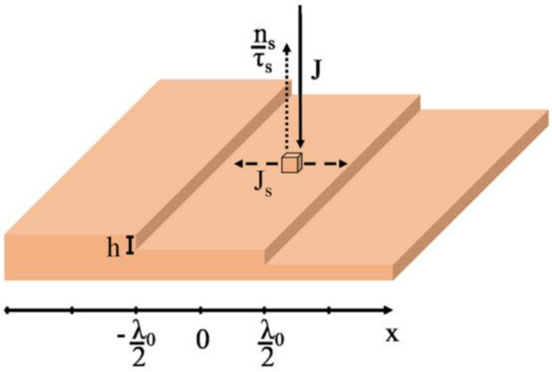

Fig. 2.9 Schematic of an ideal step and terrace morphology and the motion of species [19]

After deposition on the surface from vapor phase, atoms should move on the surface and incorporate into the right position (which usually has relatively small surface energy and more bond energy) or evaporate from the surface. If an atom incorporates into a position, the growth process is done. Therefore, if the vapor supersaturation σ is assumed as a constant above the surface, there will be a supersaturation of adsorbed atoms on the surface [18], which is defined as the surface supersaturation σ_s in this work.

$$\sigma_s = \frac{n_s - n_{s0}}{n_{s0}} \qquad (2.14)$$

where n_s is the actual adsorbed atom density on the surface which is a function of distance x. n_{s0} is the equilibrium adsorbed atom density. Here, the vapor supersaturation σ is re-defined as follows.

$$\sigma = \frac{n - n_{s0}}{n_{s0}} \qquad (2.15)$$

where n is the atom density in vapor phase.

According to Burton, Cabrera, and Frank (BCF) theory [18], the diffusion current of adsorbed atoms towards to the step, J_s, can be easily written as follows,

$$J_s = -D_s \nabla n_s = D_s n_{s0} \nabla(\sigma - \sigma_s) \qquad (2.16)$$

Where D_s is the diffusion coefficient of adsorbed atoms. There will also exist a current J_v from the vapor phase to the surface in Fig 2.

$$J_v = J - \frac{n_s}{\tau_s} = (\sigma - \sigma_s)\frac{n_{s0}}{\tau_s} \qquad (2.17)$$

Where, τ_s is the mean life of an adsorbed atom. According Einstein's relation, the diffusion length λ_s is expressed as follows,

$$\lambda_s = \sqrt{D_s\tau_s} \qquad (2.18)$$

Therefore, there exists the continuity equation

$$\nabla \cdot J_s = J_v \qquad (2.19)$$

Bring Eqs (2.15), (2.16) and (2.17) into (2.19), and get the surface supersaturation σ_s,

$$\sigma_s(x) = \sigma\left[1 - \frac{cosh\left(\frac{x}{\lambda_s}\right)}{cosh\left(\frac{\lambda_0}{2\lambda_s}\right)}\right] \qquad (2.20)$$

$$\lambda_0 = \mathrm{h}/\mathrm{tan}\theta \qquad (2.21)$$

where, λ_0 is the step width of the substrate and θ is the miscut angle of substrate. If $x = 0$, σ_s has the maximum.

$$\sigma_{s,max} = \sigma\left[1 - \frac{1}{cosh\left(\frac{\lambda_0}{2\lambda_s}\right)}\right] \qquad (2.22)$$

In this work, the maximum is used to express the average surface supersaturation. According to Eqs. (2.21) and (2.22), the surface supersaturation is not related to vaper supersaturation but also to the miscut angle of the substrate.

References

1. https://ned.ipac.caltech.edu/level5/Sept03/Li/Li4.html
2. G. Meyer and N.M. Amer, “Novel Optical Approach to Atomic Force Microscopy,” Appl. Phys. Lett. **53** (1988) 1045–1047.
3. D. K. Schroder: SEMICONDUCTOR MATERIAL AND DEVICE CHARACTERIZATION (John Wiley & Sons, Inc., Hoboken, New Jersey, 2006)
4. M. A. Moram and M. E. Vickers, “X-ray diffraction of III-nitrides”, Rep. Prog. Phys. 72 (2009) 036502
5. https://en.wikipedia.org/wiki/Transmission_electron_microscopy
6. I. V Markov: CRYSTAL GROWTH FOR BEGINNERS: Fundamentals of Nucleation, Crystal Growth and Epitaxy (World Scientific Publishing Co. Pte. Ltd., Singapore 2004)
7. A. Koukitu and H. Seki, “Unstable Region of Solid Composition in Ternary Nitride Alloys Grown by Metalorganic Vapor-Phase Epitaxy”, Jpn. J. Appl. Phys. 35 (1996) L1638-L1640
8. A. Koukitu, N. Takahashi, T. Taki and H. Seki, “Thermodynamic Analysis of $In_xGa_{1-x}N$ Alloy Composition Grown by Metalorganic Vapor Phase Epitaxy”, Jpn. J. Appl. Phys. 35 (1996) L673-L675
9. A. Koukitu, N. Takahashi and H. Seki, “Thermodynamic Study on Metalorganic Vapor-Phase Epitaxial Growth of Group III Nitrides”, Jpn. J. Appl. Phys. 36 (1997) L1136-L1138
10. A. Koukitu, N. Takahashi, T. Taki and H. Seki, “Thermodynamic analysis of the MOVPE growth of $In_xGa_{1-x}N$”, J. Cryst. Growth 170 (1997) 306-311
11. A. Koukitu and H. Seki, “Thermodynamic study on phase separation during MOVPE growth of $In_xGa_{1-x}N$”, J. Cryst. Growth 189/190 (1998) 13-18
12. A. Koukitu, T. Taki, N. Takahashi and H. Seki, “Thermodynamic study on the role of hydrogen during the MOVPE growth of group III nitrides”, J. Cryst. Growth 197 (1999) 99-105

13. J. Ou, Y.-C. Pan, W.-H. Lee, C.-K. Shu, H.-C. Lin, M.-C. Lee, W.-H. Chen, C.-I Chiang, H. Chang and W.-K. Chen, “A High-Temperature Thermodynamic Model for Metalorganic Vapor Phase Epitaxial Growth of InGaN”, Jpn. J. Appl. Phys. 38 (1999) 4958–4961
14. A. Kimura, N. Futagawa, A. Usui and M. Mizuta, “Supersaturation-dependent step-behavior of InGaN grown by metal organic vapor phase epitaxy”, J. Cryst. Growth 229 (2001) 53–57
15. Y. Kumagai, J. Kikuchi, Y. Matsuo, Y. Kangawa, K. Tanaka, and A. Koukitu, “Thermodynamic analysis of InN and $In_xGa_{1-x}N$ MOVPE using various nitrogen sources”, J. Cryst. Growth 272 (2004) 341–347
16. S. Mita, R. Collazo, A. Rice, R. F. Dalmau, and Z. Sitar , “Influence of gallium supersaturation on the properties of GaN grown by metalorganic chemical vapor deposition”, J. Appl. Phys. 104 (2008) 013521
17. A. Koukitu and H. Seki, “Thermodynamic Calculation of the VPE Growth of In1-xGaxAs by the Trichloride Method”, Jpn. J. Appl. Phys. 23 (1984) 74-78
18. W. K. Burton, N. Cabrera and F. C. Frank, “The Growth of Crystals and The Equilibrium Structure of Their Surface”, Philos. Trans. R. Soc. Ser. A 243 (1951) 299-358
19. I. Bryan, Z. Bryan, S. Mita, A. Rice, J. Tweedie, R. Collazo, and Z. Sitar, “Surface kinetics in AlN growth: A universal model for the control of surface morphology in III-nitrides”, J. Cryst. Growth 438 (2016) 81–89

Chapter 3 Morphological study of InGaN grown by MOVPE

3.1 Introduction

Since 1990s, InGaN-based quantum wells (QWs) have been active layers of light emitting diodes (LEDs) and laser diodes (LDs) with emission from violet to green. For violet-blue emission, high internal quantum efficiency (IQE) has been achieved [1]. However, for green, yellow, and even longer wavelength emission, the IQEs are much lower. There are some reasons which we analyze in Chapter 1. Besides polarization and the quantum-confined Stark effect, the increased growth-related defects also attribute to a reduction in IQE. The low growth temperature and high growth rate which are favorable for high InN mole fraction [2] cause many types of defects, such as stacking faults [3] and trench defects [4]. These defects strongly increase non-radiative recombination [5]. Although some reports optimized the surrounding of the InGaN layer [6-8], the optimization of InGaN layer itself is the best way forward.

There have been many reports on the morphology, but the terminology is quite inconsistent. Apart from a stepped morphology, one or two monolayer high islands are often reported [9-12]. These islands can be larger than the step spacing [11], and are sometimes falsely labelled as quantum dots. Moreover, these islands also yield the typical rougher upper interface of InGaN quantum wells, which has been found by atom probe tomography [13]. Quantum dots in a real sense appear later in higher-strain area and roughen the surface [14-16]. The high dislocation density of GaN/sapphire template has strong effect on InGaN morphology and the onset of 3D transition (and following relaxation) [15]. Researchers usually attributed the morphological change to the strain of InGaN. In this study, we will suggest a new insight into the morphological change by studying the morphology of InGaN grown on GaN substrate as functions of the growth condition and miscut angle of GaN substrate, and will show that step morphology has advantages for InGaN growth, and finally will compare these results to GaN/sapphire template.

Recently, GaN substrates become commercially available with low dislocation density, which is promising for InGaN-based devices [17]. In this chapter, firstly, we study the morphology of single InGaN layer grown on GaN substrate by MOVPE with different growth condition because free-standing GaN substrates with low threading dislocation density (TDD) can delete the effect of threading dislocation. Three different morphologies appeared, a stepped surface, large flat two-dimensional (2D) islands, small high three-dimensional (3D) dots. Then we analyze the morphology transition by supersaturation. The effect of miscut angle of GaN substrate on the InGaN growth is systematically investigated. The critical miscut angle from 2D islands to steps is related to growth condition. At last, compared with InGaN grown on GaN/sapphire templates, we illustrate InGaN grown on GaN substrate easily achieve stepped morphology.

In this work, single InGaN layers were grown in a horizontal MOVPE reactor shown in Chapter 2. Triethylgallium (TEG), trimethylindium (TMI) and ammonia (NH_3) were used as the gallium, indium and nitrogen sources, respectively. Trimethylgallium (TMGa) was also used to grow InGaN at high growth rate. During InGaN growth, nitrogen was used as a carrier gas, and the pressure in the reactor was kept at 500 hPa for the entire series. The InGaN layer thickness and InN mole fraction were obtained by comparing X-ray diffraction (XRD) (0002) ω-2θ measurements and kinematic diffraction simulation. Non-contact tapping mode atomic force microscope (AFM) was used to measure the surface morphology. The room temperature (RT) photoluminescence (PL) was excited by a 325nm He-Cd laser under an excitation power density of 160 kW/cm^2. Here, we defined the ratio of PL intensity at RT and at 77K as IQE.

3.2 Effect of growth condition

Table 3.1 Growth parameters of the InGaN layer on GaN substrate

Series	Sample	Miscut angle (°)	Growth temp. (℃)	TEG (μmol/min)	TMI (μmol/min)	NH_3 (mol/min)	Growth time (s)
I growth temp.	A	0.2-0.4	730	11.3	15.3	0.34	100
	B		700				
	C		670				
II growth rate	D	0.2-0.4	670	3.8	2.0	0.34	300
	E			15.1	8.1		75
	F			20.9(TMG)	11.2		34

Table 3.2 InN mole fraction, thickness, and roughness of the InGaN layer

Series	Sample	InN mole fraction	Thickness (nm)	Growth rate (nm/min)	Roughness (nm)
I growth temp.	A	0.19±0.005	4.6±0.2	2.76	0.091
	B	0.20±0.005	4.5±0.2	2.70	0.148
	C	0.24±0.005	4.5±0.2	2.70	0.221
II growth rate	D	0.18±0.005	4.4±0.2	0.84	0.112
	E	0.19±0.005	4.5±0.2	3.60	0.174
	F	0.20±0.005	4.6±0.2	8.12	0.368

Table 3.3 PL peak wavelength, FWHM, IQE of the InGaN layer on GaN substrate

Series	Sample	Peak wavelength (nm)	FWHM (nm)	IQE
I growth temp.	A	467.4±2.0	29.3±1.0	0.43
	B	495.5±2.0	30.3±1.0	0.36
	C	517.7±2.0	45.5±1.0	0.27
II growth rate	D	464.2±2.0	37.0±1.0	0.30
	E	488.4±2.0	35.0±1.0	0.23
	F	491.8±2.0	41.8±1.0	0.15

In this section, InGaN layers with 4-6 nm thickness were grown on c-plane GaN substrates in a horizontal metalorganic vapor phase epitaxy MOVPE reactor. The InGaN morphology was studied by varying temperature or changing TEG (TMG) and TMI fluxes while keeping the other conditions constant. Two series of InGaN growth parameters are summarized in Table 3.1. The

InGaN layer thickness, InN mole fraction, and roughness are shown in Table 3.2. Table 3.3 shows the PL peak wavelength, full width at half maximum (FWHM) and IQE of the InGaN layer.

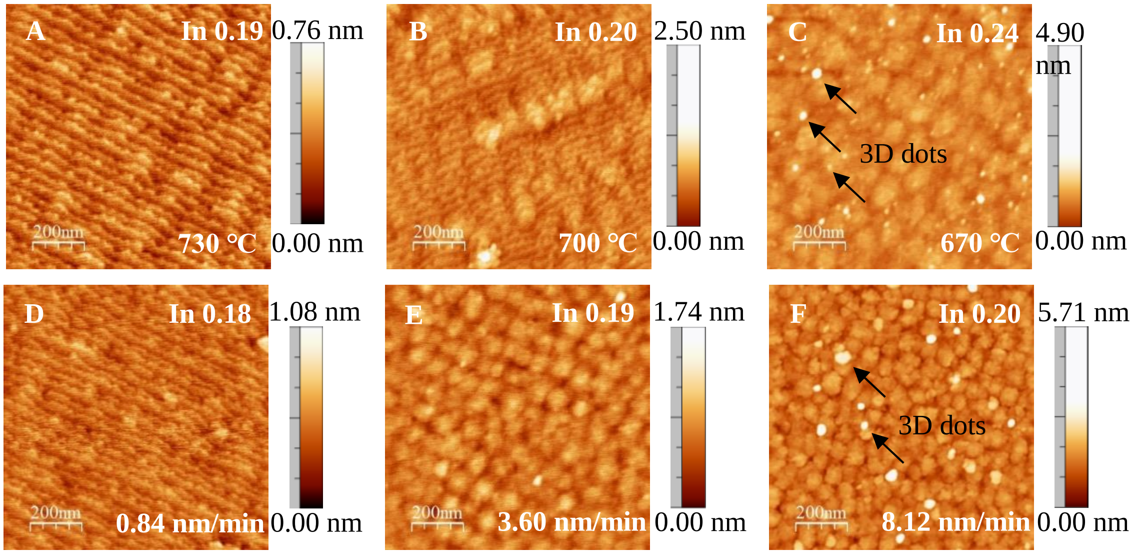

Fig. 3.1 1 μm × 1 μm AFM image of all samples. Top row is series I (InGaN layer grown at different temperatures), sample A 730 °C, sample B 700 °C, and sample C 670 °C. Bottom row is series II (InGaN layer grown with different growth rates at 670 °C), sample D at 0.84 nm/min, sample E at 3.60 nm/min, sample F at 8.12 nm/min (The vertical direction is [11-20]).

Figure 3.1 shows the AFM images of all samples. Top row is series I (InGaN grown at different growth temperatures). Sample A has a stepped morphology at 730 °C. The height of the steps is 0.25±0.02 nm, corresponding to a single monolayer of InGaN. With decreasing growth temperature to 700 °C, sample B still keeps the stepped morphology, however, flat islands start to form in some areas. The height of these islands is 0.6±0.1 nm, which is close to two monolayers (so-called two-dimensional (2D) islands). The size of these 2D islands is 120±20 nm, which exceeds the spacing of the steps given by the miscut angle. By decreasing the growth temperature to 670°C, 2D islands cover the whole surface of sample C. Additionally, three-dimensional (3D) dot-like structures appear. The size of these 3D dots is 30-50 nm with large variation. The height also has a large distribution of 1-5 nm. These findings match the results from the literature, since decreasing the growth temperature increases the InN mole fraction, triggering a transition from steps to 2D islands [9, 11] and to 3D dots [14]. However, the onset of 2D island formation was previously reported at 16% InN mole fraction [11] and for 3D dots the transition depends strongly on the accumulated strain inherently related to thickness and InN mole fraction [14, 16, 18].

Bottom row in Fig. 3.1 shows the dependence of the morphology of series II on growth rate at 670 ℃ with a constant vapor phase ratio of In/Ga. Sample D at 0.86 nm/min has stepped morphology. The step height is 0.25±0.02 nm, suggesting a single monolayer. With increasing the rate to 3.60 nm/min, the morphology of sample E changes from steps to 2D islands. The height and the size of island is 0.5±0.01 nm and 90±10 nm, respectively. With the rate increased to 8.12 nm/min, the size of 2D islands shrinks to ~60 nm and the 3D dots appear with greater density. The size of the 3D dots is 30-50 nm and the height is 2-5 nm. The density of the 3D dots is 1.4×10^9 cm^{-2}. A similar change of surface morphology has been reported for InGaN layers on GaN/sapphire templates, although there the NH_3 flow and the thickness of the layer were different [9]. Since the V/III ratio mainly governs how metal-rich the surfaces can be realized, increasing the flow of group III source should have the same effect to lowering the NH_3 flow [9].

While it generally agrees that the transition to 3D dots is governed by Stranki-Krastanov growth mode [14, 16, 18], the preceding formation of the 2D islands spanning more than a single terrace is still in a debate. Strain is often assumed to be the dominant factor, while Pristovsek et al. proposed a surface transition mode [11] where the islands would be fed from the liquid In/Ga surface layer present during the InGaN growth [19, 20]. Here, XRD data in Table 3.2 shed new insights into it: Sample A and E have the same InN mole fraction and thickness, while both morphologies are very different. Sample A has stepped morphology, while sample E has many 2D islands. Hence the appearance of 2D islands is not only controlled by strain but also dependent on the supersaturation.

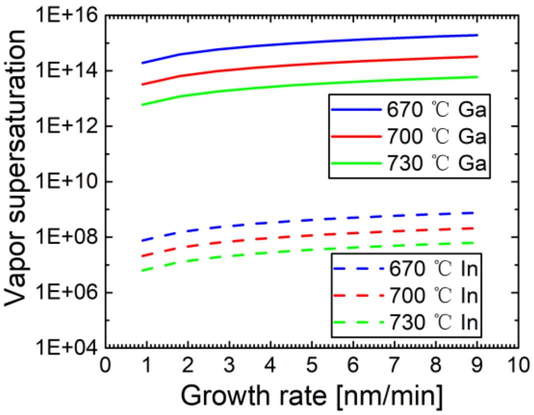

Fig. 3.2 The calculation result of vapor supersaturation of In and Ga.

According to the calculation theory in Chapter 2, the vapor supersaturation of Ga and In, σ_{Ga} and σ_{In}, can be calculated with the growth parameters in Table 3.1. Although the equilibrium partial pressures of the overlayer are hard to obtain which may change with its composition, we may well assume those values are proportional to the In and Ga vapor pressures of the crystal. Figure 3.2 shows the results of calculated vapor supersaturation versus growth rate at different temperatures. Since the supersaturation of Ga dominates over that of In by several orders of magnitude, InGaN growth depends mostly on the Ga supersaturation. However, In is also needed since GaN growth at these temperatures does not lead to the observed morphologies. Either decreasing growth temperature or increasing growth rate increases the supersaturation of Ga and In. Also, InGaN growth is under the metal rich conditions. Since Ga–Ga bonds are weak, the adatoms behave almost like a liquid film on the surface [21]. Therefore, diffusion of N atoms on the terrace would be a rate limiting step for InGaN growth. Then the nucleation sites would no longer be the step edges but rather the places where an N atom could bond to the surface. At these places InGaN would be crystallized and thus exposed as nucleation sites. The mean spacing of those 2D islands would be related to the N diffusion length on the terrace. Higher Ga supersaturation will increase the amount of metal atoms on the surface and when a critical amount is reached, then N atoms have possibility to nucleate on the terrace. Therefore, with increasing the supersaturation, the morphology changes from steps to 2D islands. Moreover, as shown in Fig 3.1, after formation the island density increases and the size decreases with decreasing growth temperature and increasing growth rate (i.e. increasing supersaturation), corresponding to shorter diffusions length as initial nucleation. Again, the nucleation seems to occur on top of the metal overlayer during growth, which is why these islands can span over multiple terraces while still show a weak coupling to the general step alignment.

In Fig. 3.1, 3D dots form after the formation of 2D islands (sample C and F). These dots are likely due to the Stranki-Krastanov (S-K) growth mode, i.e. the layer transitions to 3D growth beyond a critical wetting layer thickness [14-17]. In Table 3.2, sample F and B have the same InN mole fraction and thickness. However, 3D dots only appear in sample F, suggesting that the strain factor itself does not suffice to account for the change. In fact, the S-K transition depends on the surface energies, which will change with a different metal overlayer. A rougher surface with 2D islands will also cause non-uniform strain distribution on the surface. The larger local strain on top of the islands (due to a thicker layer) will lead to an earlier 3D dot growth. Since InGaN dots form slightly earlier on areas with more strain and grow rapidly, the size distribution of these InGaN dots is not uniform. This is different from InGaAs QDs with uniform size which form on a flat layers and thus occurs universally at the same time [22].

In Table 3.2, InN mole fraction increases with decreasing growth temperature or increasing growth rate because such growth condition decreases the desorption rate of indium. However, at the same time, the IQE becomes lower, due to either more non-radiative recombination sites led by the rougher surface or an average reduction in wave function overlap because of the non-linear change of the QCSE. Therefore, it is favorable to decrease the supersaturation to have a flat surface during high-InN-mole-fraction InGaN growth.

3.3 Effect of miscut angle of substrate

M. Leszczynski et al. reported that the morphology of InGaN layer with low InN mole fraction (In= 0.08-0.13) changed with miscut angle [23]. Moreover, some researchers showed that large miscut angle of c-plane substrate easily led to step bunching and decreased InN mole fraction [24-26]. However, the mechanism of morphology transformation and decreasing In mole fraction is unclear.

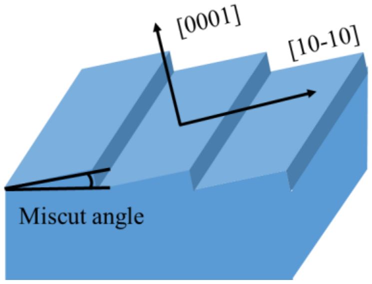

Fig. 3.3 GaN substrate with miscut angle (SCIOCS, TDD ~ 3 × 10^6 cm^{-2})

Table 3.4 Growth parameters of the InGaN layer

Series	Sample	Miscut angle (°)	Growth temp. (°C)	TEG (µmol/min)	TMI (µmol/min)	NH_3 (mol/min)	Growth time (s)
I Low T_g and high R_g	A	0.24	730	14.1	19.0	0.34	100
	B	0.33					
	C	0.42					
	D	0.51					
	E	0.97					
II Low T_g and low R_g	F	0.28	730	4.7	6.3	0.34	300
	G	0.36					
	H	0.46					
III High T_g and low R_g	I	0.26	745	4.7	6.3	0.34	300
	J	0.32					
	K	0.44					

In this section, 5.5 ± 0.2 nm thick InGaN layers were grown on c-plane GaN substrates with different miscut angles (Fig. 3.3). The effect of miscut angle was studied by varying temperature or changing TEG and TMI fluxes while keeping other conditions constant. Three series of InGaN growth parameters are summarized in Table 3.4. Table 3.5 shows InN mole fraction, PL peak wavelength and surface roughness of the InGaN layers with different growth conditions and miscut angles.

Table 3.5 InN mole fraction, PL peak wavelength and surface roughness of the InGaN layer

Series	Sample	Miscut angle (°)	InN mole fraction	Peak wavelength (nm)	Roughness (nm)
I Low T_g and high R_g	A	0.24	0.217±0.005	483.6±2.0	0.198±0.005
	B	0.33	0.224±0.005	485.1±2.0	0.192±0.005
	C	0.42	0.228±0.005	485.4±2.0	0.178±0.005
	D	0.51	0.220±0.005	480.2±2.0	0.105±0.005
	E	0.97	0.200±0.005	473.9±2.0	0.200±0.005
II Low T_g and low R_g	F	0.28	0.193±0.005	461.3±2.0	0.129±0.005
	G	0.36	0.197±0.005	460.4±2.0	0.103±0.005
	H	0.46	0.190±0.005	453.8±2.0	0.092±0.005
III High T_g and low R_g	I	0.26	0.150±0.005	433.3±2.0	0.100±0.005
	J	0.32	0.142±0.005	432.6±2.0	0.093±0.005
	K	0.44	0.130±0.005	429.0±2.0	0.093±0.005

3.3.1 Effect on morphology

Figure 3.4 shows AFM images of InGaN layers grown on GaN substrate with different miscut angles at various growth conditions. For series I, at a growth temperature of 730 °C and a growth rate of 3.3 nm/min, the InGaN morphology of sample A with 0.24° (Fig. 3.4(a)) is completely dominated with two-dimensional (2D) islands. The size of these islands is 150±10 nm and the height is 0.6±0.1 nm. For the miscut angle of 0.42°, sample C (Fig. 3.4(b)) involves some complete 2D islands and some fan-shaped step edge. The density of 2D island decreased from 3.2×10^9 cm^{-2} to 1.4×10^9 cm^{-2}. With increasing miscut angle to 0.51°, there is no 2D island in sample D (Fig. 3.4(c)) and the InGaN morphology changes totally to steps. The step height is 0.25±0.02 nm, which corresponds to monolayer. When the miscut angle increases to 0.97°, the step width (750±10 nm) and step height (1.4±0.2 nm) of sample E (Fig. 3.4(d)) become large, which corresponds to step bunching. The critical miscut angle at which the InGaN morphology changes from 2D islands to steps is between 0.42° and 0.51°.

For series II, when the growth rate decreases to 1.1 nm/min on the basis of series I, the morphology of sample F with miscut angle of 0.28° (Fig. 3.4(e)) still has 2D islands in addition to steps. At the same growth condition, the morphology of sample G (Fig. 3.4(f)) completely changes to step with miscut angle of 0.36°. The critical miscut angle is between 0.28° and 0.36°. For series III, all InGaN samples have stepped morphology with a miscut angle ranging from 0.26° (Fig. 3.4(h)) to 0.44° (Fig. 3.4(i)) at a growth temperature of 745 °C and a growth rate of 1.1 nm/min. The step width decreases from 51 nm to 31 nm. The critical miscut angle should be smaller than 0.26°.

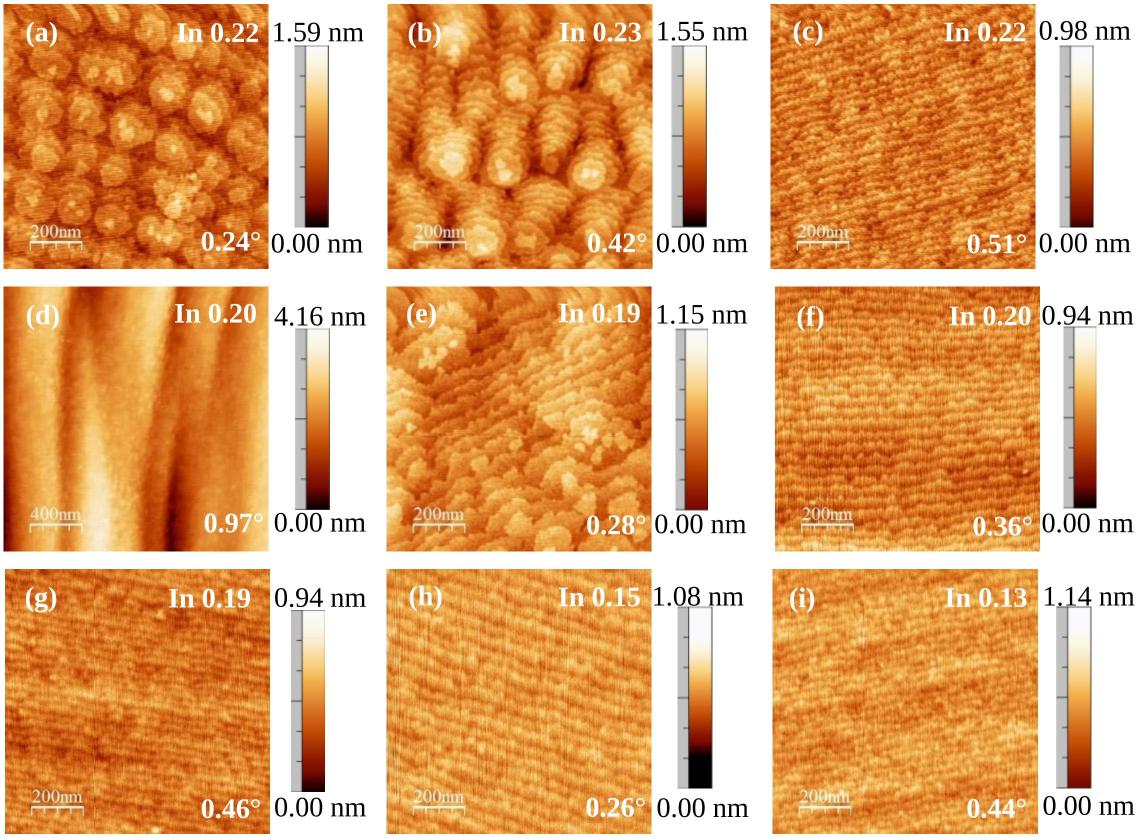

Fig. 3.4 AFM image of series I (TEG=3.8 μmol/min, TMI=5.1 μmol/min, growth temperature=730 °C), (a) sample A 0.24°, (b) sample C 0.42°, (c) sample D 0.51°, (d) sample E 0.97°; series II (TEG=3.8 μmol/min, TMI=5.1 μmol/min, growth temperature=730 °C), (e) sample F 0.28°, (f) sample G 0.36°, (g) sample H 0.46°; series III (TEG=3.8 μmol/min, TMI=5.1

μmol/min, growth temperature=745 ℃), (h) sample I 0.26°, (i) sample K 0.44° (The vertical direction is [11-20]).

M. Leszczynski et al. also showed that the InGaN morphology changed from 2D islands to steps and to step bunching with increasing miscut angle [23]. In addition, our results show that the critical miscut angle for 2D island-to-step transition decreases with higher growth temperature and lower growth rate. This transition can be explained by surface supersaturation of Ga and In.

In Chapter 2.4, the surface supersaturation can be expressed as follows,

$$\sigma_{s,max} = \sigma\left[1 - \frac{1}{cosh\left(\frac{\lambda_0}{2\lambda_s}\right)}\right] \qquad (2.22)$$

If we calculate the surface supersaturation we need to confirm the diffusion length. Equation (2.18) shows the diffusion length is related with diffusion coefficient D_S and mean lifetime τ_S of adsorbed atoms. The diffusion coefficient D_S and the mean life τ_S can be written as follows [27].

$$D_S = a^2 v' exp(-U_S/k_B T) \qquad (3.1)$$

$$1/\tau_S = v\ exp(-W_S'/k_B T) \qquad (3.2)$$

where, U_S is the activation energy between two neighbouring equilibrium positions on the surface with a distance a and W_S' is the evaporation energy from the surface to vapor phase. v and v' are the frequency factors with the order of the atomic frequency of vibration ($v{\sim}10^{13}s^{-1}$).

Bring Eqs (3.1), (3.2) into (2.18), assuming $v{\sim}v'$

$$\lambda_S = \sqrt{D_S\tau_S} = a\ exp\left[\left(W_s^{'} - U_s\right)/2k_B T\right] \qquad (3.3)$$

If assuming $\mathrm{Q} = W_S' - U_S$, the diffusion length λ_S is a function of temperature with two unknown number. Therefore, we assume the diffusion length λ_S keeps constant with the same growth temperature.

$$\lambda_S = a\ exp(Q/2k_B T) \qquad (3.3)$$

At the critical miscut angle, the InGaN morphology changes from steps to 2D islands which means the growth mode change from step-flow to 2D-nucleation. The supersaturation of 2D-nucleation can be expressed as follows [28, 29],

$$\sigma_{2D} = \alpha - 1 = exp\left(\frac{\Omega\pi h\varepsilon^2}{(65 - \ln J_{2D})k_B^2T^2}\right) - 1 \quad (3.4)$$

where h is the height of nuclei, Ω is the atomic volume, and ε is the surface free energy. J_{2D} is the nucleation rate. At the critical miscut angle, the surface supersaturation should be equal to the supersaturation of 2D-nucleation.

$$\sigma_{s,c} = \sigma_{2D} \quad (3.5)$$

Bring Eqs. (2.21), (2.22) and (3.4) into (3.5) in order to get the diffusion length λ_s.

$$\sigma\left[1 - \frac{1}{cosh\left(\frac{\mathrm{h}/\tan\theta}{2\lambda_s}\right)}\right] = exp\left(\frac{\Omega\pi h\varepsilon^2}{(65 - \ln J_{2D})k_B^2T^2}\right) - 1 \quad (3.6)$$

In this work, the atomic volume Ω is 0.264 nm^3, the height h is 0.52 nm, and the surface free energy $\varepsilon = 6.0$ $\mathrm{eV/nm}^2$ [30]. The nucleation rate J_{2D} is assumed as 10^{12} [28]. According to the AFM results, the critical miscut angle is assumed as 0.45° for series I and 0.23° for series III. Therefore, the diffusion length λ_s is 52.8 nm at 730 ℃ and 50.6 nm at 745 ℃. Put these two diffusion length at different temperature into equation (3.3), and get Q as 0.27 eV and a as 0.3 nm. Therefore, the diffusion length λ_s can be expressed as follows. Here, more experiments is necessary to confirm the accurate diffusion length.

$$\lambda_s = 3.0\ exp(0.27eV/2k_BT) \quad (3.7)$$

Figure 3.5(a) shows that Ga surface supersaturation decrease with increasing miscut angle. As the previous section, higher surface supersaturation of Ga increases the amount of metal atoms on the surface and when a critical amount is reached, N atoms have possibility to nucleate on the terrace and form 2D islands. Therefore, InGaN morphology changes from 2D islands to steps and then to step bunching by decreasing the Ga surface supersaturation. Figure 3.5(a) shows the Ga surface supersaturation of series I is larger than that of series II, series III at the same miscut angle, because Ga vapor supersaturation of series I is larger than the other series in Fig. 3.5(b). This means decreasing growth rate (from series I to II) or increasing growth temperature (from series II to III) can also reduce the surface supersaturation by decreasing the vapor supersaturation. Fig. 3.5(a) also shows that the critical supersaturation from 2D islands to steps is similar among these three series, around 1.3×10^{12} in our calculation.

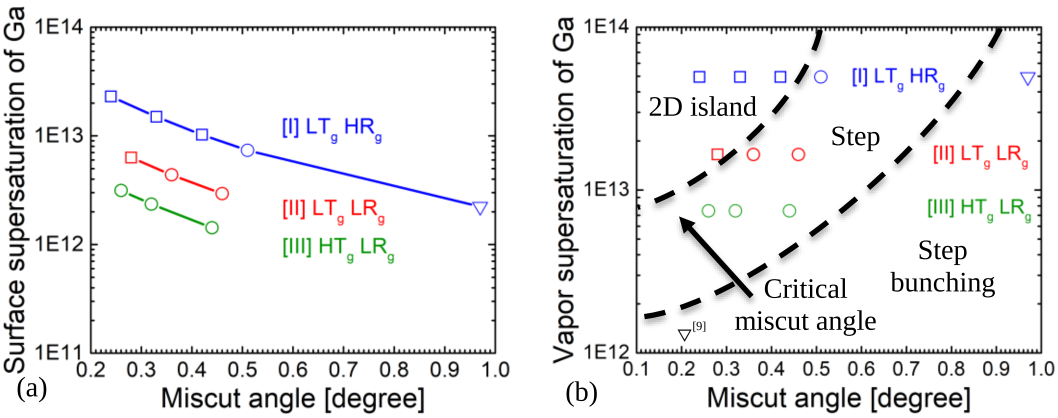

Fig. 3.5(a) Calculated Ga surface supersaturation and (b) Ga vapor supersaturation of all samples versus miscut angle (○=step, □=2D island, ▽=step bunching).

Figure 3.5(b) shows the InGaN surface morphology is controlled by combination between vapor supersaturation (i.e. growth condition) and miscut angle. It can be divided into three regions by two lines for different morphologies (2D island, step, step bunching). The critical miscut angle from 2D islands to steps increase with increasing vapor supersaturation (high growth rate or low growth temperature), therefore, the critical miscut angle shifts right from series III to I in Fig. 3.5(b). M. Kryśko et al. reported that InGaN grown at 820 °C shows step bunching even with miscut angle of 0.22° [24]. In this case, the Ga surface supersaturation should be around 10^{12}. Therefore, there should also exist another critical miscut angle line for steps to step bunching transition in Fig. 3.5(b). With low growth rate or high growth temperature (i.e. low vapor supersaturation), the critical miscut angle for steps to step bunching transition moves towards left. Usually high growth rate or low growth temperature are used to achieve high InN mole fraction. In this case, the substrate with large miscut angle can be adopted to keep InGaN morphology into step region by decreasing surface supersaturation.

3.3.2 Effect on indium incorporation

Figure 3.6 shows the InN mole fraction of InGaN layer with different miscut angle. For series I, at a growth temperature of 730 °C and a growth rate of 3.3 nm/min, InN mole fraction increases as the miscut angle from 0.2° to 0.42° and then decreases above 0.5°. For series II, when the growth rate decreases to 1.1 nm/min at 730 °C, InN mole fraction decrease to below 0.2. InN mole fraction also increases from 0.28° to 0.36°, and then decreases above 0.36°. For series III, InN mole fraction decreases to below 0.16 at 745 °C and decreases from 0.26°.

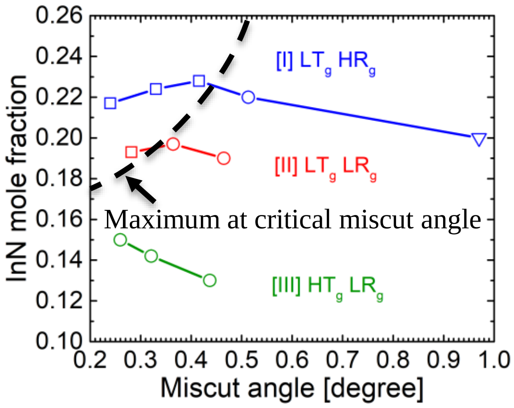

Fig. 3.6 InN mole fraction of InGaN layers with different miscut angles (○=step, □=2D island, ▽=step bunching).

Some researchers reported that InN mole fraction changed with increasing miscut angle. However, the explanations are still in debate. M. Kryśko et al. showed that InN mole fraction decrease with increasing miscut angle because the In segregation at {1-10n} facets may reduce the incorporation [24]. G. Franssen et al. interpreted that In adatoms diffuse more efficiently towards the growth step of a given terrace than Ga adatoms [31]. K. Shojiki et al. showed that for N-polar InGaN, InN mole fraction increased with step density which is proportional to the substrate miscut angle because group-III atoms are incorporated mainly at step edges [32]. H. Yamada et al. suggested that the InN mole fraction increases with miscut angle for m-plane InGaN/GaN MQWs because that the In incorporation at the step edge is larger than that on the terrace [33, 34]. However, our results show that the InN mole fraction is related to the InGaN morphology. For stepped morphology, InN mole fraction decrease with increasing miscut angle, while, for 2D islands, InN mole fraction increase a little with larger miscut angle.

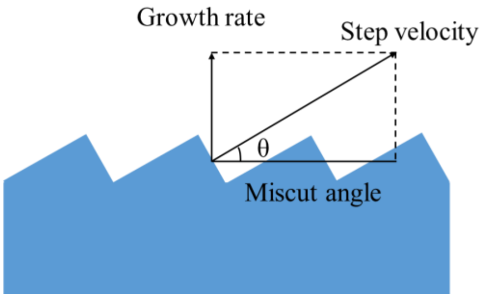

Fig. 3.7 The relationship among growth rate, step velocity and miscut angle.

According to the phase diagram of InN [35], high temperature increases the decomposition rate of InN. A. Yamamoto et al. showed that InN could not be grown at above 600 °C [36]. However, InGaN can be grown at that temperature. Our results also show that InGaN can be grown at even above 700°C. Therefore, the In incorporation during the InGaN growth is strongly dependent on Ga incorporation. A high speed of the Ga incorporation into step edge, i.e. high step velocity, can effectively reduce the InN decomposition. Figure 3.7 shows the relationship among growth rate, step velocity and miscut angle matches the following equation (3.8).

$$R_g = R_{step} \times \sin\theta \qquad (3.8)$$

Here, R_g and R_{step} are the growth rate and the step velocity, respectively. Therefore, high growth rate which means high step velocity can increase InN mole fraction [2]. The stepped morphology suggests that all the atoms can move into step edge. For the same number of atoms, more steps, means rather a slower velocity of an individual step. For series III, all the samples have stepped morphology, therefore, the InN mole fraction decreases with increasing miscut angle due to the lower step velocity.

For 2D island morphology, islands create extra steps due to island borders. Therefore, InGaN layers with a 2D island morphology has more step edges. The total step edge decreases with decreasing island density during the morphological change from 2D islands to steps with larger miscut angle. Therefore, InN mole fraction increases with increasing miscut angle by decreasing the total step edge. For series I and II, InN mole fraction first increases in the case of 2D islands. When the InGaN morphology changes to steps, the InN mole fraction decreased because the step density increases with increasing miscut angle. Therefore, the InN mole fraction reaches the maximum at around critical miscut angle. The maximum shifts left from series I to series III because the high growth temperature and low growth rate can change the morphology by decreasing the surface supersaturation in the previous section.

3.3.3 Effect on PL

To improve accuracy of PL measurement, five points on each sample were measured. Figure 3.8 shows the PL peak intensity with peak wavelength of all three series. With decreasing growth rate and increasing growth temperature, peak wavelength becomes shorter and peak intensity increase from series I to III. For series III, all samples have stepped morphology. Corresponding to the InN mole fraction in Fig. 3.6, peak wavelength blue-shifts with increasing miscut angle. At the same time, peak intensity decreases with increasing miscut angle, possibly because that more InN mole fraction increases the localization of carriers. Sample G and sample H in series II also have the similar results, while, for series I, sample A with 2D islands has longer peak wavelength and stronger peak intensity than sample D with steps despite smaller InN mole fraction. It is possible that these islands change the strain of InGaN layer which leads to large band gap tilt. This band tilt can increase peak wavelength and increase the localization to strengthen the peak intensity. It is similar to the results of sample F and G in series II. Sample E with step bunching has the shortest wavelength and the smallest peak intensity in series I.

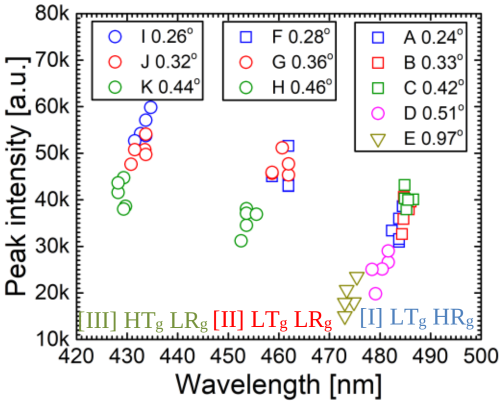

Fig. 3.8 PL peak intensity vs peak wavelength of all series (○=step, □=2D island, ▽=step bunching).

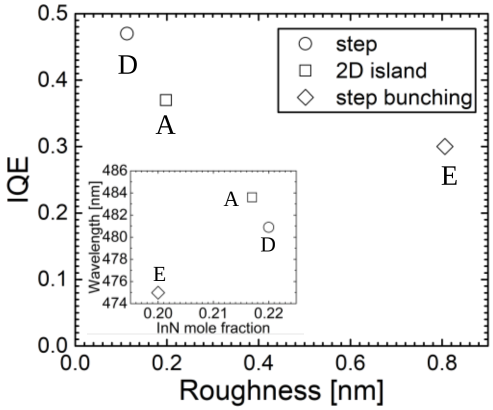

Fig. 3.9 IQE and roughness of InGaN with different morphologies (the Inset is the peak wavelength vs the InN mole fraction of every sample).

In Fig. 3.9, the stepped morphology has the smallest roughness. From steps to 2D islands the roughness increases, which is similar to the results of series I and II shown in Table 3.2. The step-bunching has the largest roughness. The IQE of the steps is higher than the 2D islands at similar peak wavelength with the same growth condition. But it decreases strongly with step-bunching since it typically leads to PL wavelength broadening due to lateral In fluctuations close to and far away from the step-edges. Thus, for high-InN-mole-fraction InGaN growth, a large enough miscut angle provides another way to decrease supersaturation on an individual terrace to maintain a flat surface and improve IQE without changing growth condition.

3.4 Comparison of InGaN on GaN substrate with GaN/sapphire template

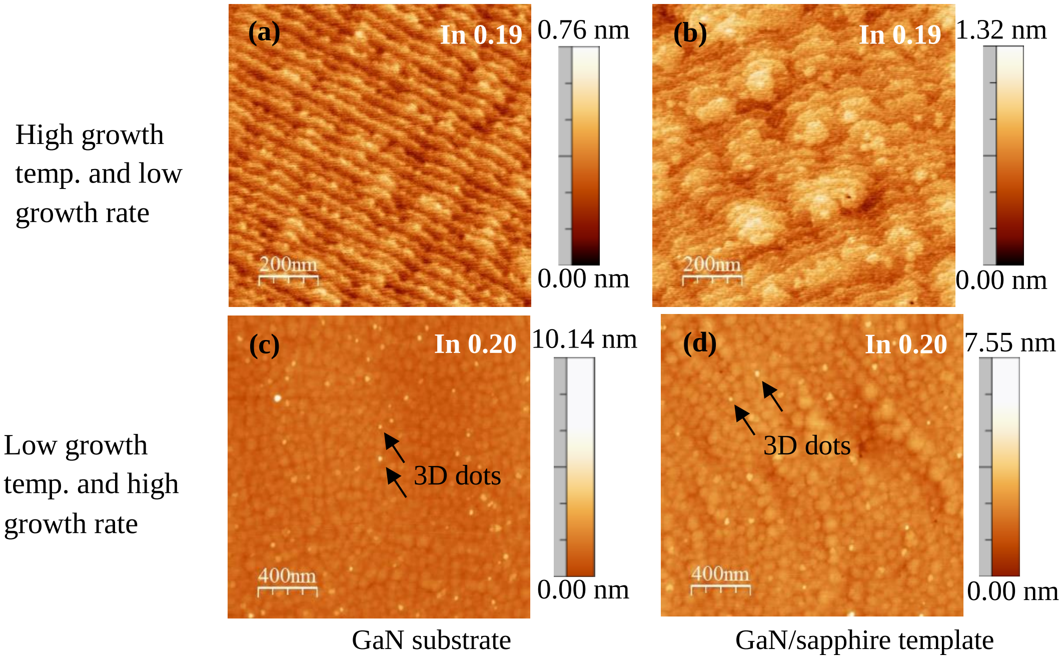

Fig. 3.10 AFM image of InGaN grown at R_g=2.76 nm/min, T=730 °C on (a) GaN substrate (sample A in section 3.2), (b) on GaN/sapphire template, and at R_g=8.12 nm/min, T=670 °C on (c) GaN substrate (sample F in section 3.2), (d) GaN/sapphire template (The vertical direction is [11-20]).

InGaN layer were also grown on GaN/sapphire template at the same time to keep the growth condition in gas phase consistent. The miscut angle of sapphire is ~0.2°. Besides the samples listed in Table 1, many additional samples with a greater variation of growth condition were used to compare the influence of GaN substrates versus GaN/sapphire template. The threading dislocation density (TDD) of the GaN/sapphire template is ~10^9 cm^{-2}, while the TDD of the GaN substrates is as low as ~10^6 cm^{-2}.

Figure 3.10 and 3.11 compare AFM images of InGaN layers grown on GaN substrate and GaN/sapphire templates. The InN mole fraction of InGaN layer on GaN substrate and GaN/sapphire template are similar in Table 3.2. Due to low supersaturation, InGaN on the GaN substrate (sample A in section 3.2) has a stepped morphology in Fig. 3.10(a). However, in Fig. 3.10(b), InGaN on GaN/sapphire template has 2D islands with the same growth condition. Figure 3.11 also shows that with high temperature and low growth rate, InGaN on GaN substrate has stepped morphology, while InGaN on GaN/sapphire template is populated with 2D islands. The GaN/sapphire template (no patterned sapphire) has high threading dislocation density of 10^8-10^{10} cm^{-2} [37]. These TDs with a screw component easily lead to spiral growth [10], and can pin step edges, which may reduce the diffusion length. Moreover, sapphire substrate has a miscut angle of 0.2°±0.1°. This small miscut angle increases the surface supersaturation and thus increases the probability for adatoms on the terrace to form 2D island. GaN substrate grown by HVPE has low threading dislocation density as low as ~10^6 cm^{-2} [17], and the miscut angle tends to be larger than 0.2°. Therefore, it is easier for InGaN on GaN substrate to achieve stepped morphology than that on GaN/sapphire template in Fig. 3.12. With low temperature and high growth rate, 3D dots form on both substrates in Fig. 3.12. However, Fig. 3.10(d) shows the size of dots on GaN/sapphire template is in the range of 35-65 nm which is larger than sample F. The dot density is 7.5×10^8 cm^{-2} and the height is 1-3nm which are lower than sample F. Both InN mole fraction and thickness are the same, but there is a difference in the residual strain from the substrate, which is likely to delay the formation of 3D dot on the GaN/sapphire templates.

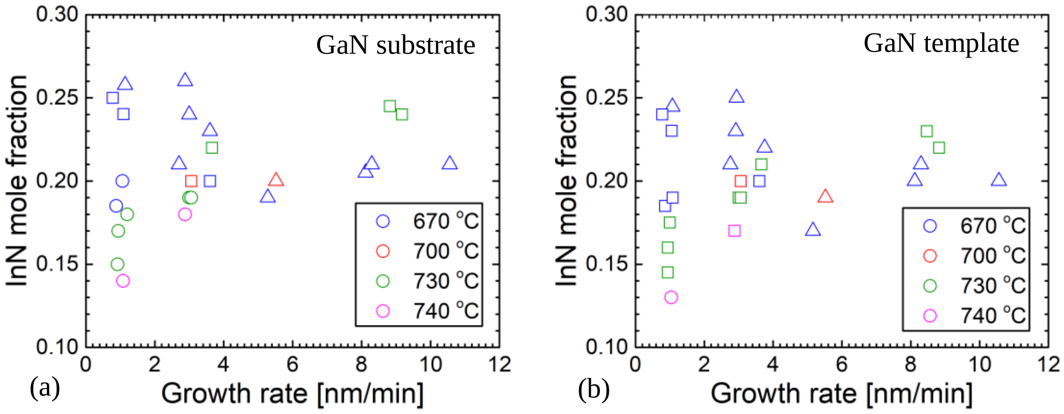

Fig. 3.11 Morphology of InGaN layer grown on (a) GaN substrate and (b) GaN/sapphire template (○=step, □=2D island, △=3D dot)

3.5 Summary

The InGaN layers grown by MOVPE show essentially for different morphologies: steps, 2D islands, 3D dots, and step bunching. With increasing vapor supersaturation (e.g. low growth temperature, high growth rate), the InGaN morphology changes from steps to 2D islands and then to 3D dots. The dependency of InGaN morphology on miscut angle of GaN substrate was interpreted by surface supersaturation. The InGaN morphology is controlled by combination between vapor supersaturation (i.e. growth condition) and miscut angle. The critical miscut angle from 2D island to step becomes large with increasing vapor supersaturation (i.e. higher growth rate or lower growth temperature). Moreover, critical miscut angle is important to obtain higher InN mole fraction and stronger PL intensity with stepped morphology which means high quality. Too large miscut angles (above 0.9°) will form step bunching, a fourth morphology. To compare with InGaN on GaN/sapphire template, InGaN on GaN substrate can achieve steps easily because of lower surface supersaturation. This method is expected to improve the quality of InGaN layer with high InN mole fraction.

References

1. Y. Narukawa, M. Ichikawa, D. Sanga, M. Sano and T. Mukai, “White light emitting diodes with super-high luminous efficacy”, J. Phys. D: Appl. Phys. 43 (2010) 354002
2. R. Hashimoto, J. Hwang, S. Saito, and S. Nunoue, “High-efficiency green-yellow light-emitting diodes grown on sapphire (0001) substrates”, Phys. Status Solidi C 10 (2013) 1529-1532
3. H. K. Cho, J. Y. Lee, C. S. Kim, G. M. Yang, N. Sharma, C. Humphreys, “Microstructural characterization of InGaN/GaN multiple quantum wells with high indium composition”, J. Cryst. Growth 231 (2001) 466–473
4. F. C.-P. Massabuau, S.-L. Sahonta, L. Trinh-Xuan, S. Rhode, T. J. Puchtler, M. J. Kappers, C. J. Humphreys, and R. A. Oliver, “Morphological, structural, and emission characterization of trench defects in InGaN/GaN quantum well structures”, Appl. Phys. Lett. 101 (2012) 212107
5. M. Pristovsek, A. Bao, R. A. Oliver, T. Badcock, M. Ali, and A. Shields, “Effects of wavelength and defect density on the efficiency of (In, Ga) N-based light-emitting diodes”, Phys. Rev. Applied 7 (2017) 064007
6. S. Suihkonen, T. Lang, O. Svensk, J. Sormunen, P. T. Törmä, M. Sopanen, H. Lipsanen, M. A. Odnoblyudov, V.E. Bougrov, “Control of the morphology of InGaN/GaN quantum wells grown by metalorganic chemical vapor deposition”, J. Cryst. Growth 300 (2007) 324–329
7. F. Massabuau, M. Kappers, C. Humphreys, and R. Oliver, “Mechanisms preventing trench defect formation in InGaN/GaN quantum well structures using hydrogen during GaN barrier growth”, Phys. Status Solidi B 254 (2017) 1600666
8. J.-I. Hwang, R. Hashimoto, S. Saito, and S. Nunoue, “Development of InGaN-based red LED grown on (0001) polar surface”, Appl. Phys. Express 7 (2014) 071003

9. R. A. Oliver, M. J. Kappers, and C. J. Humphreys, “Growth modes in heteroepitaxy of InGaN on GaN”, J. Appl. Phys. 97 (2005) 013707
10. S. Keller, U. K. Mishra, S. P. Denbaars and W. Seifert, “Spiral growth of InGaN nanoscale islands on GaN”, Jpn. J. Appl. Phys. 37 (1998) L431–L434
11. M. Pristovsek, A. Kadir, C. Meissner, T. Schwaner, M. Leyer, and M. Kneissl, “Surface transition induced island formation on thin strained InGaN layers on GaN (0001) in metal-organic vapour phase epitaxy”, J. Appl. Phys. 110 (2011) 073527
12. H. J. Kim, H. Na, S.-Y. Kwon, H.-C. Seo, H. J. Kim, Y. Shin, K.-H. Lee, D. H. Kim, H. J. Oh, S. Yoon, C. Sone, Y. Park, and E. Yoon, “Growth of In-rich InGaN/GaN quantum dots by metalorganic chemical vapor deposition”, J. Cryst. Growth 269 (2004) 95–99
13. M. J. Galtrey, R. A. Oliver, M. J. Kappers, C. J. Humphreys, P. H. Clifton, D. Larson, D. W. Saxey, and A. Cerezo, “Three-dimensional atom probe analysis of green- and blue-emitting $In_xGa_{1-x}N/GaN$ multiple quantum well structures”, J. Appl. Phys. 104 (2008) 013524
14. C. Bayram, and M. Razeghi, “Stranski–Krastanov growth of InGaN quantum dots emitting in green spectra”, Appl. Phys. A 96 (2009) 403–408
15. G. X. Ju, M. Tabuchi, Y. Takeda, and H. Amano, “Role of threading dislocations in strain relaxation during GaInN growth monitored by real-time X-ray reflectivity”, Appl. Phys. Lett. 110 (2017) 262105
16. A. Kadir, C. Meissner, T. Schwaner, M. Pristovsek, M. Kneissl, “Growth mechanism of InGaN quantum dots during metalorganic vapor phase epitaxy”, J. Cryst. Growth 334 (2011) 40–45
17. H. M. Foronda, A. E. Romanov, E. C. Young, C. A. Robertson, G. E. Beltz, and J. S. Speck, “Curvature and bow of bulk GaN substrates”, J. Appl. Phys. 120 (2016) 035104
18. M. Pristovsek, A. Kadir, C. Meissner, T. Schwaner, M. Leyer, J. Stellmach, M. Kneissl, F. Ivaldi, and S. Kret, “Growth mode transition and relaxation of thin InGaN layers on GaN (0001)”, J. Cryst. Growth 372 (2013) 65–72

19. F. Jiang, R.-V. Wang, A. Munkholm, S. K. Streiffer, G. B. Stephenson, P. H. Fuoss, K. Latifi, and C. Thompson, “Indium adsorption on GaN under metal-organic chemical vapor deposition conditions”, Appl. Phys. Lett. 89 (2006) 161915
20. M. Pristovsek, A. Kadir, and M. Kneissl, “Surface transitions during InGaN growth on GaN (0001) in metal–organic vapor phase epitaxy”, Jpn. J. Appl. Phys. 52 (2013) 08JB23
21. T. Zywietz, J. Neugebauer, and M. Scheffler, “Adatom diffusion at GaN (0001) and (0001) surfaces”, Appl. Phys. Lett. 73 (1998) 487-489
22. B. G. Orr, D. Kessler, C. W. Snyder and L. Sand, “A model for strain-induced roughening and coherent island growth”, Europhys. Lett. 19 (1992) 33-38
23. M. Leszczynski, R. Czernecki, S. Krukowski, M. Krysko, G. Targowski, P. Prystawko, J. Plesiewicz, P. Perlin, T. Suski, “Indium incorporation into InGaN and InAlN layers grown by metalorganic vapor phase epitaxy”, J. Cryst. Growth 318 (2011) 496–499
24. M. Kryśko, G. Franssen, T. Suski, M. Albrecht, B. Łucznik, I. Grzegory, S. Krukowski, R. Czernecki, S. Grzanka, I. Makarowa, M. Leszczyński, and P. Perlin, “Correlation between luminescence and compositional striations in InGaN layers grown on miscut GaN substrates”, Appl. Phys. Lett. 91 (2007) 211904
25. A. Nakamura, N. Yanagita, T. Murata, K. Hoshino, and K. Tadatomo, “Effects of sapphire substrate misorientation on the GaN-based light emitting diode grown by metalorganic vapour phase epitaxy”, phys. stat. sol. (c) 5 (2008) 2007–2009
26. P. Perlin, G. Franssen, J. Szeszko, R. Czernecki, G. Targowski1, M. Kryśko, S. Grzanka, G. Nowak, E. Litwin-Staszewska, R. Piotrzkowski, M. Leszczyński, B. Łucznik, I. Grzegory, R. Jakieła, M. Albrecht, and T. Suski, “Nitride-based quantum structures and devices on modified GaN substrates”, Phys. Status Solidi A 206 (2009) 1130–1134
27. W. K. Burton, N. Cabrera and F. C. Frank, “The growth of crystals and the equilibrium structure of their surfaces”, Philos. Trans. R. Soc. Ser. A 243 (1951) 299-358

28. T. Shitara and Ta. Nishinaga, “Surface Diffusion Length of Gallium during MBE Growth on the Various Misoriented GaAs(001) Substrates”, Jpn. J. Appl. Phys. 28 (1989) 1212-1216
29. J.P. Hirth and G.M. Pound: CONDENSATION AND EVAPORATION, Nucleation and Growth Kinetics (Pergamon Press, Oxford, London, Paris, Frankfurt, 1963)
30. John E. Northrup, J. Neugebauer, R. M. Feenstra, and A. R. Smith, “Structure of GaN(0001): The laterally contracted Ga bilayer model”, Phys. Rev. B 61 (2000) 9932-9935
31. G. Franssen, T. Suski, M. Kryśko, B. Łucznik, I. Grzegory, S. Krukowski, A. Khachapuridze, R. Czernecki, S. Grzanka, P. Mensz, M. Leszczyński, S. Porowski, and M. Albrecht, “Influence of substrate misorientation on properties of InGaN layers grown on freestanding GaN”, Phys. Stat. Sol. (c) 5 (2008) 1485–1487
32. K. Shojiki, J.-H. Choi, H. Shindo, T. Kimura, T. Tanikawa, T. Hanada, R. Katayama, and T. Matsuoka, “Effect of c-plane sapphire substrate miscut angle on indium content of MOVPE-grown N-polar InGaN”, Jpn. J. Appl. Phys. 53 (2014) 05FL07
33. H. Yamada, K. Iso, M. Saito, K. Fujito, S. P. Denbaars, J. S. Speck, and S. Nakamura, “High brightness blue InGaN/GaN light emitting diode on nonpolar m-plane bulk GaN substrate”, Jpn. J. Appl. Phys. 46 (2007) L960–L962
34. H. Yamada, K. Iso, M. Saito, K. Fujito, S. P. Denbaars, J. S. Speck, and S. Nakamura, “Effects of off-axis GaN substrates on optical properties of m-plane InGaN/GaN light-emitting diodes”, J. Cryst. Growth 310 (2008) 4968–4971
35. T. Matsuoka, “Progress in nitride semiconductors from GaN to InN—MOVPE growth and characteristics”, Superlattices and Microstructures 37 (2005) 19–32
36. A. Yamamoto, K. Kodama, T. Matsuoka, and M. Kuzuhara, “Low-temperature (≤ 600° C) growth of high-quality $In_xGa_{1-x}N$ (x∼ 0.3) by metalorganic vapor phase epitaxy using NH_3 decomposition catalyst”, Jpn. J. Appl. Phys. 56 (2017) 041001
37. J. L. Weyher, H. Ashraf, and P. R. Hageman, “Reduction of dislocation density in epitaxial GaN layers by overgrowth of defect-related etch pits”, Appl. Phys. Lett. 95 (2009) 031913

Chapter 4 Multi-quantum well growth

4.1 Introduction

4.2 High InN-mole-fraction MQW growth

4.3 Effect of miscut angle

4.4 Summary

References

4.1 Introduction

Only single InGaN layer is not enough to capture much carriers for strong emission. In 1993, S. Nakamura et al. firstly achieved Double-Heterostructure Blue-LEDs with p-GaN-n-InGaN (20 nm)-n-GaN based on this technology with GaN buffer and p-type technology [1, 2]. Then, they grew InGaN multi-quantum-well structure (MQW) consisting of 3 nm wells and 3 nm barriers to decrease the misfit dislocation in the thick InGaN layer caused by the stress because of lattice mismatch and improve the crystal quality of InGaN layer [3]. Nowadays, InGaN based MQW structure is applied widely in fabrication of GaN-based LED. For violet-blue emission, high internal quantum efficiency (IQE) has been achieved [4]. For long wavelength emission, however, the quantum efficiency is suddenly decreased [5]. F. A. Ponce et al. showed that there were misfit dislocations for green MQW [6]. A. Kaneta et al. observed that there are some pits on the wing of ELOG for green MQW by AFM and SNOM which means new TDs were generated during MQW growth to decrease PL intensity after 470 nm [7]. H. K. Cho et al. also observed the new V-pits appear for green MQW on low TD density GaN compared to low InN-mole fraction MQW [8]. However, the formation mechanism of this defects is unclear.

Besides InGaN layer growth, barrier growth condition is also influential for MQW growth. Many procedures have been used to improve the optical properties of high-InN-mole-fraction multiple quantum wells (MQWs) by optimizing barrier growth, such as the use of a high temperature or H_2 flow during barrier growth to etch excess In and prevent defects [9, 10], the insertion of AlGaN interlayer for stress compensation and surface flattening [11].

In this chapter, based on InGaN growth illustrated in the last chapter, we grow multi-quantum well (MQW) structure by MOVPE. We compare high InN-mole-fraction MQWs with low InN-mole-fraction MQWs and we also grow MQWs on GaN/sapphire template at the same time in order to analyze the effect of substrate. Then, we investigate the effect of micut angle on MQW growth. We illustrate that a smooth InGaN layer itself is a key point for InGaN-based MQW growth.

4.2 High InN-mole-fraction MQW growth

In this work, two series MQWs with different InN-mole-fractions were grown on GaN substrate and GaN/sapphire by MOVPE at the same time. In each series, single InGaN well layer, 1QW, 3QW or 5QW were grown to observe the defect formation. Triethylgallium (TEG), trimethylindium (TMI) and ammonia (NH_3) were used as the gallium, indium and nitrogen sources, respectively. Trimethylgallium (TMGa) was also used to grow InGaN at high growth rate. During MQW growth, nitrogen was used as the carrier gas, and the pressure in the reactor was kept at 750 hPa. The growth parameters of InGaN well layer is summarized in Table 4.1. Both series have the same barrier growth parameters. The barrier growth (5 min) involved three parts: growth at the well temperature as a protection layer (1 min), growth during the temperature ramp (1 min), and growth at the barrier temperature (3 min). According to in-situ monitoring, the temperature was stable after the temperature ramp. Both barrier temperatures are 745 ℃. TEG and NH_3 was supplied during the whole barrier growth. The TEG and NH_3 flow rate was kept at 6.4 μmol/min and 0.33 mol/min, respectively, for all three series.

Table 4.1 Growth parameters of InGaN well layer

Series	Sample	Miscut angle (°)	Growth temp. (℃)	TEG (μmol/min)	TMI (μmol/min)	NH3 (mol/min)	Growth time (s)
I Low InN-mole-fraction	InGaN SQW 3QW 5QW	0.57 0.22 0.36 0.32	715	6.4	10.2	0.34	150
II High InN-mole-fraction	InGaN SQW 3QW	0.33 0.31 0.29	715	21.0(TMG)	33.6	0.34	34

The well and barrier layer thickness were obtained as around 2.5 nm/5 nm and InN mole fraction were 0.28 and 0.33 for the two series by comparing X-ray diffraction (XRD) (0002) ω-2θ measurements and kinematic diffraction simulation. Non-contact tapping mode atomic force microscope (AFM) were used to measure the surface morphology. The room temperature (RT) photoluminescence (PL) was excited by a 325nm He-Cd laser under an excitation power density of 160 kW/cm^2.

Table 4.2 PL results of all samples

Series	Sample	On GaN substrate			On GaN/sapphire template		
		Peak wavelength (nm)	Peak intensity (a.u.)	Integrated intensity (a.u.)	Peak wavelength (nm)	Peak intensity (a.u.)	Integrated intensity (a.u.)
I Low InN-mole-fraction	InGaN	479.9	393	27346	478.1	266	3487
	SQW	0	0	0	0	0	0
	3QW	501.6	1895	178510	486.6	1149	92378
	5QW	492.7	36041	3165488	492.7	10263	821923
II High InN-mole-fraction	InGaN	521.1	3803	454742	520.4	1668	163977
	SQW	0	0	0	0	0	0
	3QW	548.8	601	108949	539.7	339	40341

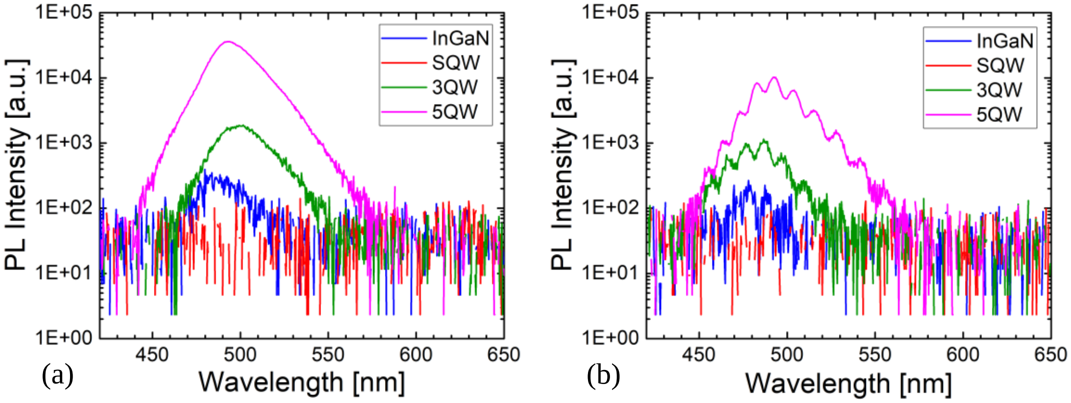

Fig. 4.1 PL spectrum of series I (In 0.28) (a) on GaN substrate; (b) on GaN/sapphire template (Integral time=100 ms).

Figure 4.1 shows the spectrum of series I with low InN-mole-fraction. For single InGaN layer, the both peak wavelength are ~480 nm. For QW structure, peak wavelength shifts to red around 10 nm because the barrier brings the QCSE. SQW do not have PL intensity possibly because of thin well layer. However, for 3QW and 5QW, PL intensity increase with increasing period number. Moreover, PL intensity of QW on GaN substrate increases more than that on

GaN/sapphire template. For high InN-mole-fraction, the PL intensity of single InGaN layer increases possibly because the large band offset for high InN-mole-fraction can capture more carriers. While, PL intensity of MQWs decreases clearly compared to low InN-mole-fraction MQW with the same period. Due to the same growth condition of barrier layer, this decreased PL intensity is mainly because of the growth condition of InGaN well layer. Moreover, for high InN-mole-fraction, PL intensity of 3QW is smaller than single InGaN layer.

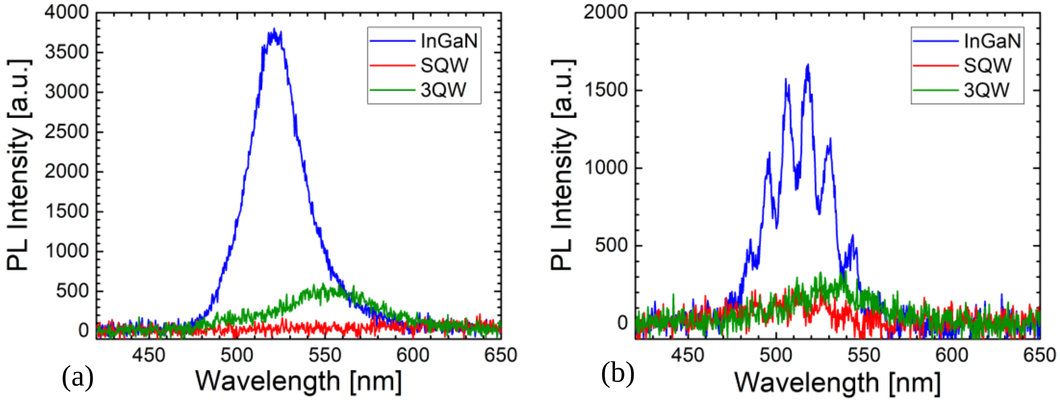

Fig. 4.2 PL spectrum of series II (In 0.32) (a) on GaN substrate; (b) on GaN/sapphire template (Integral time=1000 ms).

The PL intensity can be understood from the topography of the samples. Figure 4.3 shows the AFM image of series I. Single InGaN layer on GaN substrate has stepped morphology. Based on this stepped InGaN well layer, the MQW growth can easily achieve stepped morphology. For InGaN on GaN/sapphire template, the step is not straight because of screw or mixed dislocation. There are many pits and the step is not straight when we grow MQW based on this InGaN layer. The size of pits increases with increasing periods but the density does not change. Figure 4.3(h) shows there exists trench defects on 5QW/ GaN template, while there is no any trench defect on SQW and 3QW. F. C.-P. Massabuau et al. observed that the trench defect is related with the stacking faults under the trench defect rather than connect with the dislocation from the

GaN/sapphire template [11]. However, no trench defect is observed on the surface of 5QW/GaN substrate. Therefore, the stacking faults is possibly because the tortuous step leads to non-uniform strain distribution in plane. The accumulated large strain in some area will relax first and form new dislocation.

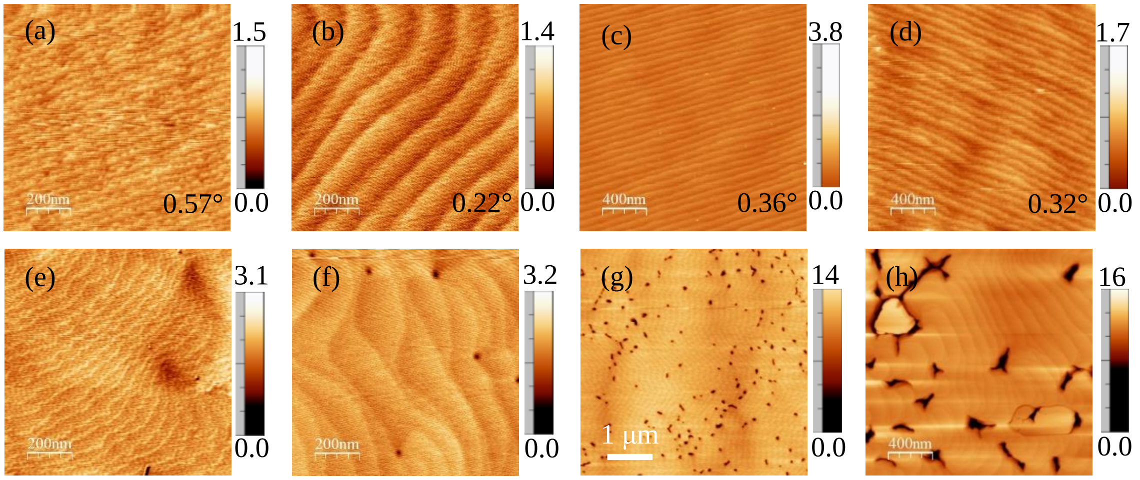

Fig. 4.3 AFM images of series I with 0.28 InN-mole-fraction (Unit: nm). Top row is on GaN substrate, (a) InGaN layer, (b) SQW, (c) 3QW, (d) 5QW; bottom row is on GaN/sapphire template, (e) InGaN layer, (f) SQW, (g) 3QW, (h) 5QW (The vertical direction is [11-20]).

Figure 4.4 shows the AFM images of series II with 0.33 InN mole fraction. Due to high growth rate of InGaN layers which increase the vapor supersaturation, a part of 2D islands appear on the surface of single InGaN/GaN substrate in Fig. 4.4(a). While the surface of single InGaN on GaN/sapphire template involve the whole 2D island structure which are not related with threading dislocation from GaN/sapphire template (Fig. 4.4(d)). Based on these InGaN layers, many pits and trench defects form on even SQW (Fig. 4.4(b) and (e)). In clusters also appear on both 3QW (Fig. 4.4(c) and (f)). Some In clusters are relaxed. Compared to 3QW on GaN/sapphire template, 3QW on GaN substrate has lower defect density and smaller size of In cluster. Therefore, tortuous step or 2D island will leads to non-uniform strain distribution which will bring new defects if they are relaxed. GaN substrate has larger miscut angle which reduce surface supersaturation to decrease the 2D island density, therefore, MQW on GaN substrate will have smoother surface.

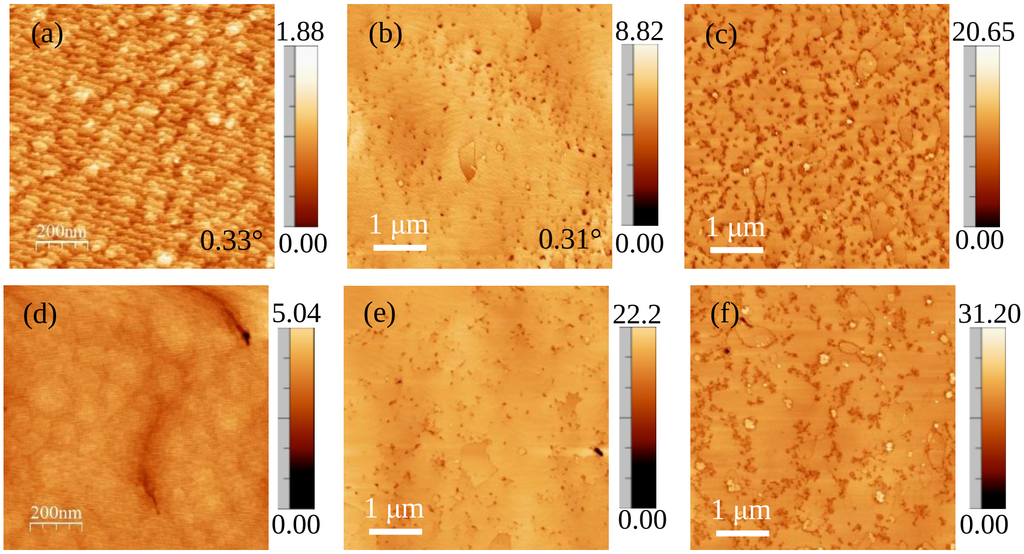

Fig. 4.4 AFM image of series II with 0.33 InN-mole-fraction (Unit: nm). Top row is on GaN substrate, (a) InGaN layer, (b) SQW, (c) 3QW; bottom row is on GaN/sapphire template, (d) InGaN layer, (e) SQW, (f) 3QW (The vertical direction is [11-20]).

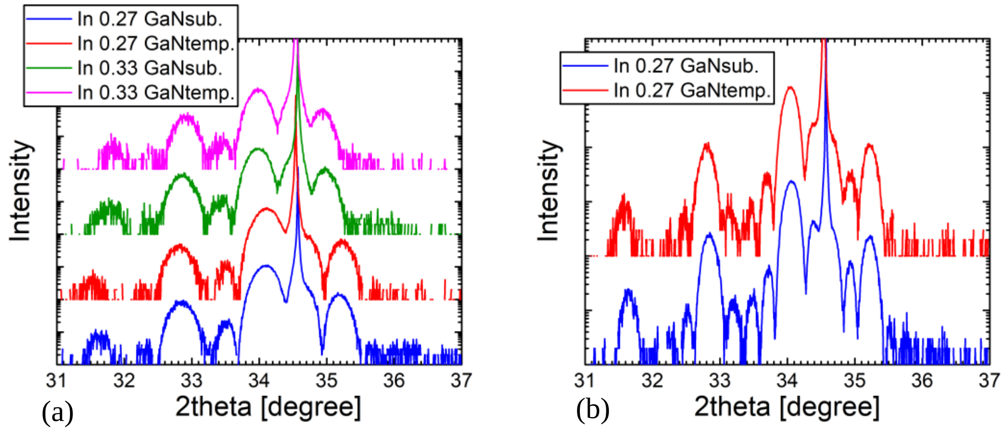

Fig. 4.5 XRD curve of (a) 3QW and (b) 5QW

The interface can be understood from the XRD curves. Figure 4.5 shows the XRD curve of 3QW and 5QW. Comparing 3QW of two series in Fig. 4.5(a), the satellite peak of low InN-mole-fraction is stronger than the high InN-mole-fraction, which corresponds to the rough interface with defects. Figure 4.5(b) shows that satellite peak of 5QW on GaN substrate is stronger than that on GaN/sapphire template because of pits and trench defects which are observed by AFM.

4.3 Effect of miscut angle

Table 4.3 the growth parameters of InGaN well layer

Series	Sample	Miscut angle (°)	Growth temp. (°C)	TEG (μmol/min)	TMI (μmol/min)	NH_3 (mol/min)	Growth time (s)
I	A	0.55	725	12.7	20.4	0.34	75
	B	0.24					
	C	Temp.					
II	D	0.44	718	12.7	20.4	0.34	75
	E	0.28					
	F	Temp.					
III	G	0.44	710	12.7	20.4	0.34	75
	H	0.27					
	I	Temp.					

In this work, three-period MQWs were grown on GaN substrate with different miscut angles. The growth temperature of InGaN well layer was changed for different wavelength. Triethylgallium (TEG), trimethylindium (TMI) and ammonia (NH_3) were used as the gallium, indium and nitrogen sources, respectively. Trimethylgallium (TMGa) was also used to grow InGaN at high growth rate. During the MQW growth, nitrogen was used as the carrier gas, and the pressure in the reactor was kept at 750 hPa. The growth parameters of InGaN well layer is summarized in Table 4.3. The barrier growth (5 min) involved three parts: growth at the well temperature as a protection layer (1 min), growth during the temperature ramp (1 min), and growth at the barrier temperature (3 min). According to in-situ monitoring, the temperature was stable after the temperature ramp. Barrier temperature is 40 °C higher than well temperature. TEG and NH_3 was supplied during the whole barrier growth. The TEG and NH_3 flow rate was kept at 6.4 μmol/min and 0.33 mol/min. MQW were also grown on GaN/sapphire template at the same time. Besides these samples listed in Table 4.3, many additional samples with a greater variation of growth condition were used to compare the influence of GaN substrates versus GaN/sapphire template. Well and barrier layer thickness and InN mole fraction are obtained by comparing X-ray diffraction (XRD) (0002) ω-2θ measurements and kinematic diffraction simulation. Non-contact tapping mode atomic force microscope (AFM) were used to measure the surface morphology. The room temperature (RT) photoluminescence (PL) was excited by a 325nm He-Cd laser under an excitation power density of 160 kW/cm^2. Table 4.4 shows the thickness, InN mole fraction, and PL data of all samples in Table 4.3.

Table 4.4 Thickness, InN mole fraction, peak wavelength and PL integrated intensity

Series	Sample	Miscut angle (°)	InN mole fraction	Well thickness (nm)	Barrier thickness (nm)	Peak wavelength (nm)	PL integrated intensity
I	A	0.55	0.27	2.62	5.24	486.285	178664
	B	0.24	0.27	2.55	5.1	493.773	769505
	C	Temp.	0.26	2.7	5.4	503.727	1883452
II	D	0.44	0.28	2.58	5.16	518.946	290783
	E	0.28	0.28	2.62	5.24	510.816	621580
	F	Temp.	0.27	2.62	5.24	513.293	504399
III	G	0.44	0.32	2.7	5.4	551.925	93977
	H	0.27	0.32	2.7	5.3	547.737	81548
	I	Temp.	0.31	2.75	5.5	539.342	23749

Figure 4.5 shows AFM images of all samples. For MQW on GaN substrate, there are many pits on the surface. These pits are not related with threading dislocation from substrate because of low dislocation density of GaN substrate. It is also found that small miscut angle of GaN substrate decreases pit density. According to the previous research of InGaN layer growth, large miscut angles change morphology from 2D islands to steps by decreasing surface supersaturation while, in this case, large miscut angle increases pit density. One possible reason is that these new pits are due to the barrier growth condition. Compared with the barrier growth condition in the previous section, high growth temperature decrease vapor supersaturation of Ga during barrier growth. It is possible that low supersaturation by large miscut angle make barrier growth in the step bunching

region. If InGaN grown on the step bunching surface, the surface of InGaN is rough according to the previous results in Chapter 3. Therefore, barrier growth condition is also controlled in the step region for MQW growth. Moreover, the optimization of barrier growth condition is different between GaN substrate and GaN/sapphire template because of different miscut angle and dislocation density.

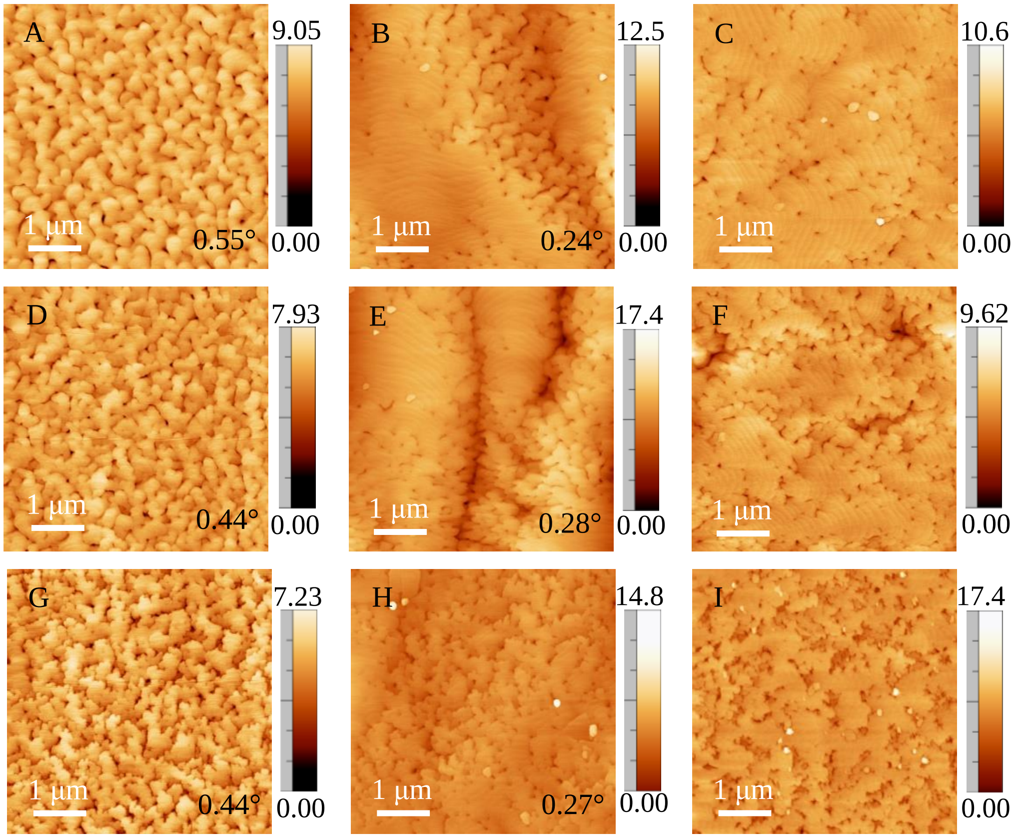

Fig. 4.5 AFM images of all samples (Unit: nm). From left to right: large miscut angle, small miscut angle, and GaN/sapphire template. From top row to bottom row: series I, series II, and series III (The vertical direction is [11-20]).

Figure 4.6 shows the PL integrated intensity vs different wavelength. PL intensity first increase before 500 nm possibly because the large band offset with more InN mole fraction can capture more carriers. In this case, MQWs grown on GaN substrate with large miscut angle have weaker intensity than small miscut angle because of high pits density which corresponds to AFM image. In comparison to PL intensity of MQWs grown on GaN/sapphire template, GaN substrate has no obvious advantage for short wavelength device. However, the PL intensity of MQWs on GaN/sapphire template decreases quickly above 520 nm because the high threading dislocation density and small miscut angle cause to the rough surface of InGaN layer in previous section results, while, the PL intensity of MQWs on GaN substrate decreases more slowly. And MQWs grown on higher miscut GaN substrate have stronger PL intensity. This is because large miscut angle smoothen InGaN surface by decreasing surface supersaturation. Therefore, for long wavelength MQW, GaN substrate can improve optical property because of large miscut angle and low dislocation density.

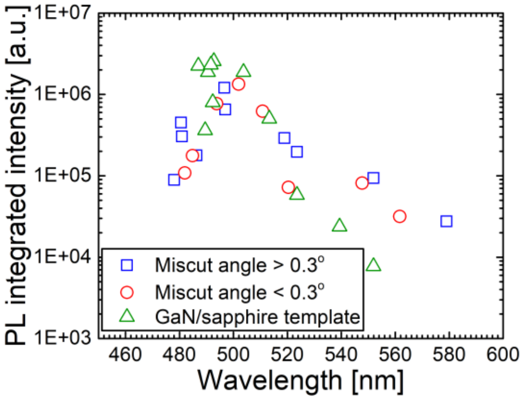

Fig. 4.6 PL integrated intensity of all samples vs peak wavelength (Integral time=1000 ms).

4.5. Summary

In this chapter, InGaN/GaN MQW growth was study on both GaN substrate and GaN/sapphire template for different wavelength. For short wavelength with low InN-mole-fraction, InGaN layer have stepped morphology, and MQWs growth with this InGaN layer will easily achieve stepped morphology and higher PL intensity. However, for high InN mole fraction, InGaN morphology change to 2D islands, and MQW surface becomes rough with many defects because the non-uniform strain distribution in plane easily causes partly relaxation. Therefore, the PL intensity decreases drastically.

There are different effects of miscut angle on MQW growth for various wavelength. For short wavelength, small miscut angle has better PL intensity than large miscut angle because of low pits density. It is possible because that large miscut angle makes barrier grow in the step-bunching region by decreasing surface supersaturation. Moreover, MQWs on GaN substrate and on GaN/sapphire template show similar PL intensity. However, for long-wavelength, MQWs on GaN substrate has stronger PL intensity than on GaN/sapphire template. Moreover, large miscut angle increases the PL intensity. This is because large miscut angle of GaN substrate can smoothen InGaN surface by decreasing surface supersaturation besides the low dislocation density. GaN substrate with large miscut angle is expected for improving optical properties of long-wavelength MQW.

References

1. S. Nakamura, “GaN Growth Using GaN Buffer Layer”, Jpn. J. Appl. Phys. 30 (1991) L1705.
2. S. Nakamura, M. Senoh, T. Mukai, “P-GaN/N-InGaN/N-GaN Double-Heterostructure Blue-Light-Emitting Diodes”, Jpn. J. Appl. Phys. 32 (1993) L8-L11.
3. S. Nakamura, T. Mukai, M. Senoh, S. Nagahama, and N. Iwasa, “$In_xGa_{(1-x)}N/In_yGa_{(1-y)}N$ superlattices grown on GaN films”, J. Appl. Phys., 74 (1993) 3911-3915
4. Y. Narukawa, M. Ichikawa, D. Sanga, M. Sano and T. Mukai, “White light emitting diodes with super-high luminous efficacy”, J. Phys. D: Appl. Phys. 43 (2010) 354002
5. B. Damilano and B. Gil, “Yellow–red emission from (Ga,In)N heterostructures”, J. Phys. D: Appl. Phys. 48 (2015) 403001
6. F. A. Ponce, S. Srinivasan, A. Bell, L. Geng, R. Liu, M. Stevens, J. Cai, H. Omiya, H. Marui, and S. Tanaka, “Microstructure and electronic properties of InGaN alloys”, Phys. Stat. Sol. (b) 240 (2003) 273–284
7. A. Kaneta, M. Funato, and Y. Kawaka, “Nanoscopic recombination processes in InGaN/GaN quantum wells emitting violet, blue, and green spectra”, Phys. Rev. B 78 (2008) 125317
8. H. K. Cho, J. Y. Lee, C. S. Kim, G. M. Yang, N. Sharma, and C. Humphreys, “Microstructural characterization of InGaN/GaN multiple quantum wells with high indium composition”, J. Cryst. Growth 231 (2001) 466–473
9. S. Suihkonen, T. Lang, O. Svensk, J. Sormunen, P.T. Törmä, M. Sopanen, H. Lipsanen, M.A. Odnoblyudov, V.E. Bougrov, “Control of the morphology of InGaN/GaN quantum wells grown by metalorganic chemical vapor deposition”, J. Cryst. Growth 300 (2007) 324–329
10. F. Massabuau, M. Kappers, C. Humphreys, and R. Oliver, “Mechanisms preventing trench defect formation in InGaN/GaN quantum well structures using hydrogen during GaN barrier growth”, Phys. Status Solidi B 254 (2017) 1600666

11. J.-I. Hwang, R. Hashimoto, S. Saito, and S. Nunoue, “Development of InGaN-based red LED grown on (0001) polar surface”, Appl. Phys. Express 7 (2014) 071003
12. F. C.-P. Massabuau, S.-L. Sahonta, L. Trinh-Xuan, S. Rhode, T. J. Puchtler, M. J. Kappers, C. J. Humphreys, and R. A. Oliver, “Morphological, structural, and emission characterization of trench defects in InGaN/GaN quantum well structures”, Appl. Phys. Lett. 101 (2012) 212107

Chapter 5 Effect of gas phase temperature on MQW growth

5.1 Introduction

InGaN-based multiple quantum wells (MQWs) have achieved high quantum efficiency for short-wavelength emission because of the high growth temperature for low-indium-content InGaN. However, for long-wavelength emission, a low growth temperature or high growth rate for high-indium-content InGaN [1] will decrease the effective V/III ratio, leading to many types of defect such as point defects [2], or a rough surface [3], which results in low quantum efficiency [4]. There is also clear evidence that the growth temperature can enhance the PL efficiency at the same InN mole fraction by increasing the effective V/III ratio[5], because the NH_3 decomposition strongly depends on the temperature [6]. Due to high In surface desorption at higher surface temperatures, this motivated us to search for other way to increase the effective V/III ratio. However, increasing the NH_3 flow rate will have little impact, since already 25% of the gas phase is NH_3 and NH_3 decomposition is very low below 900 °C [7]. Therefore, the NH_3 decomposition rate should be considered. One such attempt in literature used a separate heated NH_3 inlet [6]. In this chapter, since the author did not want to alter our reactor, a practical method of increasing the gas phase temperature to increase the actual V/III ratio on the wafer surface in a horizontal MOVPE reactor is demonstrated here to improve optical properties of high-indium-content MQWs.

5.2 Experimental

In this work, four wafer trays with gaps of 150, 500, 1000, and 1500 μm were used to control the difference between the wafer surface temperature and gas phase temperature. We define the gap as the distance between the top surface of the pocket and the bottom of the wafer. Five-period InGaN/GaN MQWs emitting wavelengths of 450 (series I), 500 (series II) and 550 nm (series III) were grown on 2-inch GaN/sapphire templates with each wafer tray by MOVPE. As shown in Fig. 5.1, we used 1 × 2-inch horizontal reactor in our MOVPE system, in which the gas flowed in the lateral direction. The height of the flow channel was 6.5 mm. Under the wafer tray, there was a heater to control the wafer surface temperature by heating the wafer tray. An in situ system with a 950 nm pyrometer and photodetector was used to monitor the wafer tray temperature.

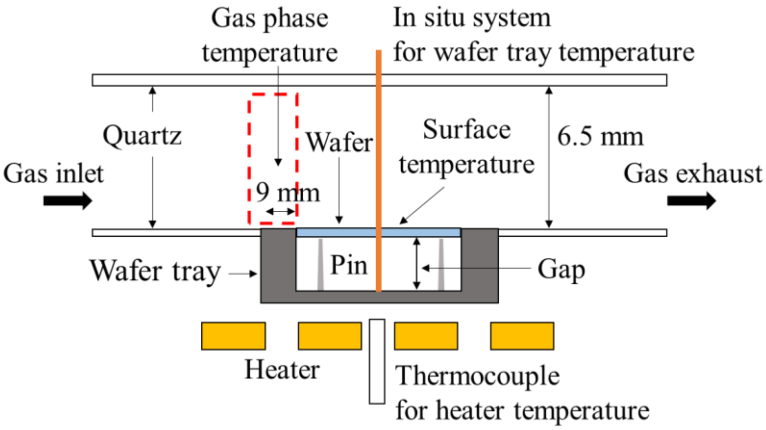

Fig. 5.1 Schematic configuration of the MOVPE reactor.

Triethylgallium (TEGa), trimethylindium (TMIn), NH_3 and N_2 were used as the Ga, In, and N sources and carrier gas. Here, Trimethylgallium (TMGa) was also used to grow InGaN at high growth rate in series III. The well growth conditions are summarized in Table 5.1. The well temperature is expressed as the wafer tray temperature in Fig. 5.2 which was monitored by an in situ system and increases with increasing gap for every series. The barrier growth (5 min) involved three parts: growth at the well temperature as a protection layer (1 min), growth during the temperature ramp (1 min), and growth at the barrier temperature (3 min). According to in-situ monitoring, the temperature was stable after the temperature ramp. The barrier temperature of three series are the same as 740 °C (the well temperature of series I) to keep the same growth condition at the barrier temperature. TEG and NH_3 was supplied during the whole barrier growth. The TEG and NH_3 flow rate was kept at 3.8 μmol/min and 0.33 mol/min, respectively, for all three series. The flow speed was maintained at 1 m/s and pressure was kept at 750 hPa during MQW growth. The X-ray diffraction (XRD) result confirmed the target indium contents of 18, 28, and 33% for series I, II, and III within ±1% and QW and barrier thickness of 2.5 nm and 5 nm. A 405 nm laser was used to measure the photoluminescence (PL) at room temperature and an atomic force microscope (AFM) was used to measure the surface morphology.

Table 5.1 Growth conditions of InGaN well layer

Series	Peak Wavelength (nm)	TEG (μmol/min)	TMI (μmol/min)	NH_3 (mol/min)	Growth time (min)	Growth rate (nm/min)	Pressure (hPa)
I	450	3.8	10.2	0.33	2.50	1	750
II	500	3.8	10.2	0.33	2.50	1	750
III	550	14.7(TMG)	23.6	0.33	0.63	4	750

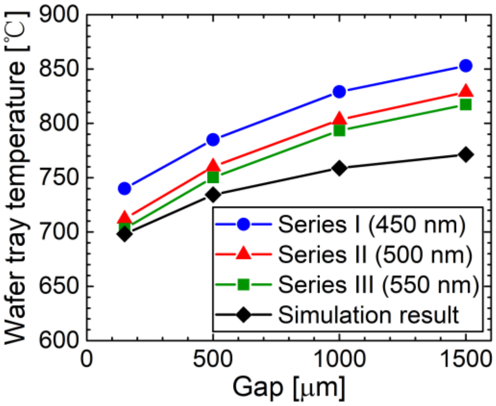

Fig 5.2 Wafer tray temperature of all samples monitored by in situ system.

5.3 Thermal simulation

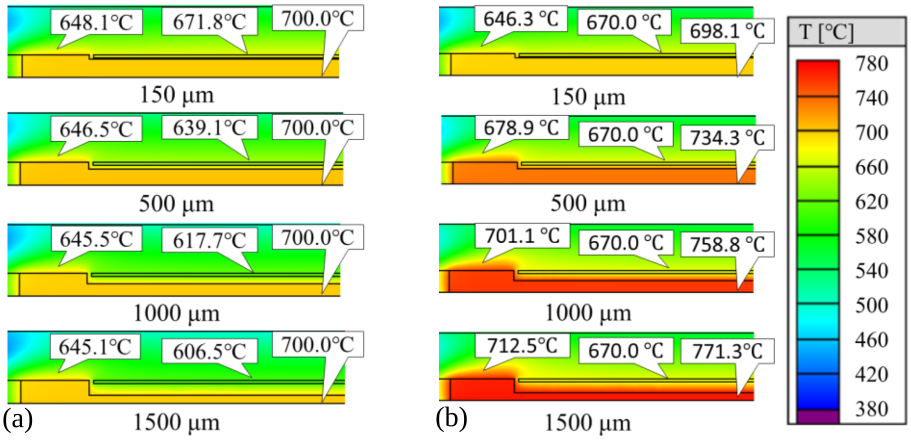

Fig. 5.3 Temperature distribution in the reactor for each wafer tray calculated by Virtual Reactor (STR Group Inc): (a) with the same heat temperature and (b) with the same wafer surface temperature.

Because the real thermal distribution is difficult to be measured by tools, in this work we use Virtual Reactor software (STR Group Inc.) to simulation the thermal distribution of our reactor (Fig 5.1). Figure 5.3 shows the simulation result of thermal distribution in this reactor. In Fig. 5.3(a), if the same heater temperature is set, the wafer surface temperature will decrease from 672 °C to 607°C with increasing the gap of wafer tray. Therefore, in Fig. 5.3(b), if the author wants to maintain a constant wafer surface temperature to grow MQWs with the same wavelength, it is necessary to increase the heater temperature when using a larger-gap. At the same time, the gas phase temperature on the wafer tray before reaching the wafer surface increases from 646 to 713 °C, which is expected to increase the decomposition rate of NH_3. Figure 5.2 shows that the simulated wafer tray temperatures has the same tendency as the measured one needed to keep the indium content constant even if the parameter is not accurately the same with the reality.

In Fig. 5.1, there exists three pins in the pocket to hold the wafer. Their effect on thermal distribution should not be neglected. The size of the pin is 1 mm and the shape of the top is cone-like which means that the touch area between the wafer and the pin is small compared to 2-inch wafer. Figure 5.4 shows simulation results of surface temperature distribution for 1500 µm wafer tray with pin and without pin. The temperature at the pin point is ~6 ℃ higher than the very position on the wafer tray without pin. The temperature difference between these two wafer trays is smaller than 2 ℃ at the distance of 6 mm away from the pin point. Around 16.7% of the wafer area is affected by the pins. However, it is difficult to distinguish the actual effect of the pin on the temperature uniformity from other effects.

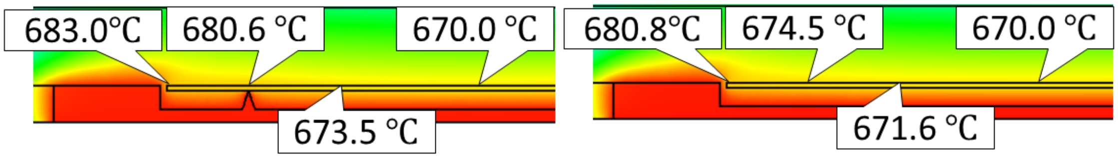

(a) Wafer tray with pin (b) Wafer tray without pin

Fig. 5.4 Wafer surface temperature distribution in the reactor calculated by Virtual Reactor (STR Group Inc) for 1500 µm wafer tray (a) with pin and (b) without pin.

5.4 Results and discussion

Figure 5.5 shows the (a) PL spectra, (b) PL peak intensity and (c) full width at half maximum (FWHM) for all series. For series I, the peak intensity and FWHM of all samples are approximately 1100 counts and 20 nm respectively because of the high growth temperature (i.e. wafer surface temperature) which lead to high NH_3 decomposition rate on the surface. In this case, increasing the gap which improves NH_3 decomposition in the gas phase has no effect on the PL peak intensity and FWHM. For series II and III, the peak intensity decreases and the FWHM increases rapidly because at the lower growth temperatures the effective V/III ratio on the wafer surface is limited by the NH_3 decomposition. However, the increased gas phase temperature by a larger-gap wafer tray increased the peak intensity from 230 to 492 counts at 500 nm and even from 3.3 to 16.3 counts at 550 nm. At the same time, the FWHM decreases from 39 nm to 31 nm and from 85 nm to 72 nm.

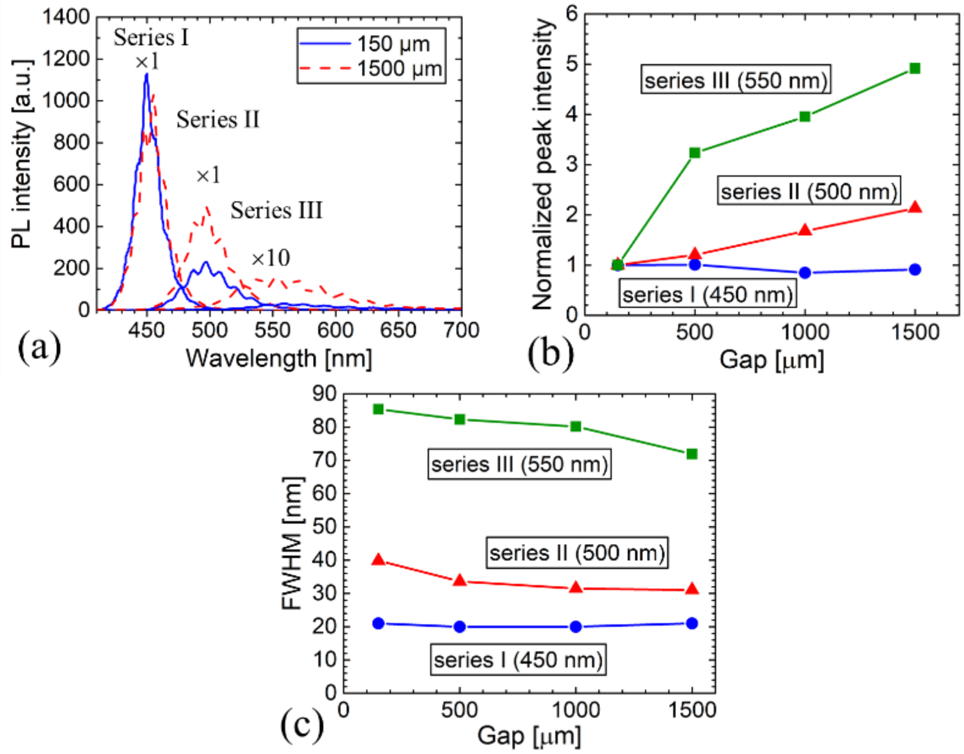

Fig.5.5 (a) PL spectra of MQWs grown using the wafer trays with 150 μm gap and 1500 μm gap for all series, (b) normalized peak intensity, and (c) FWHM of all series.

The improvement of the PL intensity and FWHM at larger gap can be understood from the topography of the samples. Figure 5.6 shows AFM images of MQWs grown using the wafer trays with 150 μm gap and 1500 μm gap for all In concentration series. For series I, both surfaces showed a step morphology. At a high growth temperature and high effective V/III ratio, all the atoms deposited on the surface are incorporated into the step edges [3, 8]. However, for series II and III, the morphology of the MQWs includes many slits or In-rich clusters at narrow gap in Figs. 5.6(b), and (c). Such effects are typical for high-indium-content MQW growth [6]. These rough MQWs show a wider PL FWHM, as there are a multitude of different sites on the surface [9]. Owing to the same barrier growth conditions as those for series I, such morphological deterioration is caused by the low growth temperature and high growth rate of the well layer. These growth conditions decrease the effective V/III ratio on the surface, which increases the roughness of the well layer surface [8]. This rough well layer induces some defects such as slits and clusters during MQW growth [5], which are nonradiative centers. However, with a larger gap as in Figs. 4(e) and (f), the density of clusters was strongly decreased and the trenches became less and shallower. For series II, the depth of slits decreases from 7 to 5 nm, and for series III, the height of clusters decreases from 12 to 7 nm. This is also reflected by the RMS roughness as seen in Fig. 5.6(g).

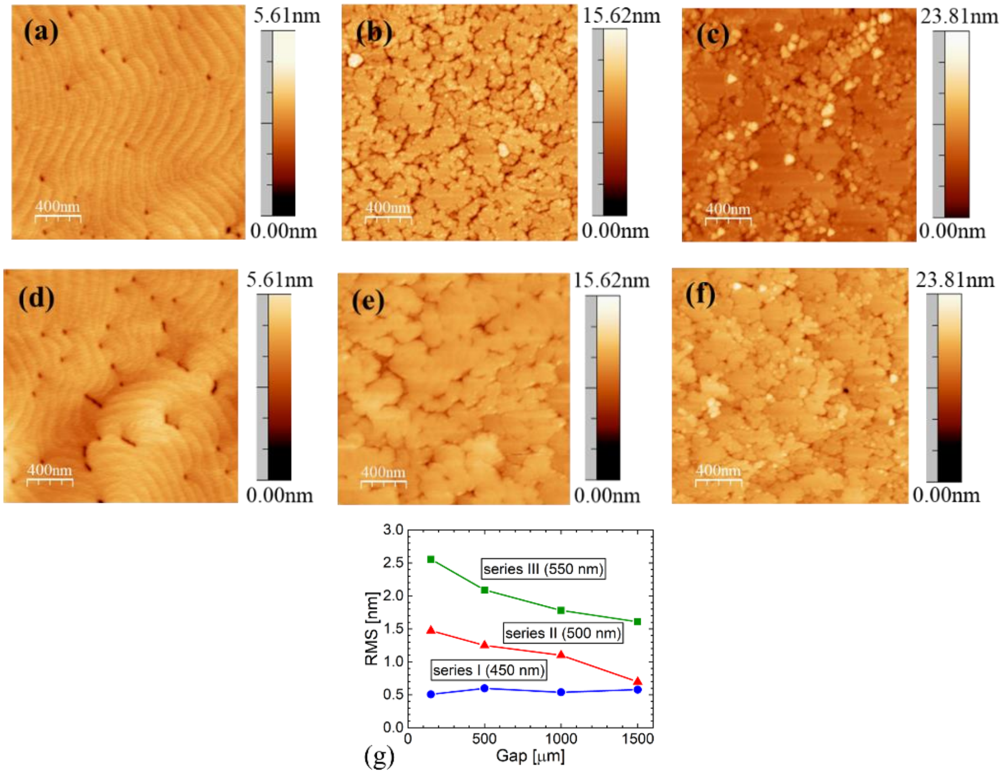

Fig. 5.6 2 μm × 2 μm AFM images of MQWs grown using wafer trays with 150 μm gap and 1500 μm gap: (a), (d) series I 150 μm, 1500 μm; (b), (e) series II 150 μm, 1500 μm; (c), (f) series III 150 μm, 1500 μm and (g) RMS roughness of all series.

The real reaction process between NH_3 and metal organics has not been observed yet. G. Ertl et al. showed that the NH_3 can release H atom to form NH_2 or NH and finally form nitride at a moderate temperature on the surface [10]. Following Figs. 2(a) and (b), the gas phase temperature is increased with increasing gap of the wafer tray to obtain similar wavelength. It is possible that this increased gas phase temperature in front of the wafer increase the possibility of releasing H in the gas phase. And the NH_2 or NH is more active because of the lack of H, and is more easily to be absorbed and bonded on the surface. Therefore, the actual V/III ratio on the wafer surface was increased. For blue QWs, there is evidence in the topography in literature that increasing the nominal V/III ratio enhances the transition to step flow growth [8, 11]. The higher effective V/III ratio in III-group rich region makes it easier for III-group atoms to be incorporated into step edge, which decreases the defect density. Of course, the topography is different for our higher In content MQWs, however, the underlying mechanism is similar. An increased effective V/III ratio would also reduce the In desorption and thus allow for even slightly higher growth temperatures. However, since the temperature was adjusted anyway to achieve similar indium content, this effect was beyond the resolution of this experiment.

Figure 5.7 shows the peak wavelength distribution of series II (500 nm) which is used to express the temperature distribution on the wafer surface. When the position is close to the wafer edge, for 150 and 500 μm, the peak wavelength becomes longer while the peak wavelength becomes short for 1500 μm. The peak wavelength distribution for 1000 μm is more uniform than the others. These peak wavelength distribution (i.e. wafer surface temperature distribution) is possibly because of the combination between the non-uniform well thickness and the effect of the edge temperature of the wafer tray. For 150 and 500 μm, the edge peak wavelength is longer than the center possibly because of the thicker InGaN well layer at the edge. However, for 1000 and 1500 μm, the higher edge temperature of the wafer tray mainly causes to the short wavelength at the wafer edge. Moreover, there exit three pins in the pocket to sustain the wafer (Fig. 5.1). The size of the pin is 1 mm and the shape of the top is cone-like which means that the touch area between the wafer and the pin is small compared to 2-inch wafer. According to the simulation results in previous section, these three pins have some effect on thermal distribution. However, it is difficult to distinguish the actual effect of the pin on the temperature uniformity from other effects. In the future, the peak wavelength distribution on the wafer surface can be improved by design wafer tray with non-uniform gap or controlling heater power at different area.

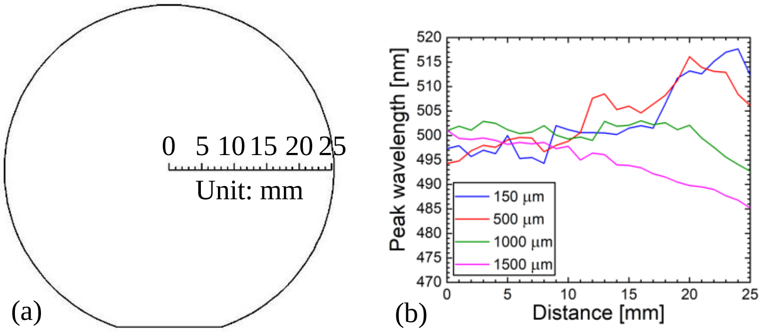

Fig. 5.7 (a) The wafer graph with a line for PL measurement, (b) the peak wavelength distribution of series II along the line in Fig. 5(a).

5.4 Summary

In this study, we used a large-gap wafer tray to improve the optical properties of InGaN/GaN MQWs in a horizontal MOVPE reactor. Numerical fluid dynamic simulation found up to 67 °C higher gas phase temperature at the front of the wafer when using the large-gap wafer tray, which will increase the effective V/III ratio at the surface due to more active nitrogen species. PL intensities and FWHM of long-wavelength MQWs were improved with this increased gas phase temperature at the same PL wavelength. AFM images demonstrated that especially the topography of long-wavelength MQWs was improved by this method. The higher effective V/III ratio makes it easier for III-group atoms to be incorporated into step edge, decreasing the defect density. This method is promising for improving the quality of high-In-content InGaN.

References

1. R. Hashimoto, J. Hwang, S. Saito, and S. Nunoue, “High-efficiency green-yellow light-emitting diodes grown on sapphire (0001) substrates”, Phys. Status Solidi C 10 (2013) 1529-1532
2. Y. Tu, Y. J. Ruan, L. H. Zhu, Q. Z Tu, H. W Wang, J. Chen, Y. J Lu, Y. L Gao, T.-M. Shih, Z. Chen, and Y. Lin, “Influences of point defects on electrical and optical properties of InGaN light-emitting diodes at cryogenic temperature”, J. Appl. Phys. 123 (2018) 161544
3. R. A. Oliver, M. J. Kappers, and C. J. Humphreys, “Growth modes in heteroepitaxy of InGaN on GaN”, J. Appl. Phys. 97 (2005) 013707
4. B Damilano and B Gil, “Yellow–red emission from (Ga, In) N heterostructures”, J. Phys. D: Appl. Phys. 48 (2015) 403001
5. S. Hammersley, M. J. Kappers, F. C.-P. Massabuau, S.-L. Sahonta, P. Dawson, R. A. Oliver, and C. J. Humphreys, “Effects of quantum well growth temperature on the recombination efficiency of InGaN/GaN multiple quantum wells that emit in the green and blue spectral regions”, Appl. Phys. Lett. 107 (2015) 132106
6. S. Kim, K. Lee, H. Lee, K. Park, C.-S. Kim, S.-J. Son, and K-W. Yi, “The influence of ammonia pre-heating to InGaN films grown by TPIS-MOCVD”, J. Cryst. Growth 247 (2003) 55–61
7. V.S. Ban, “Mass Spectrometric Studies of Vapor-Phase Crystal Growth II.”, J. Electrochem. Soc. 119 (1972) 761-765
8. R. A. Oliver, M. J. Kappers, C. J. Humphreys, G. Andrew, and D. Briggs, “The influence of ammonia on the growth mode in InGaN/GaN heteroepitaxy”, J. Cryst. Growth 272 (2004) 393-399

9. F. C-P. Massabuau, P. Chen, M. K. Horton, S. L. Rhode, C. X. Ren, T. J. O'Hanlon, A. Kovács, M. J. Kappers, C. J. Humphreys, R. E. Dunin-Borkowski, and R. A. Oliver, “Carrier localization in the vicinity of dislocations in InGaN”, J. Appl. Phys. 121 (2017) 013104
10. G. Ertl, M. Huber, “Mechanism and kinetics of ammonia decomposition on iron”, J. Catal. 61 (1980) 537-539
11. T. Zywietz, J. Neugebauer, and M. Scheffler, “Adatom diffusion at GaN (0001) and (0001) surfaces”, Appl. Phys. Lett. 73 (1998) 487-489

Chapter 6 Summary and Future Outlook

6.1 Summary

6.2 Future outlook

References

6.1 Summary

In this study, single InGaN layer and InGaN-based MQW growth on GaN substrate and GaN/sapphire template by MOVPE is systematically investigated.

First, single InGaN layers growth illustrates different morphologies: steps, 2D islands, 3D dots, and step bunching. With increasing vapor supersaturation (e.g. low growth temperature, high growth rate), the InGaN morphology changes from steps to 2D islands and then to 3D dots. The large miscut angle of GaN substrate also change morphology from 2D island to step by decreasing surface supersaturation. Too large miscut angles (above 0.9°) will form step bunching. The InGaN morphology is controlled by combination between vapor supersaturation (i.e. growth condition) and miscut angle. The critical miscut angle from 2D island to step becomes large with increasing vapor supersaturation (i.e. higher growth rate or lower growth temperature). Moreover, critical miscut angle is important to obtain higher InN mole fraction and stronger PL intensity with stepped morphology which means high quality. To compare with InGaN on GaN/sapphire template, InGaN on GaN substrate can achieve steps easily because of lower surface supersaturation.

Then, InGaN/GaN MQW growth was studied on both GaN substrate and GaN/sapphire template for different wavelengths. For low InN-mole-fraction, MQWs growth on GaN substrate easily achieve stepped morphology and higher PL intensity. However, for high InN-mole-fraction, MQW surface becomes rough with many defects because the non-uniform strain distribution of InGaN layer with 2D islands easily causes partly relaxation and PL intensity drops much. On the other hand, for short wavelength, large miscut angle has weak PL intensity possibly because it makes barrier grown in the step-bunching region to bring more pits. However, for long wavelength, the growth on the substrate with large miscut angle increases PL intensity because it smoothens InGaN surface by decreasing surface supersaturation. GaN substrate with large miscut angle is expected for improving the optical property of long-wavelength MQW for long wavelength emission besides the low dislocation density.

Finally, the effect of gas phase temperature on MQW growth is studied by wafer tray with different gap in a horizontal MOVPE reactor. Numerical fluid dynamic simulation found up to 67 ℃ higher gas phase temperature at the front of the wafer when using the large-gap wafer tray, which will increase the effective V/III ratio at the surface due to more active nitrogen species. PL intensities and FWHM of long-wavelength MQWs were improved with this increased gas phase temperature at the same PL wavelength. AFM images demonstrated that especially the topography of long-wavelength MQWs was improved by this method. The higher effective V/III ratio makes it easier for III-group atoms to be incorporated into step edge, decreasing the defect density. This method is promising for improving the quality of high-In-content InGaN.

6.2 Future Outlook

6.2.1 InGaN morphology

According to previous research, the morphology of InGaN layer has much effect on InGaN/GaN MQW growth. However, for high InN-mole-fraction, it is difficult to keep InGaN layer with stepped morphology because of high surface supersaturation. Large miscut angle of GaN susbstrate can be used to smoothen InGaN morphology by decreasing surface supersaturation. However, GaN layer growth on large miscut angle should be considered and be improved.

6.2.2 NH_3 decomposition rate

InGaN growth by MOVPE has an inherent disadvantage because it must satisfy the conditions for NH_3 decomposition to form N source and for prevention of InN dissociation, which impose conflicting temperature requirements. Many published papers show that the input V/III ratio during InGaAs growth is just smaller than one hundred, while the input V/III ratio for InGaN growth is necessary to be raised to thousands. But it is still not enough to get good quality of InGaN. The big problem is the very low NH_3 decomposition rate at low growth temperature which should be pay much attention to research for InGaN growth. Some researchers consider to use a high pre-growth temperature or catalyst to improve NH_3 decomposition rate. However, the reactor structure should be re-designed. D. F. Strobel showed that UV light can be one of photolysis to improve NH_3 decomposition in Table 6.1 [1]. Maybe it is a good method and should be considered in the future.

Table 6.1 Chemical reactions in the Jovian atmosphere [1]

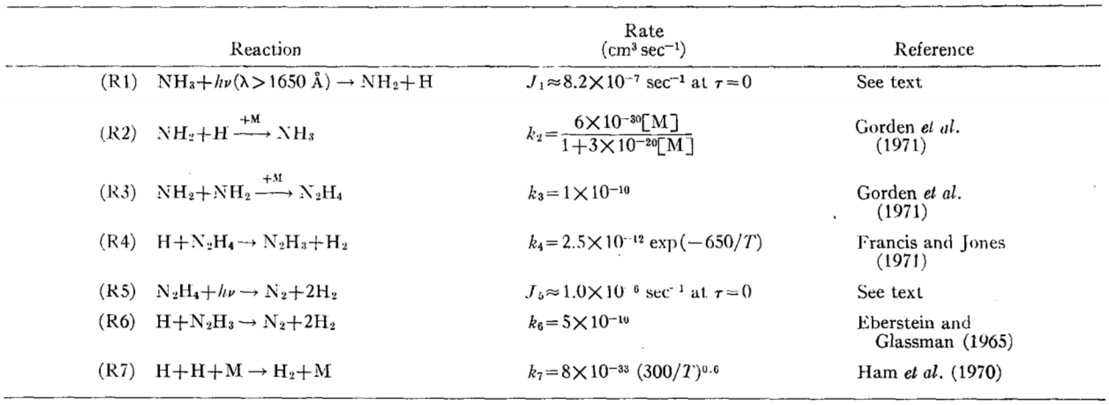

	Reaction	Rate ($cm^3\ sec^{-1}$)	Reference
(R1)	$NH_3+h\nu(\lambda>1650\ \text{Å}) \rightarrow NH_2+H$	$J_1\approx 8.2\times 10^{-7}\ sec^{-1}$ at $\tau=0$	See text
(R2)	$NH_2+H \xrightarrow{+M} NH_3$	$k_2=\dfrac{6\times 10^{-30}[M]}{1+3\times 10^{-20}[M]}$	Gorden *et al.* (1971)
(R3)	$NH_2+NH_2 \xrightarrow{+M} N_2H_4$	$k_3=1\times 10^{-10}$	Gorden *et al.* (1971)
(R4)	$H+N_2H_4 \rightarrow N_2H_3+H_2$	$k_4=2.5\times 10^{-12}\exp(-650/T)$	Francis and Jones (1971)
(R5)	$N_2H_4+h\nu \rightarrow N_2+2H_2$	$J_5\approx 1.0\times 10^{-6}\ sec^{-1}$ at $\tau=0$	See text
(R6)	$H+N_2H_3 \rightarrow N_2+2H_2$	$k_6=5\times 10^{-10}$	Eberstein and Glassman (1965)
(R7)	$H+H+M \rightarrow H_2+M$	$k_7=8\times 10^{-33}\ (300/T)^{0.6}$	Ham *et al.* (1970)

6.3.3 InGaN quantum dot (QD)

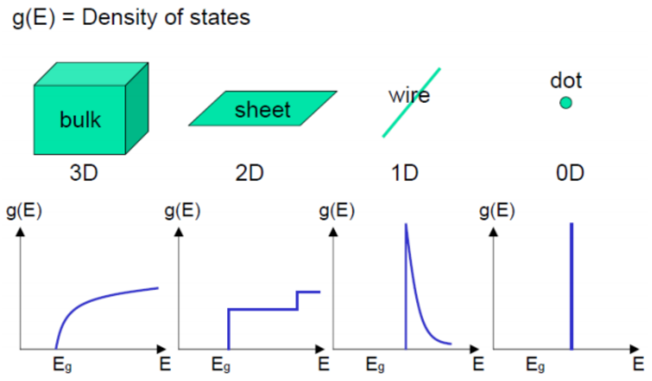

Fig. 6.1 The density of states of different dimensional structures.

Quantum dot (QD) structure has some advantage, such as strain relaxation, little QCSE, three-dimensional (3D) confinement, no extended defect. Moreover, carriers confined inside QDs can not be trapped in nonradiative recombination centers formed by dislocations outside. Therefore, QD should has much high intensity and very narrow FWHM in theory. Nowadays, Ge/Si and In(Ga)As/GaAs QDs are achieved with uniform size distribution by standard Stranski-Krastanow (S-K) growth mode [2, 3]. For high InN-mole-fraction InGaAs laser diode, In(Ga)As/GaAs QDs are expected to achieve a lower threshold current density of laser diodes compared to quantum wells [3]. InGaN/GaN has more strain than InGaAs/GaAs at the same InN mole fraction as shown in Fig. 6.2. Therefore, InGaN/GaN easily form 3D dots with lower InN mole fraction. Some researchers have already reported the InGaN growth by several un-SK methods, such as interruption mode, spontaneous spinodal decomposition, silicon antisurfactant, modified droplet epitaxy [4-7]. However, it is difficult to achieve the uniform size distribution and high PL intensity as InGaAs QD. Our previous research in Chapter 3 shows that the main problem is the rough wetting layer with non-uniform strain distribution before QD growth when we use standard SK mode to grow InGaN QD. While, InGaAs QDs are grown on smooth wetting layer surface as shown in Fig. 6.3 [8]. Therefore, before InGaN growth, smooth InGaN layer with high InN mole fraction should be achieved possibly by using large miscut angle substrate or increasing NH_3 decomposition rate.

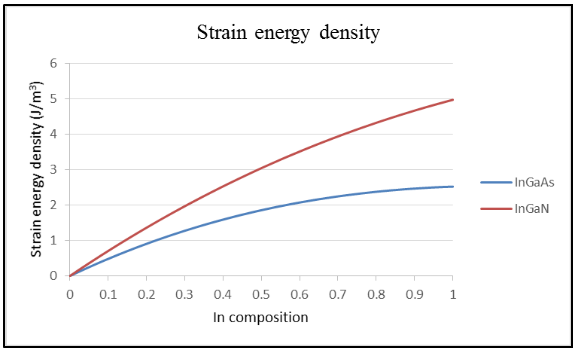

Fig. 6.2 Strain energy density of InGaN/GaN and InGaAs/GaAs

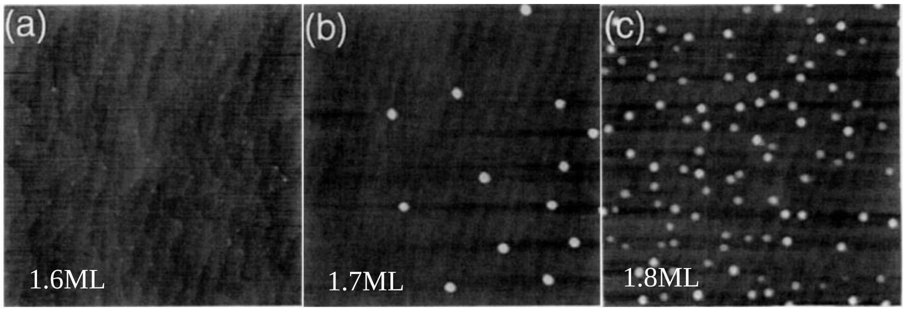

Fig. 6.3 Atomic force micrographs of MBE grown InAs self-assembling quantum dots for InAs coverage of 1.6, 1.7 and 1.8 ML. The micrographs are 1um x 1um in size [8]

References

1. D. F. Strobel, “The Photochemistry of NH_3 in the Jovian Atmosphere”, J. Atmo. Sciences 30 (1973) 1205-1209
2. D. J. Eaglesham and M. Cerullo, “Dislocation-Free Stranski-Krastanow Growth of Ge on Si(100)”, Phys. Rev. Lett. 64 (1990) 1943-1946
3. D. L. Huffaker, G. Park, Z. Zhou, O. B. Shchekin, and D. G. Deppe, “1.3 μm room-temperature GaAs-based quantum-dot laser”, Appl. Phys. Lett. 73 (1998) 2564-2566
4. L.W. Ji, Y.K. Su, S.J. Chang, L.W. Wu, T.H. Fang, J.F. Chen, T.Y. Tsai, Q.K. Xue, and S.C. Chen, “Growth of nanoscale InGaN self-assembled quantum dots”, J. Cryst. Growth 249 (2003) 144–148
5. C. Tessarek, S. Figge, T. Aschenbrenner, S. Bley, A. Rosenauer, M. Seyfried, J. Kalden, K. Sebald, J. Gutowski, and D. Hommel, “Strong phase separation of strained $In_xGa_{1-x}N$ layers due to spinodal and binodal decomposition: Formation of stable quantum dots”, Phys. Rev. B 83 (2011) 115316
6. H. Hirayama, S. Tanaka, P. Ramvall, and Y. Aoyagi, “Intense photoluminescence from self-assembling InGaN quantum dots artificially fabricated on AlGaN surfaces”, Appl. Phys. Lett. 72 (1998) 1736-1738
7. R. A. Oliver, G. Andrew D. Briggs, M. J. Kappers, C. J. Humphreys, S. Yasin, J. H. Rice, J. D Smith, and R. A. Taylor, “InGaN quantum dots grown by metalorganic vapor phase epitaxy employing a postgrowth nitrogen anneal”, Appl. Phys. Lett. 83 (2003) 755-757
8. P.M. Petroff and S.P. DenBaars, “MBE and MOCVD Growth and Properties of Self-Assembling Quantum Dot Arrays in III-V Semiconductor Structures”, Superlattices and Microstructures 15 (1994) 15-21

Publications in PhD Course

Journals

1. **<u>Zhibin Liu</u>**, Shugo Nitta, Shigeyoshi Usami, Yoann Robin, Maki Kushimoto, Manato Deki, Yoshio Honda, Markus Pristovsek, Hiroshi Amano, "Effect of gas phase temperature on InGaN grown by metalorganic vapor phase epitaxy", Journal of Crystal Growth 509 (2019) 50-53.
2. **<u>Zhibin Liu</u>**, Shugo Nitta, Yoann Robin, Maki Kushimoto, Manato Deki, Yoshio Honda, Markus Pristovsek, Hiroshi Amano, "Morphological study of InGaN on GaN substrate by supersaturation", Journal of Crystal Growth 508 (2019) 58-65.

International conferences

1. **<u>Zhibin Liu</u>**, Shugo Nitta, Yoann Robin, Maki Kushimoto, Manato Deki, Yoshio Honda, Markus Pristovsek, Hiroshi Amano, "The effect of miscut angle of GaN substrate on InGaN grown by metalorganic vapor phase epitaxy", International Workshop on Nitride Semiconductors, 11 November - 16 November, Kanazawa, Japan, 2018.
2. **<u>Zhibin Liu</u>**, Shugo Nitta, Shigeyoshi Usami, Yoann Robin, Maki Kushimoto, Manato Deki, Yoshio Honda, Hiroshi Amano, "Effect of gas phase temperature on InGaN grown by metalorganic vapor phase epitaxy", 19th International Conference on Metalorganic Vapor Phase Epitaxy (ICMOVPE-XIX), June 3-8, Nara, Japan, 2018.
3. **<u>Zhibin Liu</u>**, Ryosuke Miyagoshi, Shugo Nitta, Yoshio Honda, Hiroshi Amano, "Morphological study of InGaN layer growth on GaN substrate by metalorganic vapor phase epitaxy", The 12th International Conference on Nitride Semiconductors, July 24-28, Strasbourg, France, 2017.

Domestic conferences

1. **Zhibin Liu**, Ryosuke Miyagoshi, Shugo Nitta, Yoshio Honda, Hiroshi Amano, “Morphology control of InGaN layer on GaN substrate by metalorganic vapor phase epitaxy”, The 64th JSAP Spring Meeting, March 14-17, Yokohama, Japan, 2017.
2. **Zhibin Liu**, Shugo Nitta, Shigeyoshi Usami, Kentaro Nagamatsu, Maki Kushimoto, Manato Deki, Yoshio Honda, Hiroshi Amano, “The effect of the environment temperature of the wafer on InGaN grown by metalorganic vapor phase epitaxy”, The 78th Japan Society of Applied Physics Autumn meeting, September 5-8, Fukuoka, Japan, 2017.

Acknowledgements

I wish to appreciate many people who contributed to my PhD research and helped my life at Nagoya University in Japan. This dissertation would not have been possible without their help and contributions.

First, I would like to express my most sincere gratitude to my supervisor Professor Hiroshi Amano. Before I came into Amano Lab., actually it was my hard time because I wanted and needed to find a way to improve myself. At that time, Prof. H. Amano gave me a chance and allowed me to come into this lab for Ph. D study. His decision changed my life that I can continue to doing research as a job which I like in the future. I am deeply grateful for the opportunity he gave me to study for a doctorate and improve my crystal growth skill in such amazing laboratory. He gave me insightful guidance and indispensable encouragement during my doctoral course. His energetic work, strong interest for research, and gentleness for every person will influence me in my future life. I am extremely fortunate and honored to be his student.

I would like to thank Professor Shugo Nitta who gave me the direct guidance for my research. He teach me not just the knowledge about the research but also how to do research, how to write paper and how to make a good presentation. His hard-work during workdays tell me how to be a good researcher in the future. And his spending much time with family during weekend let me know how to be a good husband and father.

I want to thank Professor Markus Pristovsek who has much experience for InGaN research. During writing paper and taking presentation, he gave me much help and many good suggestions even if I am not his direct student. His research experience let me know which skill should be gotten as a high-level researcher. I also thank Yoann Robin for many helpful suggestions about my research and how to use AFM and PL measurement and thank Professor Zlatko Sitar for giving me good research suggestion during his visiting our lab.

I also want to thank Professor Yuhuai Liu. He help me a lot and gave some great suggestion about living in Japan. He is a good bridge between Chinese and Japanese and between student and teacher, especially for me because I can not speak Japanese. I want to thank Professor Yoshio Honda, Professor Atsushi Tanaka, Assistant Professor Maki Kushimoto, Assistant Professor Manato Deki for their advice and kind assistance in using apparatuses related to my research.

I am grateful to all secretary in our lab (Hosoe san, Tatsumi san, Fujie san, Tsukada san, Ito san). I can not finish my study in Nagoya University without their kind help. I also thank all members in Amano lab. They let me have an amazing life in Nagoya, Japan for these three years. Before that, I haven’t live so long time outside my hometown. In a sense, Nagoya is my second hometown.

At last, I would like to thank my family for their unconditional love and support, especially my wife Qizhao Huang. During my study in Japan, I had done a most important and meaningful thing that I married with Qizhao Huang. I am very grateful for her never leave even if I studied abroad and can not live with her.